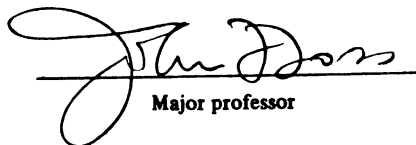THESIS

This is to certify that the

thesis entitled

Experimental Investigation of an Aerodynamic
Shroud for Cooling Fan Applications

presented by

Scott C. Morris

has been accepted towards fulfillment
of the requirements for

____MS____ degree in _Mechanical_ Engineering

_____
Major professor

Date_8 May 97_

O-7639

LIBRARY
Michigan State
University

PLACE IN RETURN BOX to remove this checkout from your record.
TO AVOID FINES return on or before date due.

DATE DUE	DATE DUE	DATE DUE
————————	————————	————————
————————	————————	————————
————————	————————	————————
————————	————————	————————
————————	————————	————————
————————	————————	————————
————————	————————	————————

c:\circ\datedue.pm3-p.1

EXPERIMENTAL INVESTIGATION OF AN AERODYNAMIC

SHROUD FOR COOLING FAN APPLICATIONS

By

Scott C. Morris

A THESIS

Submitted to

Michigan State University

in partial fulfillment of the requirements

for the degree of

MASTER OF SCIENCE

Department of Mechanical Engineering

1997

ABSTRACT

An experimental study was performed on an automotive cooling fan with a unique aerodynamic shroud. The development of the aeroshroud device was motivated by the relatively high (2.5cm) tip clearance required in engine driven fan applications. The shroud consists of a pressurized plenum and a Coanda attachment surface to deliver an annular jet of high momentum air into the tip clearance region. The present experimental data were acquired in the recently developed Automotive Cooling Fan Research and Development (ACFRD) facility. The ACFRD facility provides the capability to measure the integral flow characteristics: pressure rise, volume flow rate, and fan input power, as well as detailed velocity measurements in the wake of the fan.

The functional dependence of the relevant dimensionless parameters was derived using a boundary value problem approach. Analysis of the performance data presented indicate that two of the independent variables can be combined into a single parameter which represents the relative power input into the aerodynamic shroud. The data show that the shroud decreased performance and efficiency for the lower flow rates, and increased values at higher flow rates.

Time mean flow directions were measured with a wool tuft. These data indicate that reversed flow exists in the tip clearance area at higher flow rates. However, when the aerodynamic shroud was activated, positive axial momentum was maintained in the tip clearance area. Velocity measurements were taken using an X-array hot-wire probe whose angular orientation was aligned with the mean flow vector measured by the tuft. Time averaged and phase averaged velocities were computed from the recorded time series. These data are presented at several operating conditions in order to characterize the flow field in the wake of the fan.

Acknowledgments

I would like to thank my advisor Dr. John Foss, who has provided me with the oportunities and challenges that have allowed me to grow. Additionally, I would like to thank Dr. Foss for the personal attention that is not just uncommon, but unfound in today's academia.

Secondly I would like to thank Tom Veling of the Ford Motor Company. It is Tom's technical guidance and insight that has allowed this project to be successful. Thanks also go to John Pakkala for all the extra work that went in to the design of the ACFRD facility.

I would like to thank my friends Doug Neal and Klaus Willenborg for the great coffee breaks to procrastinate with. Also I would like to thank Eric Partyjak for the conversations that fueled my passion not only for fluid mechanics, but for science in general. I would also like to thank Yvonne Chang for being there to keep me healthy and positive through the past few years.

Finally, I need to thank my parents, who have given me the perfect blend of guidance, and freedom to achieve my dreams.

TABLE OF CONTENTS

LIST OF FIGURES

NOMENCALTURE

English

A,B,n	Calibration coefficient of Collis and Williams relationship; see (4-11)
A_{cl}	Area bounded by the shroud and fan tip; see (6-1)
A_{flow}	Area bounded by the fan hub and the shroud.
A_{nozzle}	Exit area of calibration nozzles; see (4-2).
C_d	Discharge coefficient of calibration nozzles; see (4-2).
D_{hub}	Diameter of the fan hub; see Figure 1.1.
$D=D_{fan}$	Diameter of fan; see Figure 1.1.
E	Voltage measured from hot-wire anemometer.
$\vec{F}_P$	Force measured for flow rate measurement.
g	Gap thickness of Coanda jet; see Figure 1.1.
i	Voltage measured in power measurement; see section 4.1.4.
k'	Calibration constant for flow rate measurement; see (4-1)
P_{fan}	Pressure rise across the fan ($P_{receiver}$-P_{atm})
P_{shr}	Shroud plenum pressure.
$Ᵽ_{fan}$	Shaft power input to the fan.
$Ᵽ_{shr}$	Power input to the shroud; see (2-6)
$Ᵽ_{system}$	Drive motor power including drive system losses; see (4-6).
$Ᵽ_{losses}$	Drive system losses measured without cooling fan; see (4-6).
Q	Magnitude of the velocity vector measured by the hot-wire probe; see Section 4.5.2
Q_{fan}	Approach flow rate through the fan.

Q_{shr} Flow rate through the shroud.

r Radial coordinate measured from the fan axis. See Figure 3.8.

r_{jet} Radius of curvature of the Coanda jet; see Figure 3.1

R Radius of fan ($R=D/2$); used in presentation of velocity data

U_o Mean flow velocity through the fan (Q_{fan}/A_{flow}).

U_{tip} Linear velocity of the fan tip ($U_{tip}=\pi D\Omega$).

u,v,w Velocity components in probe coordinates.

U_x,U_r,U_θ Velocity components in laboratory coordinates.

v Voltage measured in power measurement; See Section 4.1.4

x Axial coordinate measured from the trailing edge of the blades. See Figure 3.8

Greek

α Angular coordinate fixed to the rotating fan. See Figure 3.8.

$\beta_{+,-}$ Angle of the hot wire with respect to the probe axis.

β_{jet} Angle of the exit flow of the Coanda jet. See Figure 3.1

χ Dimensionless power input to the shroud. See (2-9).

ΔP_{fan} Upper receiver gage pressure.

ΔP_{shr} Shroud Plenum gage pressure.

ϕ Dimensionless flow rate through the fan. See (2-1)

γ Angle of the velocity vector with respect to the probe axis.

η_{sys} Efficiency of fan and shroud system. See (2-5)

η_{shr} Efficiency of the shroud delivery system.

Λ	Dimensionless flow rate through the shroud. See (2-4)
ρ	Density of the working fluid (air)
ψ	Dimensionless pressure rise across the fan. See (2-2)
θ	Angular coordinate of the laboratory reference frame. See Figure 3.8.
Ω	Rotational speed of the cooling fan.
η	Ratio of hot-wire voltage to the voltage of the same wire at $\gamma=0$. See (4-14).
ξ,ζ	Angular position of probe support apparatus. See Figure 4.3

Subscripts

n	Flow rate metering device on north side of facility.
s	Flow rate metering device on south side of facility.
+	Reference to the hot wire with $\beta>0$
-	Reference to the hot wire with $\beta<0$

Symbols

For a quantity a:

$<a>$	Phase averaged quantity
$\bar{a}$	Mean value (time or phase averaged).
$\tilde{a}$	RMS value (time or phase averaged).

1. INTRODUCTION

1.1 Aerodynamic Shroud Concept

Engine mounted automotive cooling fans (primarily truck applications) require a large tip clearance between the fan tip and the shroud. A 2.5cm tip clearance is typical for a 45cm fan. As a consequence, their typical operating efficiencies are less than 20%. An innovative concept[1] has been developed to modify the current shroud in order to enhance the overall efficiency of the fan-shroud system. This 'aerodynamic shroud' utilizes an annular pressurized plenum to deliver a Coanda attachment jet that serves to "fill" the gap between the blade tip and the physical surface of the shroud; see Figure 1.1 Note that the jet velocity profile shown in Figure 1.1 is a schematic representation of what would exist if the fan were not spinning. The use of the convex wall jet as opposed to a straight air delivery was to prevent the jet apparatus from obstructing the area upstream of the fan. Also, the entrainment properties of a convex wall jet could aid in efficiency. The goal of the device is to realize a power savings that is greater than the power required to pressurize the shroud's plenum.

The variables used to describe typical fan investigations are the fan diameter (D), rotating speed characterized by U_{tip}, fluid viscosity (υ), pressure rise (ΔP_{fan}), and flow rate (Q_{fan}). The aerodynamic shroud introduces the following variables: shroud jet-gap (g), shroud flow rate (Q_{shr}), and shroud plenum pressure:

---

[1] The original concept was conceived by Professor John Foss, Department of Mechanical Engineering, Michigan State University, September 1994. Patents of this and a related concept are pending.

1

$$\Delta P_{shr} = P_{shroud-plenum} - P_{T-approach} \qquad\qquad (1\text{-}1)$$

The use of $P_{T-approach}$ permits the presence of the upstream loss elements (e.g. heat exchangers) to be represented in the measurements. In their absence, this value is that of the undisturbed atmosphere (i.e., the present case). The flow field shown in Figure 1.1 can be considered to be a boundary value problem whose solution (the pressure and velocity field) is of interest. The only parameter in the governing (Navier-Stokes) equations is the Reynolds number. Chapter 2 uses this approach to identify the functional dependence of the dimensionless variables of interest.

Prior to the prototype construction of the aerodynamic shroud, a planar model was built to observe the Coanda attachment phenomena for a range of possible geometries. A constant speed centrifugal blower and throttle were used to provide pressurized air to the plenum. Visualization results aided in the selection of the geometry to be used for the prototype. An axisymmetric prototype was then constructed for testing with an automotive cooling fan. A 1994 Ford Explorer fan was selected for the experiments. Details of the planar model results, prototype design, air delivery system, and test fan are given in Chapter 3.

The Automotive Cooling Fan Research and Development (ACFRD) Facility has recently been constructed at the Turbulent Shear Flows Laboratory (TSFL) at Michigan State University. This facility was constructed for investigations of the integral performance characteristics (pressure rise, volume air flow, and input power) as well as discrete velocity measurements in the wake of automotive cooling fans and auxiliary components. The aerodynamic shroud was mounted in the test section of the facility for the experiments. Details of the ACFRD facility and its measurement capabilities are

given in Chapter 4. Procedures for the tuft and hot-wire measurements will also be discussed in Chapter 4. Hot-wire calibration and data collection procedures are explained in detail. An iterative algorithm was used to convert the recorded voltages from the x-array probe to velocity time series. Equations are then presented to calculate the time averaged and phase averaged velocity fields.

A series of experiments were conducted to measure the performance and efficiency of the fan and aerodynamic shroud combination. The flow rate through the shroud was measured independently from the total system flow rate such that the approach flow rate could be used in performance calculations. A range of jet gap heights (g), shroud pressure conditions, and fan rotation speeds were tested. The dimensionless groups of interest and their functional dependencies (derived in Chapter 2) were used to present the data. An additional "collapse" of the data in addition to that expected from the boundary value problem analysis was found to be possible. The results showed an increase in performance and efficiency values for higher flow rates, and degraded values for the lower flow rates. Details of the experiment and results of these "integral" characteristics are given in Chapter 5. Additionally, a brief study was conducted to measure the performance of the fan with a small tip clearance. The results shown in Section 5.4 demonstrate that the aerodynamic shroud with a 2.5cm tip clearance can increase performance and efficiency when compared to a shroud with a near zero tip clearance.

Several conditions of interest were identified for further study based on the results of the integral data. Specifically, tuft visualizations and velocity data were acquired in the fan wake to characterize the flow field for these conditions. The tuft observations were useful in identifying the time mean velocity vector directions in the wake of the fan.

These data were used to characterize the general attributes of the flow field and for setting the angular orientation of the hot-wire probes. Probes using hot-wires in an x-array were used to acquire time series data from which time averaged as well as phase averaged velocity components were computed; see Chapter 6. Phase averaged vorticity values are also reported.

The mass air flow of an automotive cooling system depends on the fan performance, and the resistance to airflow caused by the heat exchangers, grill, and engine components. The data acquired in the ACFRD facility indicate that the operating condition will greatly affect how the aerodynamic shroud affects the system performance. A brief study to estimate the system resistance of a Ford Explorer was performed. Discussion of this as well as predictions of the in-vehicle performance are given in Chapter 7.

1.2 Previous Work: Aerodynamic Shroud

The fluid mechanical attributes of curved wall jets have been studied extensively; see for example: Wilson and Goldstein (1976), Shakouchi et. al (1989), and El-Taher (1983). The added entrainment of the convex wall jet has motivated the use of annular Coanda ejectors for many applications (Ameri and Dybbs (1993)). To the author's knowledge, this is the first work based on the use of an annular jet as a physical boundary condition for any type of rotating machinery.

The experiments described herein were designed specifically for the automotive cooling fan application. A 1994 Ford Explorer cooling fan was selected as the test fan for the experiments. The design of efficient automotive cooling fans is typically based on a 'trial and error' approach. Specifically, different blade designs are tested for a given vehicle prototype until a fan is selected as having suitable performance characteristics. In

general, the shroud design is selected based on packaging constraints (i.e. available space) in the underhood compartment. It is not a typical approach to explore the use of innovative shroud designs to enhance system performance. It is worth noting that the aerodynamic shroud concept could be applied to other applications. The data to be presented in Chapter 5 indicate that applications in which a small tip clearance is allowed could benefit from a larger tip clearance with the aerodynamic shroud.

1.3 Previous Work: Velocity Measurements

The majority of the past research involving automotive cooling fans has been restricted to the measurement of the integral quantities such as pressure rise, volume air flow, and input power. Detailed measurements in the wake of cooling fans have been acquired by Van Houten et. al (1993) using a one component LDV system. A number of investigators have used hot-wire techniques to measure the flow field downstream of other turbomachinery such as compressors, turbines, and axial fans; see e.g. Kuroumaru et. al (1982), Hirsch et. al (1977), and Lakshminarayana (1981). The flows of interest are difficult to measure because of the inherent unsteadiness and the relatively high turbulence levels common to these devices. Most of the available literature describes geometries in which an axial flow machine is placed into a cylindrical wind tunnel for the measurement program. It is typical in automotive cooling fan research Baranski (1974) to provide the fan with quiescent inlet conditions, and a large receiver as the outlet. These "open" boundary conditions allow the fan to create large radial velocity components that would be bounded with the cylindrical passage of a wind tunnel. In order to acquire velocity data in these types of flows, the hot-wire probe must be oriented such that the probe's axis is aligned with the mean velocity vector. To the best of the

author's knowledge the measurement techniques developed for this thesis have not previously been used in the study of automotive cooling fans.
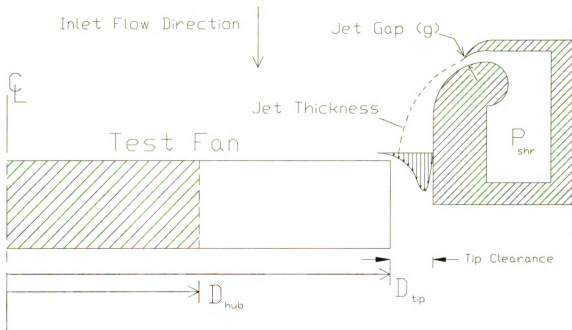
Figure 1.1: Schematic of fan and aerodynamic shroud

2. ANALYSIS

It is useful to consider the cooling fan and the aerodynamic shroud to be the internal elements of a boundary value problem whose upstream boundary is the laboratory "atmosphere" and whose downstream boundary is the receiver (see Chapter 4.1 for details of the experimental facility). The governing parameters for the flow field can then be reliably extracted as those quantities that would influence the solution: $\vec{V}(x,r,\theta,t)$ and $P(x,r,\theta,t)$. Proper scaling quantities are required to characterize this flow field; these are selected to be:

i) the tip speed of the fan blade (U_{tip}) as the reference velocity in the problem,

ii) the fan diameter (D) as the length scale of the problem, and

iii) the kinematic viscosity (υ) of the working fluid (air).

The boundary value problem can therefore be specified in terms of its boundary condition parameters and its Reynolds number ($U_{tip}D/\upsilon$). It is typical in fan studies (Baranski (1974)) to not include the Reynolds number as a significant parameter. The results shown in Chapter 5 confirm the insensitivity of the present data to the magnitude of the Reynolds number; hence it will not be considered in the set of governing parameters given below.

The boundary value problem described above in general terms for the flow field of Figure 1.1 will be made specific by identifying the boundary conditions, i.e. the independent parameters. The approach flow rate (Q_{fan}) can by expressed as:

$$\phi = \frac{U_o}{U_{tip}} \qquad\qquad (2\text{-}1)$$

where $U_o = \frac{Q_{fan}}{A_{flow}}$, and $A_{flow} = \frac{\pi}{4}(D_{shr}^2 - D_{hub}^2)$ represents the annular area between the shroud and fan hub. The pressure of the shroud plenum (ΔP_{shr}), referenced to the tip speed as $\frac{\Delta P_{shr}}{\rho U_{tip}^2}$, characterizes the "driving potential" for the shroud flow. The height (g) of the Coanda jet opening characterizes the shroud (given its basic aerodynamic shape as shown in Figure 1.1). Its parametric designation is (g/D).

The dependent integral parameters of interest are: fan pressure rise, shroud volume flow rate, and system efficiency. In dimensionless form, the typical expression for the pressure rise across a conventional fan (ΔP_{fan}):

$$\psi \equiv \frac{\Delta P_{fan}}{\frac{1}{2}\rho U_{tip}^2} = \psi(\phi) \qquad (2\text{-}2)$$

is modified to:

$$\psi = \psi\left(\phi, \frac{\Delta P_{shr}}{\rho U_{tip}^2}, \frac{g}{D}\right) \qquad (2\text{-}3)$$

The shroud flow rate (Q_{shr}) and system efficiency (η_{sys}) can be respectively described as

$$\Lambda \equiv \frac{Q_{shr}}{U_{tip} A_{flow}} = \Lambda\left(\phi, \frac{\Delta P_{shr}}{\rho U_{tip}^2}, \frac{g}{D}\right) \qquad (2\text{-}4)$$

and

$$\eta_{sys} \equiv \frac{\Delta P_{fan} Q_{fan}}{P_{fan} + P_{shr}} = \eta_{sys}\left(\phi, \frac{\Delta P_{shr}}{\rho U_{tip}^2}, \frac{g}{D}\right). \qquad (2\text{-}5)$$

where the power required to drive the fan is P_{fan} and that to pressurize the shroud is defined as

$$P_{shr} \equiv \frac{\Delta P_{shr} Q_{shr}}{\eta_{shr}} \qquad (2\text{-}6)$$

and η_{shr} is the efficiency of the shroud delivery system. The effect of η_{shr} on the overall system efficiency depends on the relative size of P_{shr} with respect to P_{fan}. Chapter 5 will use two values $\eta_{shr}=1.0$ and 0.7 in the presentation of efficiency data.

Using equation (2-4), equations (2-3) and (2-5) can be rewritten in terms of their functional dependence as

$$\psi = \psi\left(\phi, \Lambda, \frac{\Delta P_{shr}}{\rho U_{tip}^2}\right) \tag{2-7}$$

and

$$\eta_{sys} = \eta_{sys}\left(\phi, \Lambda, \frac{\Delta P_{shr}}{\rho U_{tip}^2}\right) \tag{2-8}$$

respectively. Examination of the experimental data that will be presented Chapter 5 has revealed a useful simplification of equations (2-7) and (2-8). Specifically, the variables $\frac{\Delta P_{shr}}{\rho U_{tip}^2}$ and $\frac{Q_{shr}}{A_{fan} U_{tip}}$ can be combined to a single dimensionless variable using their product:

$$\chi \equiv \Lambda \cdot \left(\frac{\Delta P_{shr}}{\rho U_{tip}^2}\right) = \frac{\Delta P_{shr} Q_{shr}}{\rho A_{flow} U_{tip}^3} \tag{2-9}$$

3. AERODYNAMIC SHROUD AND TEST FAN

This chapter describes the geometric details of the prototype aerodynamic shroud and how the design parameters were selected. The first section (3.1) describes an initial study using a planar Coanda jet to observe the qualitative attributes of the flow field. The following section (3.2) describes the axisymmetric prototype and air delivery system respectively. Section 3.3 shows the details of the test fan used in the experiments.

3.1 Planar Coanda Model

A planar Coanda jet was built for initial study due to the anticipated expense of the aerodynamic shroud prototype (which employs an annular jet). The purpose of the planar model was to test the ability of the jet to remain attached to the convex surface for a range of jet Reynolds numbers $(Re_{jet}=(U_jw/v)$ where U_j is the reference velocity derived from the plenum pressure of the shroud.) Given the relatively large ratio of the shroud radius to local jet thickness $(R_{shr}/\delta\approx12)$, it was decided that the planar model should yield satisfactory qualitative results when compared to the prototype. A drawing of the geometry is shown in Figure 3.1 . A Cincinnati centrifugal blower and throttle plate were used to pressurize the plenum. The jet width (w) was varied by repositioning the upper surface of the plenum chamber. Plexiglas was used for the side wall in the area of the jet for flow visualization.

The basic aerodynamic shape consists of a 180 degree convex wall, followed by a 5cm straight section; see Figure 3.1 . The intent of the straight section was to provide a constant tip clearance for an axial distance equal to the chord of the blade. The end of the straight section is characterized by a sharp 90 degree edge. Two radii of curvature (r_{jet} =

11

4.60 and 3.81 cm) were tested for the convex wall section. Experimental data reported Shakouchi et. al (1989) have shown 2D Coanda jets with similar radii of curvature will remain attached for the range of Reynolds numbers ($400<Re_{jet}<10,000$) of interest. The upper surface of the jet consisted of a curved "lip" with a sharp edge to define the jet exit. Two values of $\beta = 0$ and 30 degrees were used to observe the effect of the location of the jet exit.

A tuft was used to observe the flow field. The tuft consisted of a short (≈ 15mm) segment of white yarn held in the flow using an aluminum shaft, sewing needle, and light thread (details of the tuft probe are given in Section 4.4) Tests were conducted for a wide range of plenum pressures ($20<(P_{plenum}-P_{receiver}<1000$ Pa) and jet widths ($1.0 < w < 4.0$ mm.) The visualization results indicated that the jet remained attached for the radii values and the Reynolds numbers tested. The flow field presented did not visually appear to be sensitive to Re_{jet}, and the flow remained attached to the convex wall for all the conditions tested. Figure 3.2 shows a schematic of the vector directions observed for $r_{jet}=4.6$cm, $Re_{jet} = 2500$, and $\beta=30°$.

The dimensions of the Coanda surface shown in Figure 3.1 were selected for the axisymmetric prototype based on the above visualizations and machining constraints. Specifically, the planar observations indicate that the selected cross sectional geometry should provide the cooling fan an attached, non-reversing flow in the tip clearance area.

3.2 Prototype Design and Pressurization System

A detailed drawing of the prototype shroud and plenum is shown in Figure 3.3. The inner diameter of the shroud was 508mm (20"); cross sectional dimensions are shown in Figure 3.1. The shroud was machined as two pieces which allowed the setting of the jet

gap. Both pieces were machined from RenShape #440. The upper surface of the plenum was constructed from by a ½" stock plywood plate which was mounted to three segments of ½" threaded rod. The upper shroud piece was fastened to the under side of this plate. The jet gap was then varied by adjusting the three support rods to position the upper piece of the shroud; a drill bit was used to measure the gap size (g). The side walls of the plenum were also constructed from ½" plywood. A ¾" plywood cover plate was mounted to the test section of the ACFRD, which acted as the lower surface of the plenum, and rigidly supported the lower piece of the shroud.

A schematic of the pressurization system used to supply air to the shroud is shown in Figure 3.4. The Cincinnati blower (noted above) was used to move the air from the laboratory, through the system of PVC pipes, and into the shroud plenum. The piping system terminates at the four inlets to the shroud plenum in order to provide a symmetric delivery of low momentum air into the plenum. A throttle plate upstream of the blower and an auxiliary outlet allowed the flow rate into the shroud to be controlled. The purpose of the auxiliary output was to maintain a relatively high volume air flow through the blower to prevent viscous heating of the air before entering the shroud plenum.

The volume flow rate into the shroud was measured by an "elbow meter". As shown in Figure 3.4, pressure measurements on the inner and outer surfaces of a bend in the PVC delivery system allowed the flow rate to be inferred. A calibration of the device was conducted using the FordHaus facility of the TSFL, see Figure 3-5. In this process a calibrated venturi nozzle was used to measure the flow rate through the system. Two Validyne pressure transducers and a PC based A/D system (see Chapter 4) were used to

measure the pressure differences of both the elbow meter and the venturi nozzle. Figure 3.6 shows the calibration data and parabolic curve fit. The resulting transfer function:

$$Q_{shr} = 2(5.348)\Delta P_{shr}^{0.5} \qquad (3\text{-}1)$$

was used to infer the volume air flow rate through the shroud. Note the factor of 2 used in equation (3-1) because the elbow meter is located downstream of a "split" in the delivery system as shown in Figure 3.4. The equality of the flow in the two branches was checked by measuring ΔP_{shr} as a function of the flow rate Q_{shr} with the cooling fan removed. This test was repeated with the elbow meter moved to the other "branch" of the delivery system. These data are shown in Figure 3.7. These data indicate that the flow rates through both the 'east' and 'west' branches of the flow system are equal to within the precision of the measurement.

A brief study was performed to characterize the velocity profile of the annular jet with the cooling fan removed. The results are useful in characterizing the shroud, but do not necessarily represent the boundary conditions of the cooling fan. These data are given in Appendix A.

3.3 Test Fan

The selected cooling fan used in the experiments was that of a 1994 Ford Explorer. A representation of the 457 mm diameter test fan is shown in Figure 3.8. The 10 blades have an 81 mm chord with a 41° pitch (i.e. angle of the chord with respect to the plane of rotation.) The hub to tip ratio was 0.472. The blade thickness was approximately 2mm over the span. The solidity (chord divided by blade spacing, see Lakshminarayana, 1996) at blade tip was 0.349.
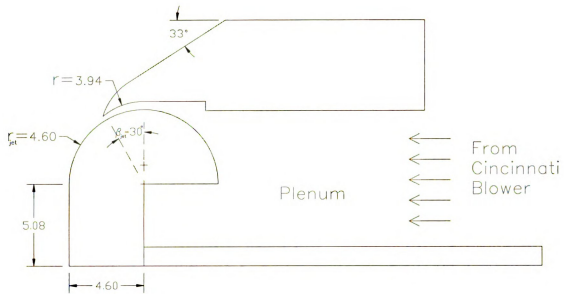
Figure 3.1 Detailed drawing of the planar test geometry
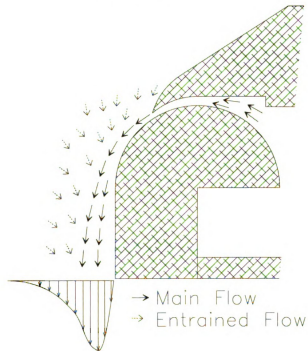
Figure 3.2 Schematic representation of the flow directions observed
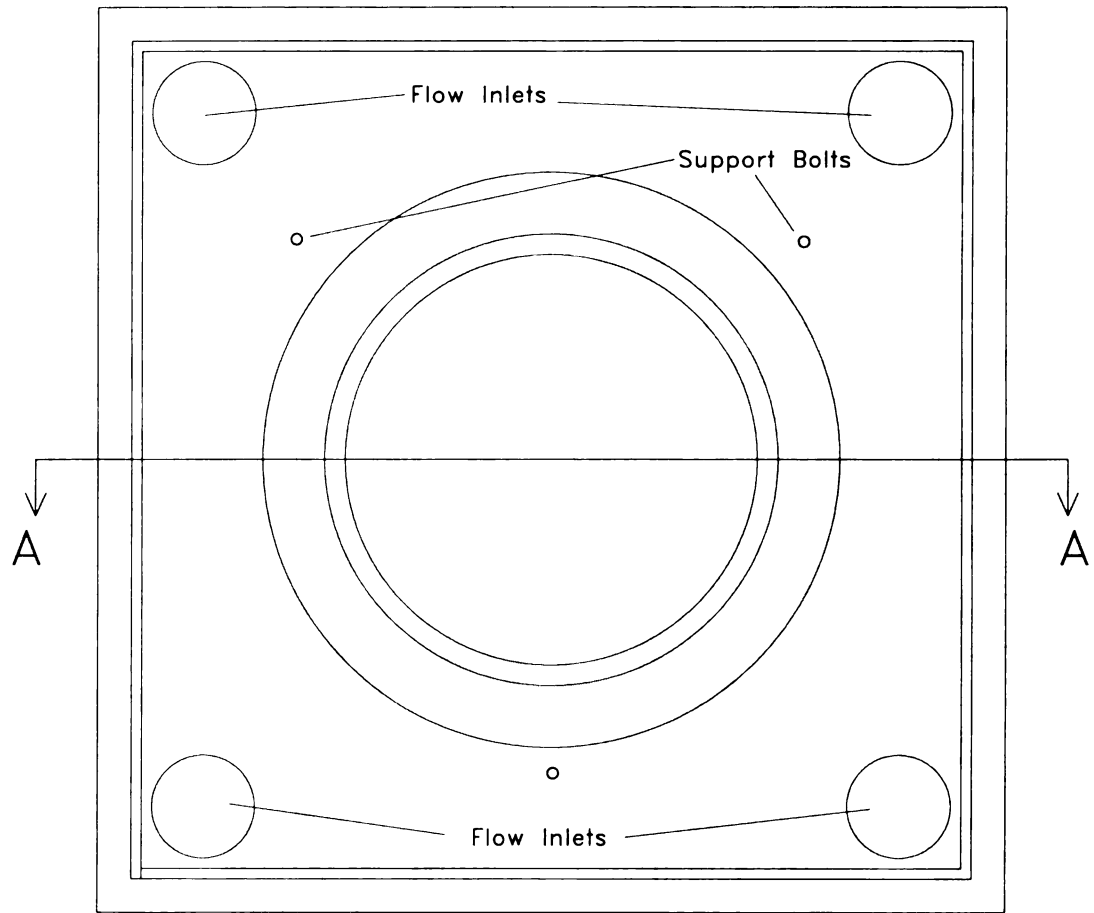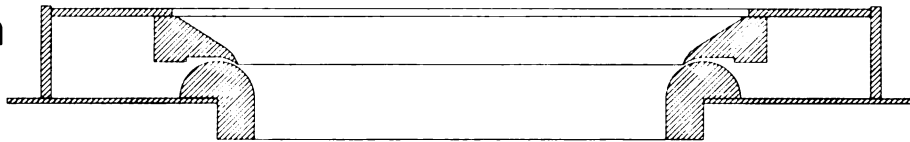
Figure 3.3 Detail of shroud and plenum

Elbow Meter
Pressure Taps

Auxiliary Exit

Inlet
Throttle

Cincinnati Blower
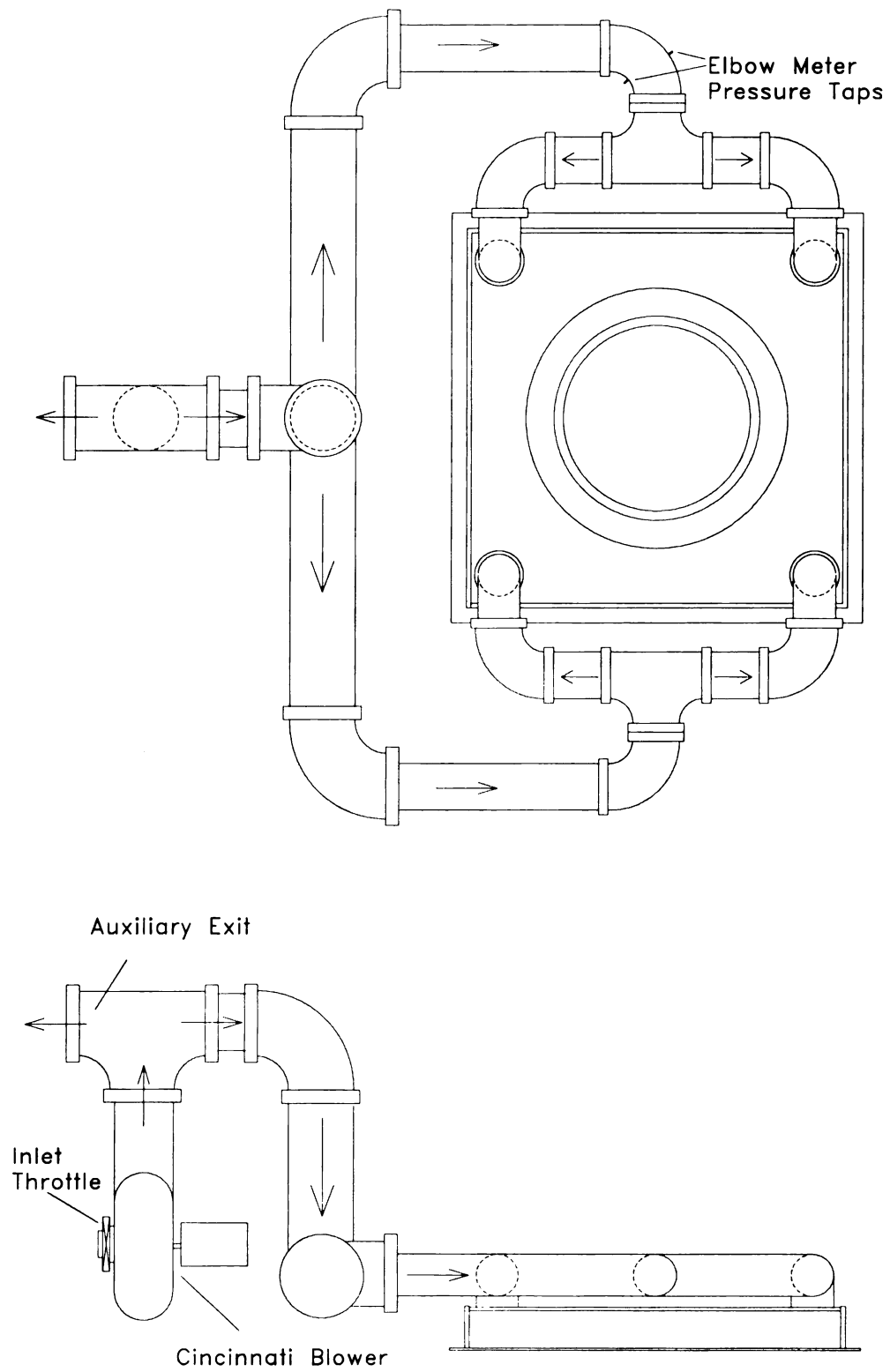
Figure 3.4 Schematic of shroud pressurization system
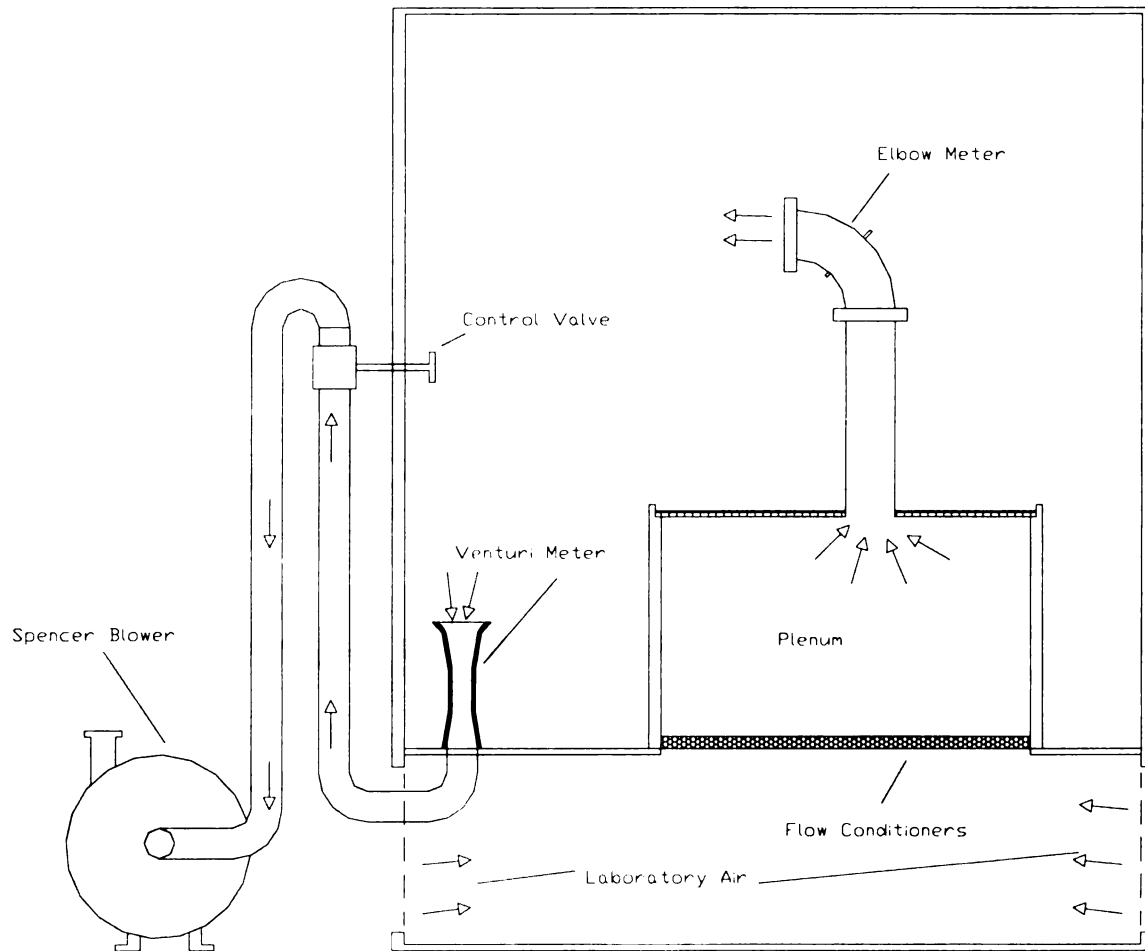
Figure 3.5 FordHaus facility used to calibrate elbow meter

Flow Rate (M^3/min)

$$Q = 5.348 * (P_o - P_i)^{0.5}$$

P$_o$-P$_i$ (cm H$_2$o)
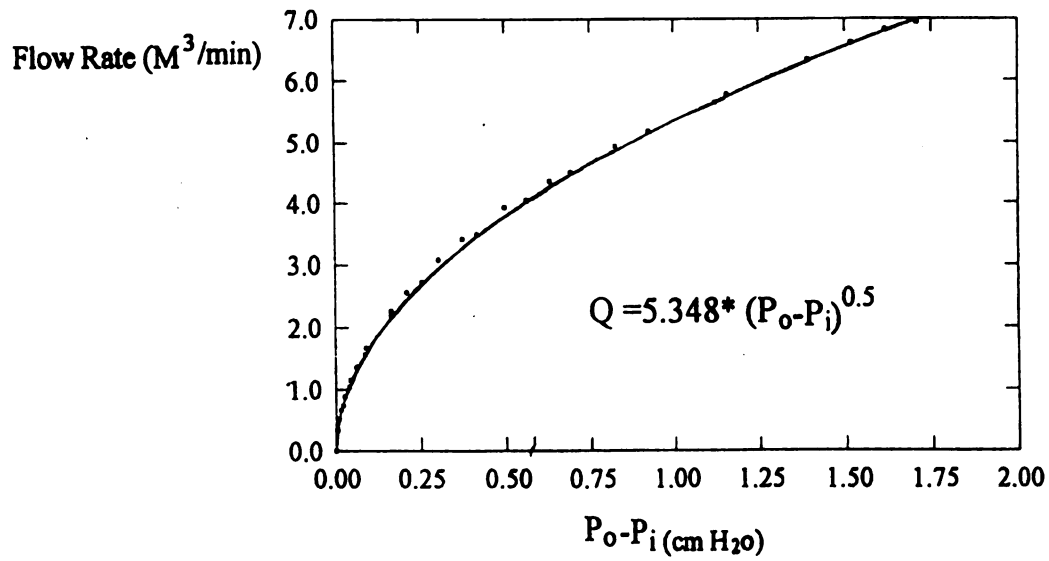
Figure 3.6 Elbow meter calibration data and fit

P$_{shr}$ (Pa)

Data Fit

○ East Meter

◆ West Meter

Q$_{shr}$ (m^3/min)
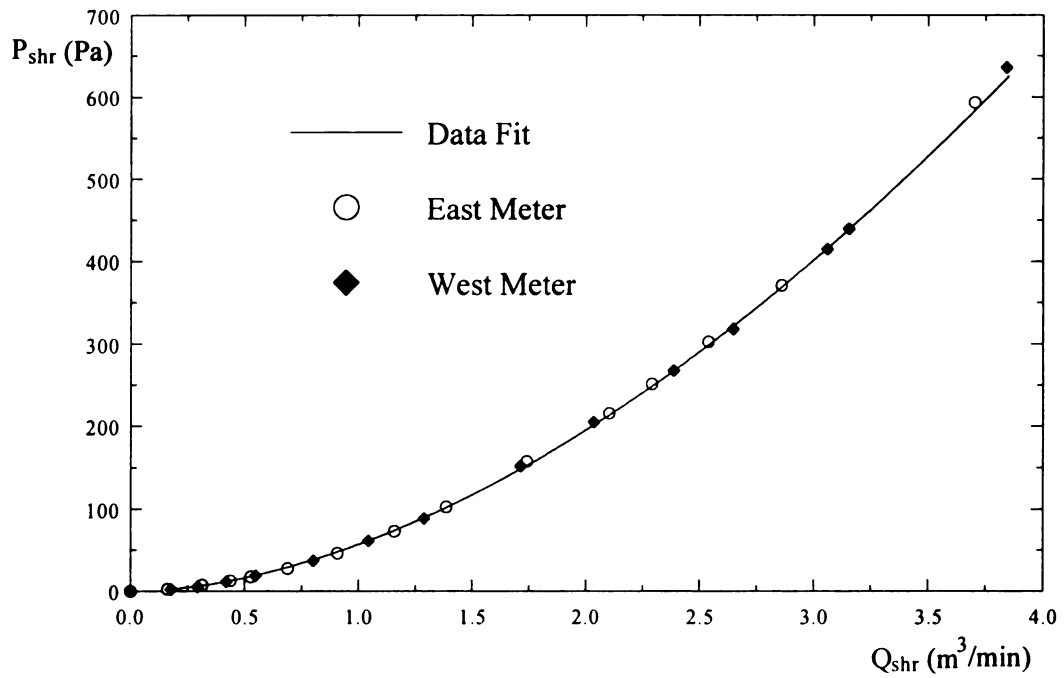
Figure 3.7 Shroud pressure vs. volume to check flow symmetry
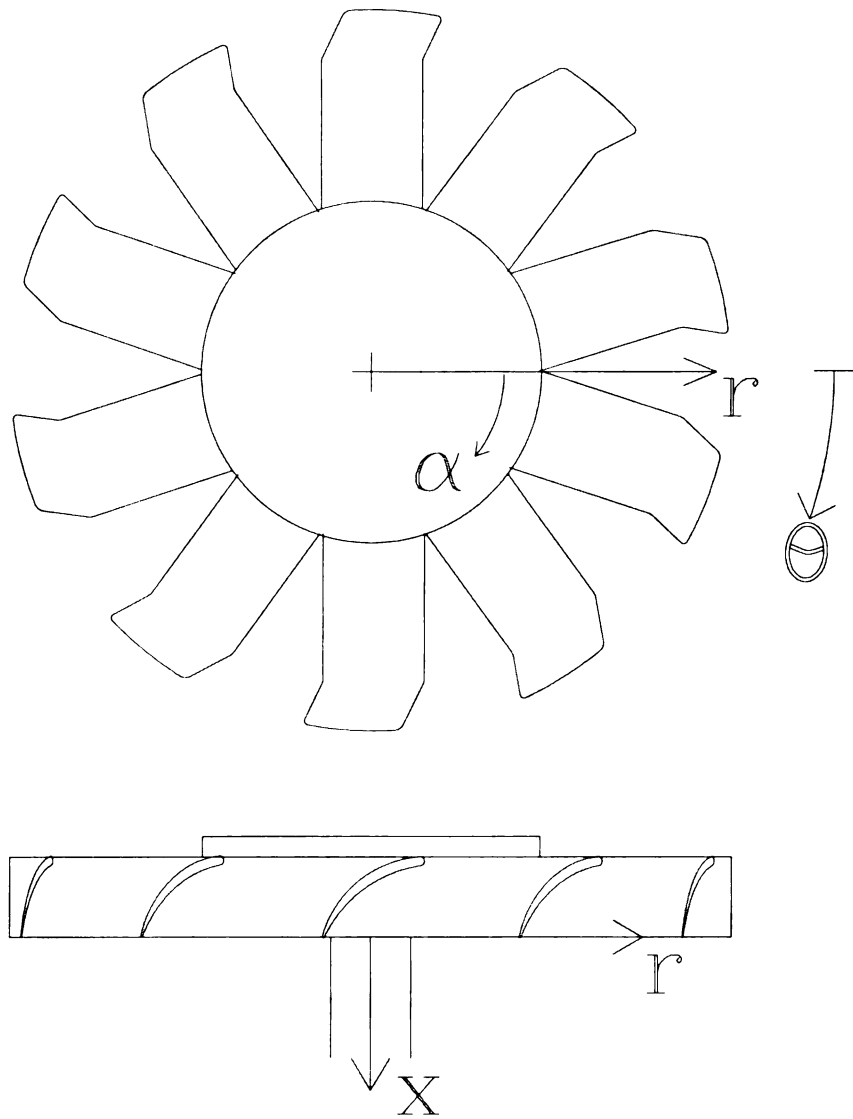
Figure 3.8 Schematic representation of test fan

4. EXPERIMENTAL EQUIPTMENT AND TECHNIQUES

4.1 The ACFRD Facility

The recently constructed Automotive Cooling Fan Research and Development (ACFRD) facility was used for the flow system in this study. The ACFRD was designed to measure both the integral flow quantities (volume flow, pressure rise, and input power) and velocity vectors in the wake of "axial" flow fans. The facility was designed by the author, Professor John Foss of the TSFL, and Mr. John Pakkala[2] of Troy Design Inc, Lansing, Mi.

4.1.1 Overview of facility

The ACFRD facility is shown in Figure 4.1. The test fan (B) and prime mover (I) are responsible for the flow from the laboratory, through the facility, and back to the laboratory. A pressure transducer (0-747 Pa) was used to measure the differential pressure from the atmosphere to the upper receiver (i.e. the pressure rise across the fan: $\Delta P = P_{upper\ receiver} - P_{T\text{-}approach}$) using the tap located at point (C). The air is moved from the upper receiver (F) through two flow metering devices (L-M-P) to the lower receiver (T). The prime mover (I, centrifugal fan: Chicago Blower Co. SQA-36.5) moved the air out of the lower receiver and past a throttle plate. The inlet to the Chicago blower was located at (S) in the lower receiver. The throttle plate was used to control the flow rate through the system.

---

[2] Mr. John Pakkala is currently employed at Capital Machine Design, Lansing, Mi.

The test fan was driven by a vertical shaft, belt drive, and D.C. motor (J) as shown Figure 4.1. A Reliance Electric 11.2 kW (15hp) motor with feedback speed control was used for this drive. The motor speed range was 250 - 1250 rpm. A 1:3 diameter ratio was used for the pulley system to increase the fan speed range to the desired range: 750 - 3750 rpm. The test fan was cantilevered 61.0cm above the shaft supports (D) to avoid aerodynamic blockage of the drive system in the fan wake. Note that the upper 30.5cm of the shaft can be removed for the study of fans which are driven with a built in electric motor. An optical encoder (G) was comprised of a notched disk (mounted on the drive shaft) and an infra-red interrupt circuit; this provided an angular position reference of the fan. The output signal was also used with a frequency counter to accurately set the fan speed. The resolution of the frequency meter was 0.01 hz, corresponding to 0.6 rpm. The feedback speed control typically maintained the specified speed to within ±0.04 hz (2.4 rpm).

4.1.2 Traverse System

A computer controlled traverse was designed and assembled for positioning of the tuft and hot-wire probes in the wake of the fan. A schematic of the traverse is shown in Figure 4.2. All positioning systems were driven by stepping motors controlled remotely from an Intel 486-66 computer. Azimuthal positioning about the fan's axis was provided by a 1.52m diameter steel ring (A). The ring was driven by a stepping motor through a 6/1 pulley system and a 100/1 worm gear box (not shown in Figure 4.2). Two horizontal linear slides (C), (Velmex Inc. #MB4024BJ-S4-20) were mounted to the ring (180° spacing) to provide 51cm of horizontal travel. A 40.5cm vertical slide (E) (Velmex Inc. # MB4024BJ-S4-16) was fixed to each of the two horizontal slides. All four slides used a

20 thread per inch lead screw. The manufacturer quoted repeatability of the positioning was 0.05mm/meter. A probe support fixture which allowed the angular orientation of the probe to be manually set was mounted to one of the aluminum support arms (H); see Figure 4.3. These support arms were given additional vertical strength from linear bearings (I) riding on steel rods (F). The vertical shafts (G) were used to hold the horizontal rods (F) in place. This configuration provided the two arms with linked vertical motion and independent radial motion. All stepping motors were connected to Velmex #NF90-3 controllers that provided the computer interface for the system. The computer commands used to move the probes were called from subroutines written in the 'C' language. These were incorporated into the data acquisition program.

4.1.3 Flow Rate Measurement

A new and unique measurement device has been assembled and tested to measure the volume air flow rate through the ACFRD facility. The wide variety of fan and component geometries to be tested in the facility can be expected to significantly alter the velocity profile entering the metering nozzles. For this reason a point measurement of a characteristic velocity in the nozzle outlet, such as that using Pitot and static pressure measurements, would not provide a reliable experimental technique for the flow rate evaluation. Also, these flow field irregularities negate the option of using a simple nozzle discharge coefficient. The use of thick screens could have been used to "regularize" the velocity profile; however, the pressure drop caused by the screens would have limited the operating capabilities of the facility.

An integral measurement technique was therefore implemented using the device shown in Figure 4.4. Given that the downward flow at the exit of the nozzle (L) is turned

into the horizontal direction at the exit of the turning vane (M), the resultant moment of momentum flux can be used as the quantity that is indicative of the mass flow rate. Specifically, this net flux was balanced by the moment of the force at point (P) acting with respect to the hinge at (R). The magnitude of this force: F_p was measured using a ring type full bridge force transducer. Given the expression for the moment of momentum flux for a control volume (see Figure 4.2) that spans the nozzle exit to the exit of the turning passage:

$$\vec{r}_{R-P} \times \vec{F}_P = \int_{cs} \rho \left[\vec{r} \times \vec{V}\right]\left(\vec{V} \cdot \vec{n}\right) dA \equiv K\left(r_{R-P}\right)\left(\dot{m}^2/\rho A\right) = k'\dot{m}^2 \tag{4-1}$$

one can compute the $\dot{m}$ given the measured force (F_p) and the coefficient k'. Note that K is dimensionless and that k' has dimensions (length^2/mass). Evaluation of k' will be discussed in Section 4.1.3.2. It is relevant to note that the inflow to the control volume contributes to the counter clockwise moment-of-momentum flux (since $\vec{V} \cdot \vec{n} < 0$ and $\vec{r} \times \vec{V}$ is clockwise.) The exit flow also contributes to the net counter clockwise flux (since $\vec{V} \cdot \vec{n} > 0$ and $\vec{r} \times \vec{V}$ is counter clockwise).

The relative insensitivity of the measurement technique to the inflow characteristics from the upper receiver reflects the conditions that the integral, and not point-wise, attributes of the velocity field are represented in the transfer function. Also, the acceleration of the flow from the nozzle exit to the control volume exit will lead to a velocity profile at (P) that is relatively insensitive to the upstream conditions.

4.1.3.1 Details of the Apparatus

Two identical measurement devices exist in the fan testing facility as shown in Figure 4.1. This design allowed a symmetric delivery of air from the upper receiver to

the lower receiver, as well as to provide a redundant measurement of the flow rate (see section on calibration).

A set of three delivery nozzles directs the air vertically downward from the upper receiver toward the turning vane for each of the two metering passages. The nozzle assemblies consist of a screen entrance and a one sided contraction as shown in Figure 4.4. The former consists of a ¼ circle (r=0.406 m) of coarse wire mesh to support a cheese cloth filter. Thin filters were used to prevent wind drafts of the upper receiver from influencing the flow in the nozzles. An elliptical shaped contraction with a 3/2 axis ratio was used to provide a 4/1 contraction in flow area. The exit flow area for both sets of nozzles was 0.310 m².

The measurement device consists of an aluminum sheet rolled to a 0.406m radius. The shape of the curved surface is rigidly held by plywood side walls. This assembly (M) is supported on one side by two 0.20 m wide knife edge pivots (R); this design provides less friction moment than a bearing support. The outflow side of the unit was supported by a counter balance (N) and force transducer (P). The counter balance was also mounted on a knife edge support as shown in Figure 4.4. Adjustable steel plates were used to offset the weight of the turning vane assembly. A ring type full bridge force transducer was connected between a rigid beam and the turning vane to measure the reaction force of the air flow. The moment was then inferred from this force. The ring was constructed from aluminum with the dimensions: 51mm in diameter, and 1.0mm thick. Four 350 ohm stain gages were fastened to the ring and connected to a bridge circuit using an instrumentation amplifier. Adjustment screws were used to set the maximum deflection of the device to limit the maximum strain of the transducer.

4.1.3.2 Airflow Meter Calibration

Calibration of the force transducer outputs was necessary to compute the flow rate from the two measured voltages. A set of four metering nozzles were placed at the roof level of the facility in place of the test fan. The mass air flow rate through the system was determined from the equation:

$$\dot{m} = \rho \times N \times A_{nozzle} \times C_d \sqrt{\frac{2}{\rho}\left(P_{atm} - P_{receiver}\right)} \qquad (4\text{-}2)$$

where N is the number of calibration nozzles used, and C_d is a known discharge coefficient of the nozzles. Initial investigations indicated that the interaction of the two metering systems when operated together caused biased results when compared to data taken with the independent operation of the metering systems. Therefore, both force transducers were calibrated simultaneously using the total flow rate. This technique assumes that the fraction of the total flow rate in each of the measurement devices during the calibration process is identical to that in an actual fan test. Data to be presented in Section 4.1.3.3 show this to be an acceptable assumption. As a result, two independent estimates of the total flow (Q_s) and (Q_n) rate are obtained (the subscripts 'n' and 's' refer to the metering device on the south and north side of the ACFRD facility). The actual flow rate is assumed to be the mean of these:

$$Q_{measured} = \frac{Q_n + Q_s}{2} \qquad (4\text{-}3)$$

A range of flow rates was established using the auxiliary fan and throttle combination to obtain the calibration data. The voltage output from the two force transducers was measured using a PC based A/D system described in Section 4.2. Assuming that the force transducers are linear (the output voltage is proportional to the applied force), it

follows from equation (4-1) that the flow rate is proportional to the square root of the voltage. Time series data acquired were then averaged and curve fit to the functions:

$$Q_n = 3.165\sqrt{E_n} + 0.0531 \tag{4-4}$$

$$Q_s = 2.978\sqrt{E_s} - 0.0094 \tag{4-5}$$

where E_n and E_s represent the average voltages measured from the transducers on the north and south sides of the facility respectively; Q is calculated in units of m^3/s. The calibration data and linear curve fit of the data is shown in Figure 4.5 and Figure 4.6.

4.1.3.3 Test of Flow Rate Measurement Device

A test fan with a well established characteristic curve (a cooling fan from a 1994 Ford Explorer) was used to validate the technique and calibration. The performance was measured using the following procedure:

i) the fan rotational speed is set to a constant value,

ii) the back pressure created by the fan was varied with the auxiliary fan and throttle plate,

iii) time series data for the force transducer outputs as well as the pressure of the upper receiver were recorded using the A/D system.

The time series data were averaged for the T = 10 seconds of data taken at 1,000 Hz. Equation (4-3) was then used to infer the flow rate. Performance data were acquired at several fan speeds and made dimensionless using equation (2.2). It was decided that scaling performance data would provide a quantitative check on both the repeatability and accuracy of the flow metering device. Specifically, the data would not collapse properly if the measurement device was not accurately measuring the flow rate. Two performance

curves were acquired for speeds of 1400 and 1600 rpm. Data supplied by the fan manufacturer was taken at 1500 rpm. These results are presented in Figure 4.7. The data indicate that the metering device is working properly. The differences between the two data sets obtained in the ACFRD are quite small (a 2% difference in flow rate at a given pressure rise was typical). Larger deviations observed over the middle flow rate range $(0.15<\phi<0.18)$ are suspected to be a result of the fan stall phenomena being sensitive to the Reynolds number $(U_{tip}D_{fan}/\upsilon)$. The data taken in the ACFRD facility agreed in general with the manufacturers data. However, larger deviations are observed. Typical agreement for the larger flow rates was within 7%. The large differences noted for the smallest flow rates are suspected to be a result of slight differences in geometrical boundary conditions used and not an error in the flow metering device. Specifically, it has been observed that the performance characteristics of cooling fans are extremely sensitive to the geometry and location of the shroud due to the radial outflow of the fan at low flow rates; see Chapter 6 and Baranski (1977).

The proper collapse of the scaled data indicates that flow rate measurement device should provide accurate results for the flow range of interest. The uncertainty in the performance data presented in Chapter 5 is estimated to be ±2.0% of the flow rate for a given fan pressure.

4.1.4 Power Drive and Measurement

The power input to the fan was measured using the electrical circuitry shown schematically in Figure 4.8. This device provides voltage signals 'v' and 'i' which are proportional to the drive motor voltage and current respectively. The 'v' signal was made proportional to the motor voltage signal by connecting a 100:1 voltage divider to the

motor's power lines. The '*i*' signal was made proportional to the motor current using a hall effect current meter (F.W. Bell Model CL-100). To measure the input power, time series data of signals '*v*' and '*i*' were acquired at 1000 hz for 10 seconds. The power delivered to the fan was then computed from:

$$P_{fan} = k\left[P_{system} - P_{losses} \right] = k\left[\sum_{i=1}^{n}(v \cdot i)_i - \sum_{i=1}^{n}(v_o \cdot i_o)_i \right],$$

(4-6)

where n is the number of samples taken (10,000). The quantity (P_{losses}) represents the power losses of the drive system which are a function of the fan rotation speed. This was recorded before and after each experiment by removing the cooling fan and recording the motor power as above. These two estimates were averaged for use in equation (4-6). Initial investigations indicated the presence of transient drive losses for approximately 15 minutes when the facility was "cold"; therefore, the drive system was operated for 20 minutes prior to an experiment to bring the drive motor and shaft bearings to thermal equilibrium.

The constant k was determined by comparing data from the test fan's manufacturer to the data acquired in the ACFRD. Data were acquired for rotational speeds of Ω=1400 and 1600 rpm. The manufacturer's data were acquired at Ω=1500 rpm. For comparison, the data acquired at 1400 and 1600 rpm were scaled according to the equation:

$$P_{fan}(\Omega = 1500) = P_{fan}(\Omega) \cdot \left(\tfrac{1500}{\Omega} \right)^3,$$

(4-7)

where N represents the fan speed at which the data were acquired. Note that equation (4-7) can be found in Baranski (1977). A least squares approach was then used to solve for k. The value was found to be 0.26 to obtain units of kilowatts. Figure 4.9 shows the data taken for this test plotted as a function of the flow rate. The largest difference in

power between the ACFRD data and the manufacturers data is 3% for $Q_{fan}>0.9$ m³/s. Differences in power for the lower flow rates range from 3 - 9%. The largest difference realized between the two data sets acquired in the ACFRD facility was 3.2%. The larger differences observed between the manufacturers data at the lower flow rates is believed to be a result of the sensitivity of the flow field to slight differences in boundary conditions. The overall uncertainty of the measurement technique is estimated to be 3% of the actual power.

4.2 Data Acquisition and Processing System

An Analogic Fast-16 plugin board and an Intel 486-66 were used to acquire data. The maximum possible data rate was 1 Mhz. An 8 channel "sample-and-hold" was used for simultaneous sampling. The resolution of the A/D conversion was 16 bits, with a range of ±10 volts. The electrical noise of the system (tested by connecting a short circuit to the input) was typically 0.3 mv, or 1 bit. The A/D card contained 10^6 samples of onboard memory. If more than 10^6 data samples in a given time series were required, independent "bursts" of data were sequentially sampled. All data were transferred to a DEC ALPHA αXP-150 computer system for processing.

4.3 Pressure Transducers

Three Validyne DP15-20 pressure transducers were used to measure the ΔP_{fan}, ΔP_{shr}, and Q_{shr} (as described in Section 3.2). The linear calibration constants for these were 0.842, 2.91, and 0.068 respectively. These calibrations were checked before and after all experimental data were acquired and found to be invariant to within 1%.

4.4 Tuft Probe Measurements

The tuft consisted of a 15mm segment of white yarn supported by a thin thread which is held in place be a sewing needle. A small hole was drilled into a ¼" aluminum shaft such that the needle could be press fit into the shaft. This design was used to minimize the effect of the tuft support on the local flow characteristics.

Images of the tuft were acquired using a Dycam DC-10 digital camera to document the time mean angle of the flow. The camera had 24 bit color resolution, with a maximum of 640x480 pixel resolution. A black background was used to hold white arrows for angular reference in the photographs. The angular excursion limits of the tuft were measured using digital image analysis software. Specifically, the reference angles that were placed in the background allowed the two angles, corresponding to the extremes of the tuft excursion, to be measured with respect to the (r, θ, x) coordinate system. The time mean flow direction was assumed to be the angle centered between the excursions.

The ability of the tuft probe to provide an accurate estimate of the mean flow angle varies depending on the flow field. Specifically, extremely high turbulence levels $\tilde{u}/\overline{U} > 1.0$ and highly reversing flows can cause unreliable results. However, for flow conditions where the velocity is nominally unidirectional, the tuft provides an accurate measure of the time mean flow angle often to within 5 degrees.

4.5 Velocity Field Measurements

This section presents the measurement procedure, calibration method, and data processing algorithms used in the acquisition of quantitative velocity data in the wake of the cooling fan and aerodynamic shroud. A probe using two hot-wires configured in an

X-array was used to acquire these data. The probes used were fabricated in the TSFL[3]. The X-array consisted of two tungsten wires mounted 1mm apart and at a nominal angle of 45° with respect to the probe axis. The wire consisted of a 3mm long 5μm diameter wire with a 1mm active region. Copper plating was used to cover the 1mm of wire on either side of the sensor. A schematic of the probe used is shown in Figure 4.10.

The data were taken using two DISA 55m10 anemometers. The electrical noise levels were typically 2 mvolts RMS. The frequency response was always in excess of 30 Khz for a flow speed of 20 m/s. This permitted flow properties that are of the order 0.67mm to be evaluated. All hot-wire data were temperature compensated to account for ambient changes in the laboratory air temperature. A thermistor with 2.03 K/Kohm sensitivity was used to measure the air temperature during calibration and data acquisition procedures.

4.5.1 Measurement Procedure

The angular orientation of the probe was aligned with the mean flow directions measured from the tuft observations. Histograms of the incident flow angle (γ) with respect to the probe's axis were calculated for each of the spatial locations measured. If the probe was correctly aligned with the mean flow, the histogram would reveal a 'centered' profile as shown in Figure 4-11. If the probe was improperly aligned, the histogram would be shifted; see e.g. Figure 4.12. The magnitude of the shift was then used to re-align the probe, and the data were retaken.

---

[3] Turbulent Shear Flows Laboratory, Michigan State University.

Stochastic values for the three components of the velocity vector were acquired by rotating the X-array probe about its axis for each measurement. This technique provides a single measurement of $\bar{v}$ and $\bar{w}$ (velocity components normal to the probe axis) and a redundant measurement of $\bar{u}$ (velocity component aligned with the probe axis). The angular orientation of the probe (i.e., the ζ and ξ angles of Figure 4.3) were used to compute U_x, U_r, and U_θ from the u, v, and w components measured. This calculation was simplified by the fact that $\xi=0$ was used for the measurements reported herein. Specifically, the velocity vector expressed in the (r, θ, x) coordinates are related to the probe coordinates by:

$$U_x = \sqrt{u^2 + v^2} \, \sin(\zeta + \gamma) \qquad (4\text{-}8)$$

$$U_\theta = \sqrt{u^2 + v^2} \, \cos(\zeta + \gamma) \qquad (4\text{-}9)$$

and

$$U_r = w \qquad (4\text{-}10)$$

where γ is the instantaneous flow angle with respect to the probe.

4.5.2 X-array calibration

The air velocity magnitude and direction with respect to the probe axis are defined as Q and γ respectively as shown in Figure 4.10. (Note that Q represents the air velocity at the probe tip; it is not related to the flow rate of the fan used in earlier sections. This notation is used to follow what is typically used in hot-wire literature.) An iterative processing algorithm known as the "speed wire - angle wire" technique (Foss et. al (1995)) was used to infer Q and γ given simultaneous measurements of the anemometer voltage outputs E_+ and E_-. Note the subscripts + and - refer to the $+\beta$ and $-\beta$ sensors of Figure 4.10. This technique requires calibration data to obtain $E_+(Q,\gamma)$ and $E_-(Q,\gamma)$. These calibration data were acquired for 8 flow speeds in the range $0.1U_{tip} < Q < 1.2U_{tip}$,

where U_{tip} represents the maximum velocity that would be expected in the flow field. For each speed setting, data were acquired for a range of $-36 < \gamma < +36$ degrees in 6 degree steps. These data were fit at each calibration angle to the modified Collis and Williams equation:

$$E_+^2(Q,\gamma) = A_+(\gamma) + B_+(\gamma)Q^{n_+(\gamma)} \tag{4-11}$$

and,

$$E_-^2(Q,\gamma) = A_-(\gamma) + B_-(\gamma)Q^{n_-(\gamma)}. \tag{4-12}$$

The coefficients A,B and n were found for each of the 13 values of γ by computing a least squares linear fit of the data as n varied from 0.2 to 0.7. The most linear data fit was determined by choosing the n value which provided the smallest value of the standard deviation of the fitted function:

$$StDev = \left(\frac{1}{N}\sum_1^N \left(Q_{calculated} - Q_{measured}\right)^2\right)^{\frac{1}{2}}. \tag{4-13}$$

A new variable was defined to obtain a relationship between the wire voltages and the flow angle (γ) for a given speed. Specifically, $\eta(\gamma)$ at a fixed Q is defined as

$$\eta(\gamma) = \frac{E(Q,\gamma)}{E(Q,\gamma=0)} - 1 \tag{4-14}$$

for each wire. Using equations (4-11) and (4-12), $\eta(\gamma)$ was evaluated at even speed increments for a total of 51 speeds in the range of the calibration data. A fifth order polynomial was used to fit the data computed with equation (4-14). Figure 4.13 shows an example of the $\eta(\gamma)$ curve fit at a flow speed of 20m/s.

A final calculation was made using the calibration data to estimate β_+ and β_- for the two wires. It can be shown (Bohl (1996)) that β for each wire can be found by evaluating the function

$$\beta = \tan^{-1}\left(\frac{dE^2}{d\gamma}\middle/(E^2 - A)n\right) \tag{4-15}$$

at $\gamma=0$. A second order fit of E^2 versus γ was differentiated to evaluate equation (4-15) for each calibration.

4.5.3 Evaluation of Q and γ

The speed and angle of the air velocity were determined using the "speed wire/angle wire" technique. This iterative technique assumes that the wire which is more perpendicular to the flow (i.e., lower value of β-γ) is more sensitive to the air speed (Q), and the wire which is more parallel to the flow (i.e., larger value of β-γ) is more sensitive to the oncoming flow angle (γ). The algorithm requires that initial estimates of Q and γ to be made. These are computed using the cosine law. Specifically, the u and v components were estimated by the functions:

$$Q_{eff+} = u\cos(\beta_+) + v\sin(\beta_+) \tag{4-16}$$

and

$$Q_{eff-} = u\cos(\beta_-) + v\sin(\beta_-). \tag{4-17}$$

The effective cooling velocity Q_{eff} was determined for both wires from

$$Q_{eff+} = \cos\beta_+ \left[\frac{E_+^2 - A_+(0)}{B_+(0)} \right]^{\frac{1}{n_+(0)}} \tag{4-18}$$

and

$$Q_{eff-} = \cos\beta_- \left[\frac{E_-^2 - A_-(0)}{B_-(0)} \right]^{\frac{1}{n_-(0)}} \tag{4-19}$$

where the coefficients A, B and n used were evaluated at $\gamma=0$.

The initial values used in the algorithm are calculated from

$$Q_{old} = \sqrt{u^2 + v^2} \tag{4-20}$$

and

$$\gamma_{old} = \tan^{-1}\left(\frac{v}{u}\right). \tag{4-21}$$

Note that the wire which has the larger initial computation of Q_{eff} determines which wire will be treated as the "speed wire" and which will be the "angle wire."

A new estimate for the speed, Q_{new}, was calculated from the A, B, and n values from the speed wire calibration closest to γ_{old}. The variable η was then evaluated for the angle wire using equation (4-14). Two estimates of the new flow angle were made using the two γ versus η curves closest to the flow speed Q_{new}. The next value of γ_{new} was

determined by linear interpolation between the two angles based on flow speed. The new estimates of Q and γ were then used as the initial guess for the next iteration. For this work, 15 iterations were used to ensure convergence.

4.5.4 Uncertainty Considerations

The hot-wires used were calibrated before and after each experiment. The maximum time between calibrations was 3 hours to ensure that "drift" would not contaminate the measurements. The standard deviation of the calibration as calculated from equation (4-10) was typically less than 0.04m/s (0.14% of full scale). Typical maximum values for the standard deviation were 0.3m/s (1.0% of full scale); these occurred at the extreme angles of the calibration where the wire is nearly parallel to the velocity vector.

The calibration drift was estimated by processing the data sets with the "pre" and "post" calibrations independently and comparing the results. If the difference between the data processed with the two calibrations was greater than 2% of the measured value then the data set was discarded and the experiment was repeated.

The ability of the X-array and processing routine to calculate the speed and angle of the flow was tested. Specifically, time series data from the calibrations were processed to compute the speed and angle of the velocity. The results were compared to the known speed (from the pressure measurement) and angular orientation of the probe in the calibration. Typical agreement in flow speed was within 1%. The deviation in angle was usually within 0.15 degrees for -24<γ<24 degrees. For $24 < |\gamma| < 36$ typical deviation was within 3 degrees (See Foss et. al (1995)).

An additional source of error in the hot-wire measurements is the existence of the velocity component normal to the plane of the X-array. The probe was aligned with the mean flow angle measured from the tuft measurements to minimize the time average of

the normal component. However, instantaneous component of velocity normal to the plane of the X-array will cause a "binormal" cooling which will yield an overestimate of the true velocity magnitude. No attempt was made to compensate for the binormal cooling in this work. The error introduced by this can be estimated to be a "cosine" effect. Specifically, the speed wire responds to the vector addition of the desired value (Q), and the binormal component (*w*). For example, if w is of order 20% of the velocity component in the plane of the X-array (i.e. w/Q=0.2) then the error in Q will be 1.9%. The maximum average value of w/Q measured is about 0.30 corresponding to an overestimate in Q of 5%. More typical values of w/Q<0.15 were recorded which would cause an uncertainty of only 1%.

4.5.5 Time Averaged and Phase Averaged Calculations

Time series data were acquired in the wake of the fan were processed to provide statistics based on time averaged and phase averaged calculations. The time mean of velocity was defined as:

$$\overline{U}(x,r,\theta) = \frac{1}{N}\sum_{j=1}^{N} U_j \, . \tag{4-22}$$

The standard deviation of velocity is

$$\tilde{U}(x,r,\theta) = \left(\frac{1}{N-1}\sum_{j=1}^{N}\left(U_j - \overline{U}\right)^2\right)^{\frac{1}{2}} \, . \tag{4-23}$$

Phase averaged mean and RMS of velocity are calculated from

$$<\overline{U}>(x,r,\theta,\alpha) = \frac{1}{N}\sum_{j=1}^{N} U_j\left(jT + t_\alpha\right) \tag{4-24}$$

and

$$< \widetilde{U} > (x,r,\theta,\alpha) = \sqrt{\frac{\sum_{j=1}^{N}\left[U_{j}\left(jT+t_{\alpha}\right)- <\overline{U}>(x.r.\theta,\alpha)\right]^{2}}{N-1}} \qquad (\ 4\text{-}25)$$

respectively, where α is an angular coordinate measured from a fixed point on the rotating fan. In these equations the time for one complete revolution of the fan is written as T. The symbol t_{α} is the phase lag for a given angle of $0 < \alpha < 360°$ such that $0 \le t_{\alpha} < $ T. Past investigators of rotating machinery have used similar phase averaging techniques; see Lakshminarayana (1981).

Another quantity used to analyze the velocity data is the phase averaged vorticity. The phase averaged axial component of vorticity in a cylindrical coordinate system is given by

$$< \omega_{x} > (x,r,\theta,\alpha) = \frac{1}{r}\left(\frac{\partial (r < \overline{U}_{\theta} >)}{\partial r} - \frac{\partial < \overline{U}_{r} >}{\partial \theta}\right). \qquad (\ 4\text{-}26)$$

The partial derivative terms of equation (4-26) were approximated using a second order finite difference scheme. The interior points were calculated using a central difference (see Anderson (1984)):

$$\left.\frac{\partial a}{\partial h}\right)_{i} = \frac{a_{i+1} - a_{i-1}}{2\Delta h}, \qquad (\ 4\text{-}27)$$

and the boundary points were calculated with a forward difference:

$$\left.\frac{\partial a}{\partial h}\right)_{i} = \frac{-3a_{i} + 4a_{i+1} - a_{i+2}}{2\Delta h}, \qquad (\ 4\text{-}28)$$

where Δh is the distance between data points.

The data rate at which time series of velocity were acquired was 6.0kHz, corresponding to every 1.0 degrees of fan rotation. A total of 324000 samples were acquired to build the statistical population for 900 fan revolutions (54 seconds of data for a fan speed of 1000 rpm) Statistical convergence of all phase averaged quantities was checked. An example of the statistical convergence of the mean velocity computed from equation (4-24) is shown in Figure 4.14.
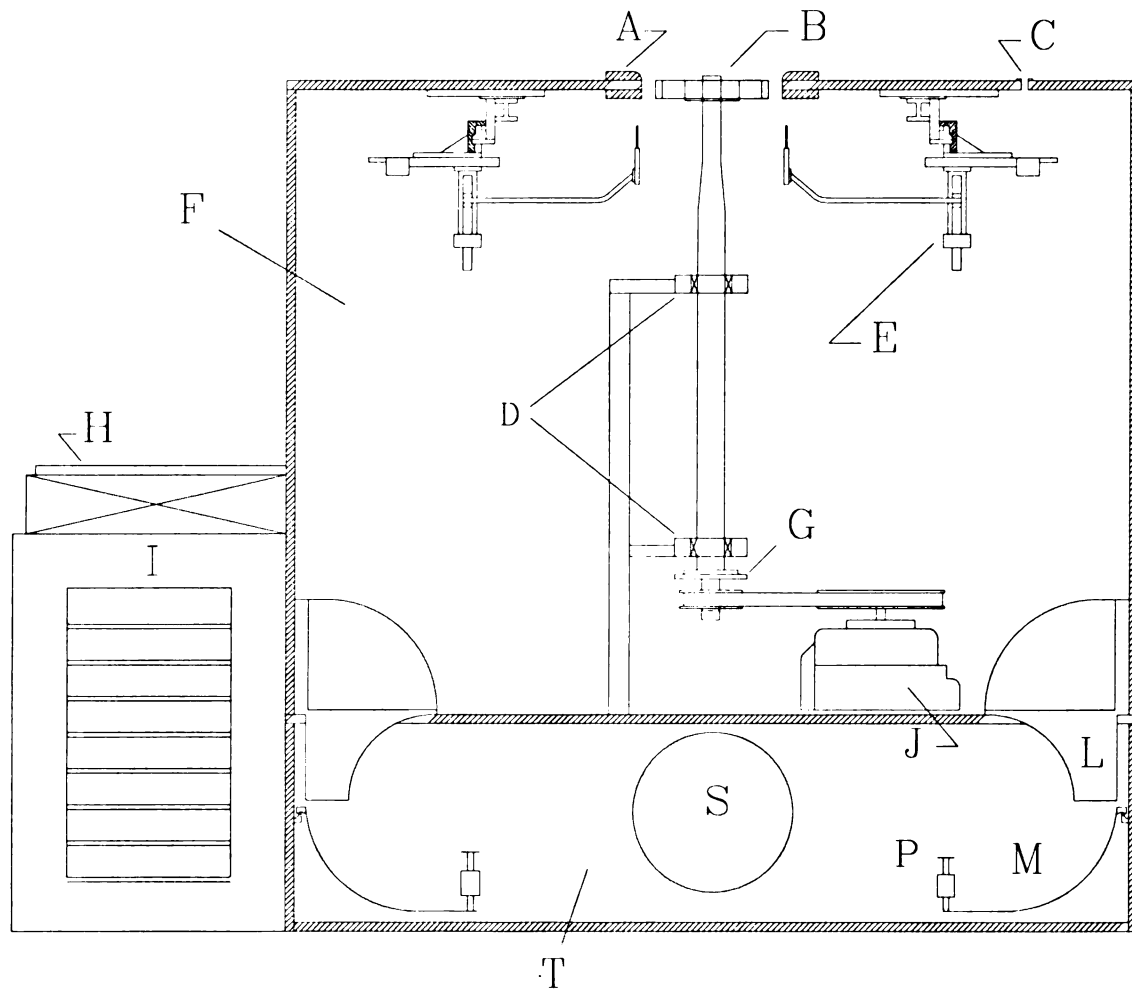
A	AXISYMETRIC SHROUD	H	THROTTLE PLATE
B	TEST FAN	I	PRIME MOVER
C	PRESSURE TAP	J	DRIVE MOTOR
E	TRAVERSE	L	NOZZLE
F	UPPER RECEIVER	M	TURNING VANE
D	BEARING SHAFT SUPPORTS	P	FORCE TRANSDUCER
		S	INLET TO PRIME MOVER
G	OPTICAL ENCODER	T	LOWER RECEIVER

Figure 4.1Schematic of the ACFRD Facility
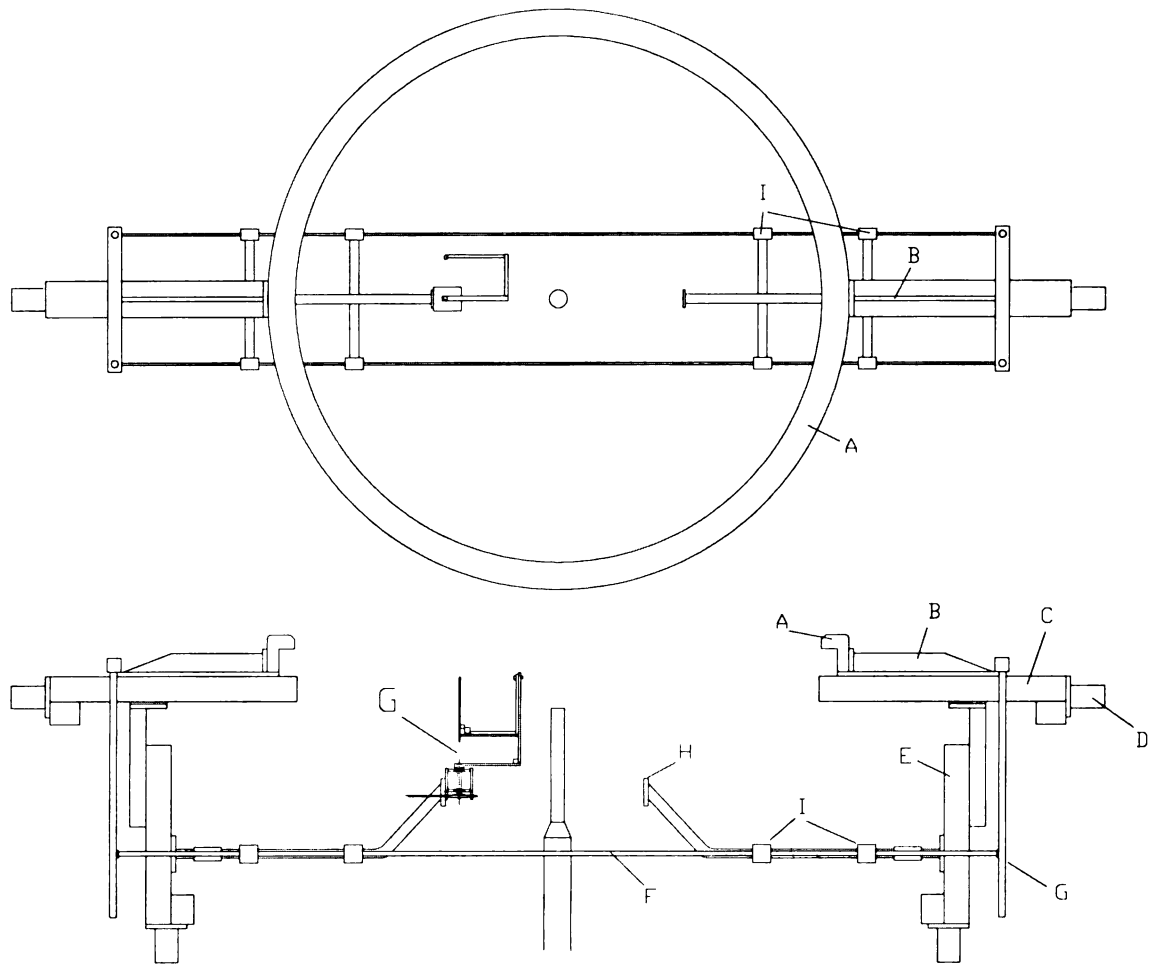
A	Azimuthal Traverse Ring	F	Cross Support Rod
B	Horizonal Slide Bracket	G	Vertical Stopper Rod
C	20" Horizontal Slide	H	Probe Mount
D	Stepping Motor	I	Linear Bearings
E	16" Vertical Slide	G	Probe support Swing

Figure 4.2 Schematic of Traverse Used in the ACFRD
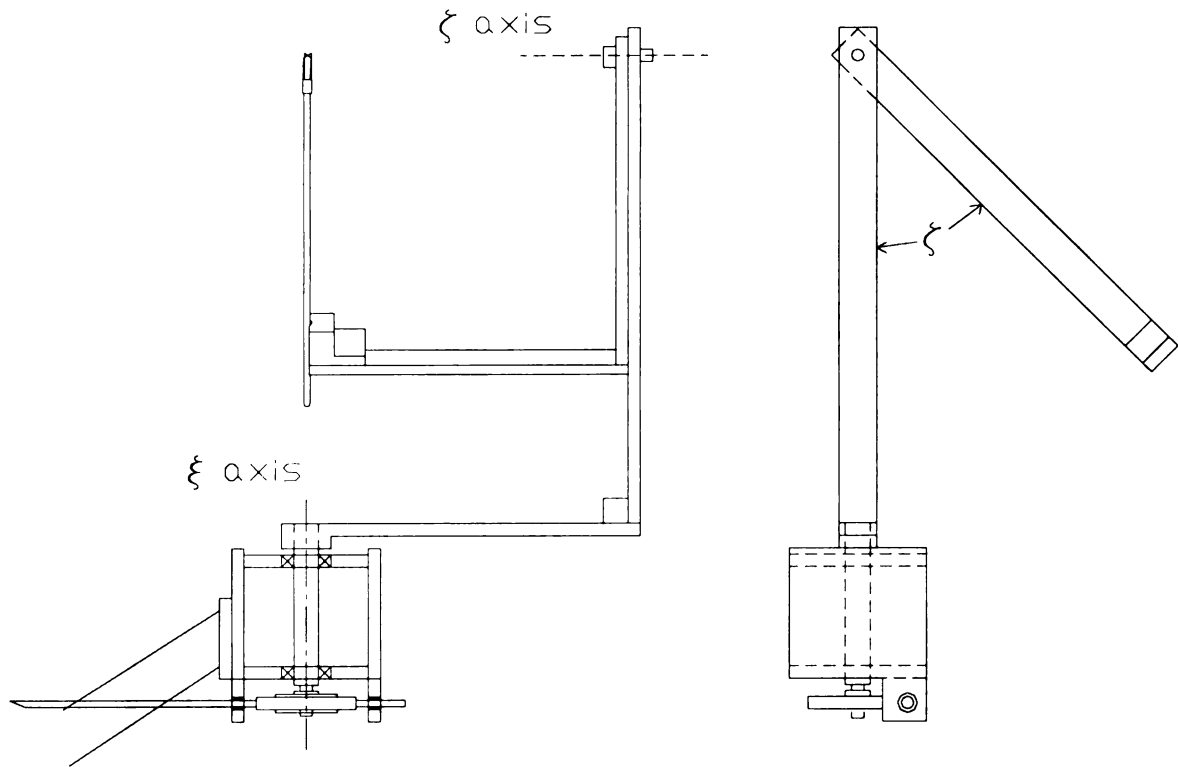
Figure 4.3 Schematic of Probe Holder
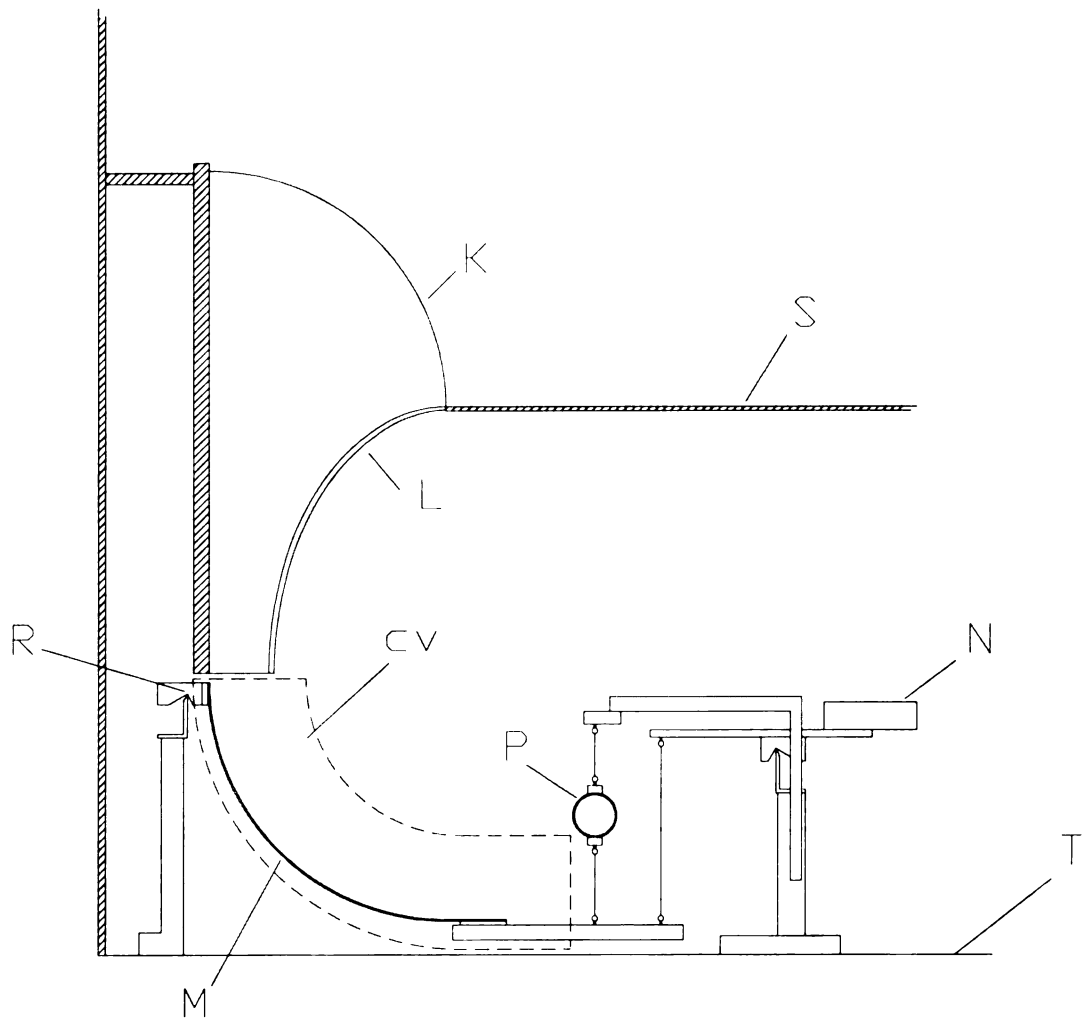
K   Inlet Filter
L   Ellipse Nozzle
M   Turning Vane
N   Counter Balance
P   Force Transducer
R   Knife Edge Pivot
S   Reciever Floor
T   Floor of Lower Reciever

Figure 4.4 Schematic of Flow Metering Device
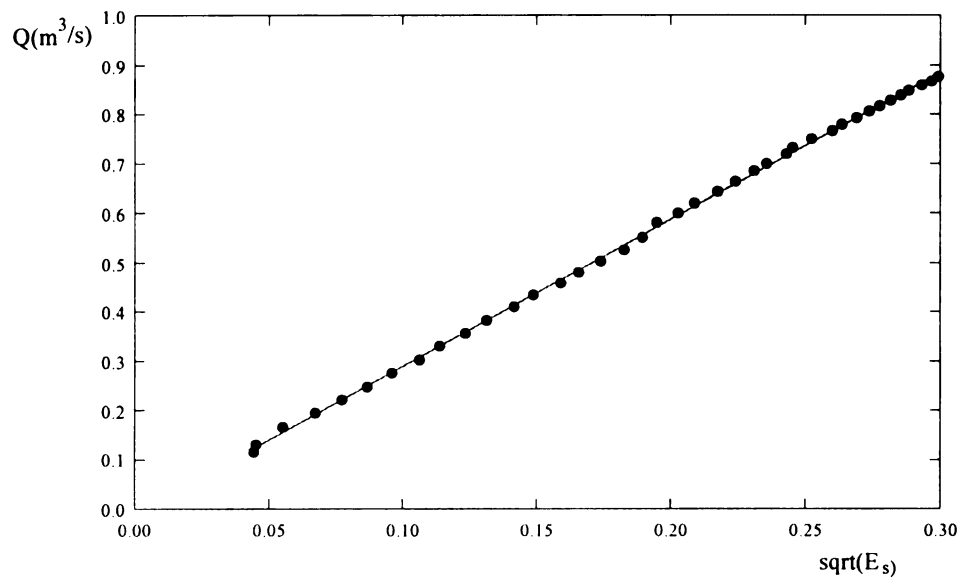
Figure 4.5 Calibration and Fit for South Side Flow Meter
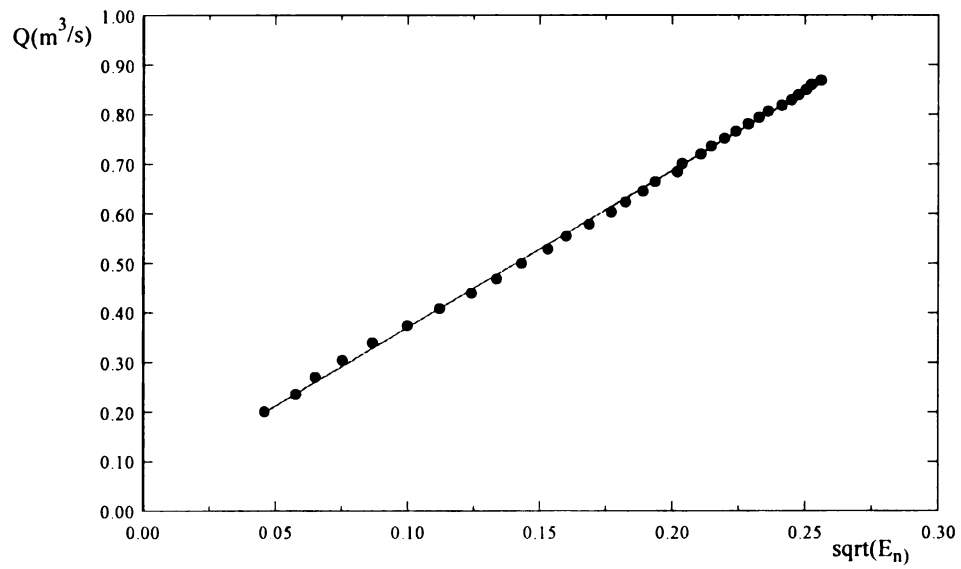
Figure 4.6 Calibration and Fit for North Side Flow Meter
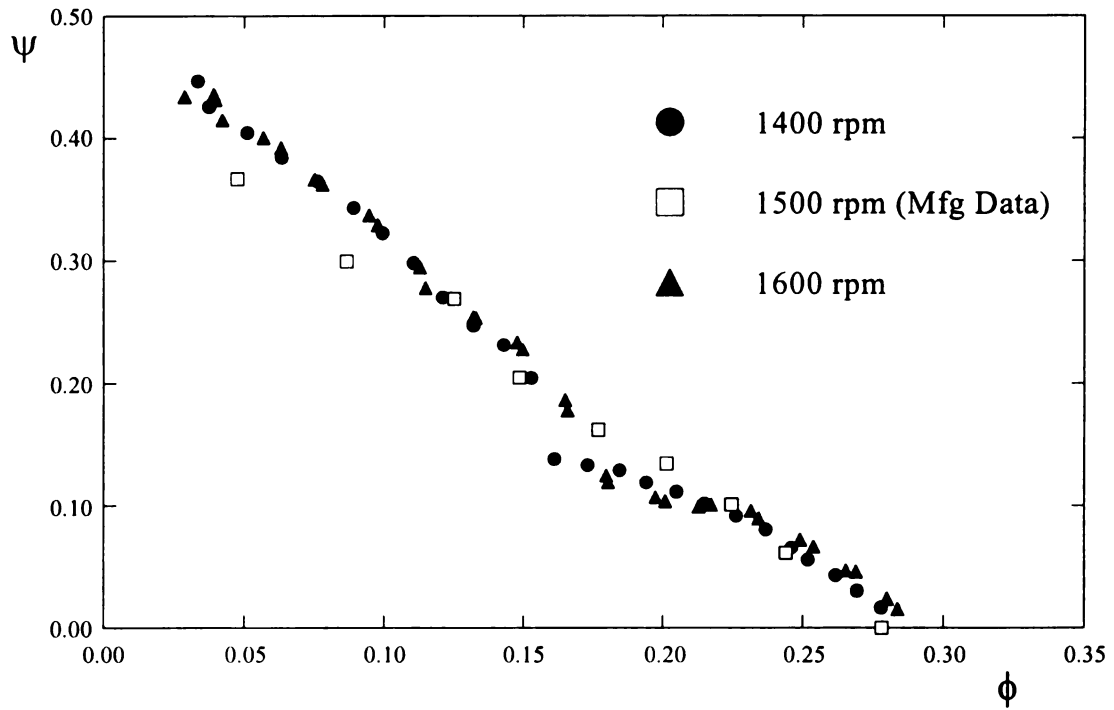
Figure 4.7 Flow Meter Test Data
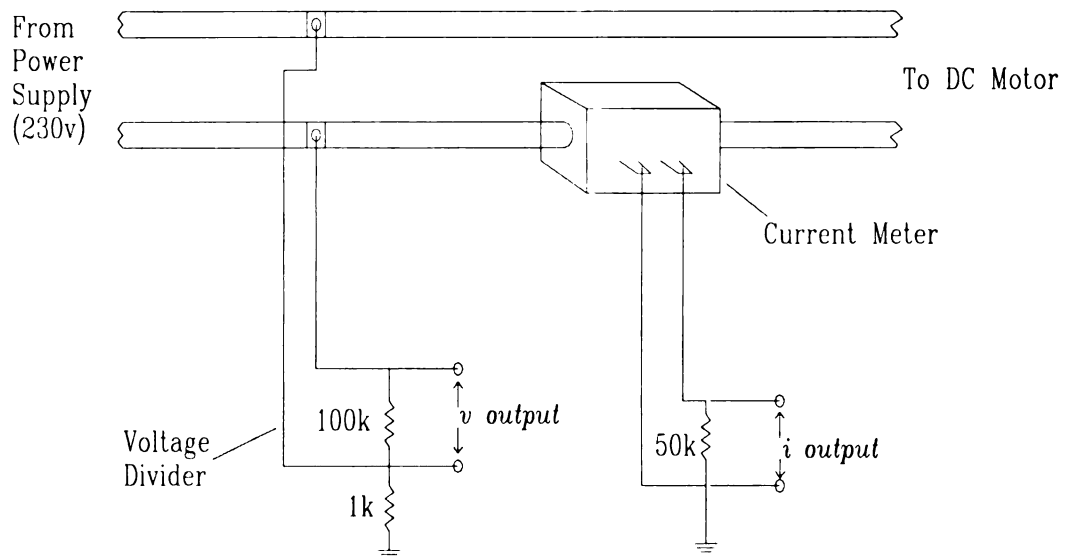
Figure 4.8 Schematic of Power Measurement Circuitry
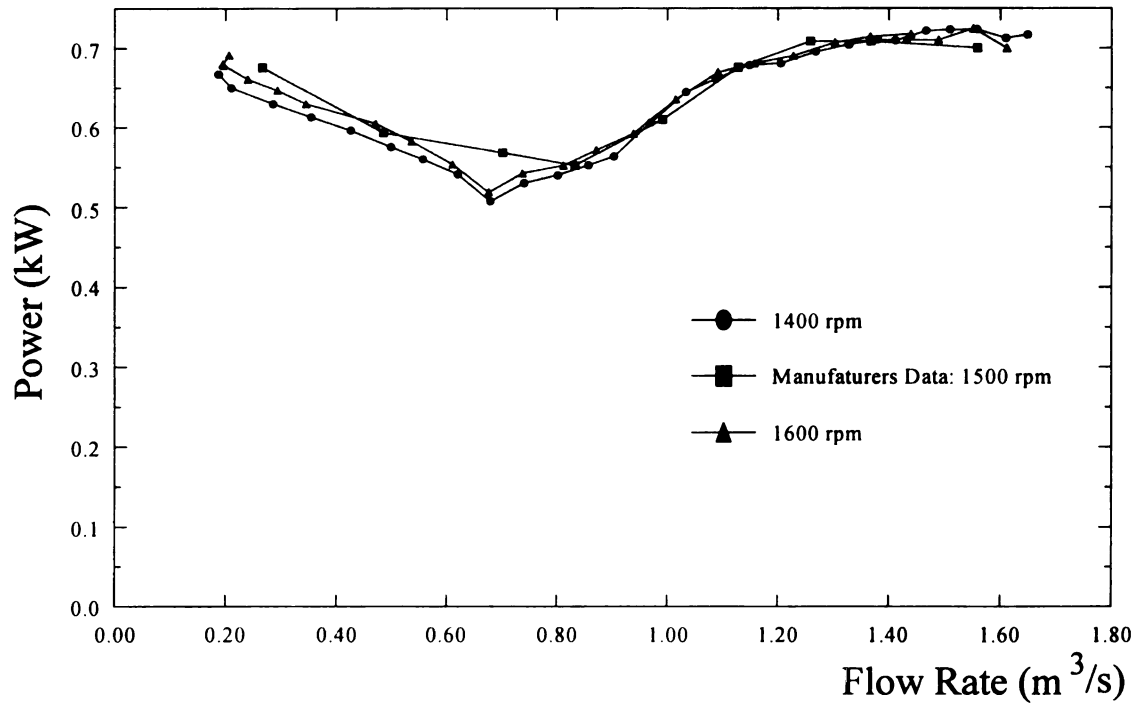
Figure 4.9 Power Measurement Test Data

a) FRONT VIEW   b) SIDE VIEW
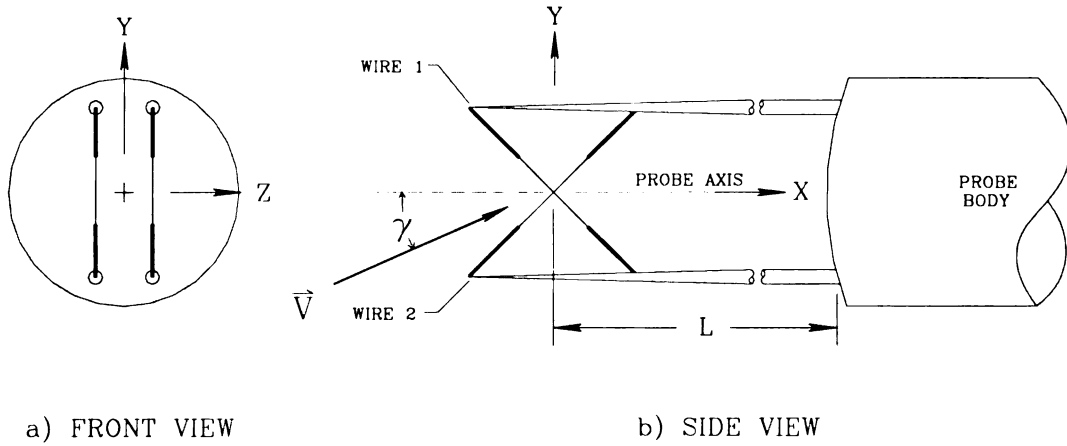
Figure 4.10 Drawing of an X-array Probe
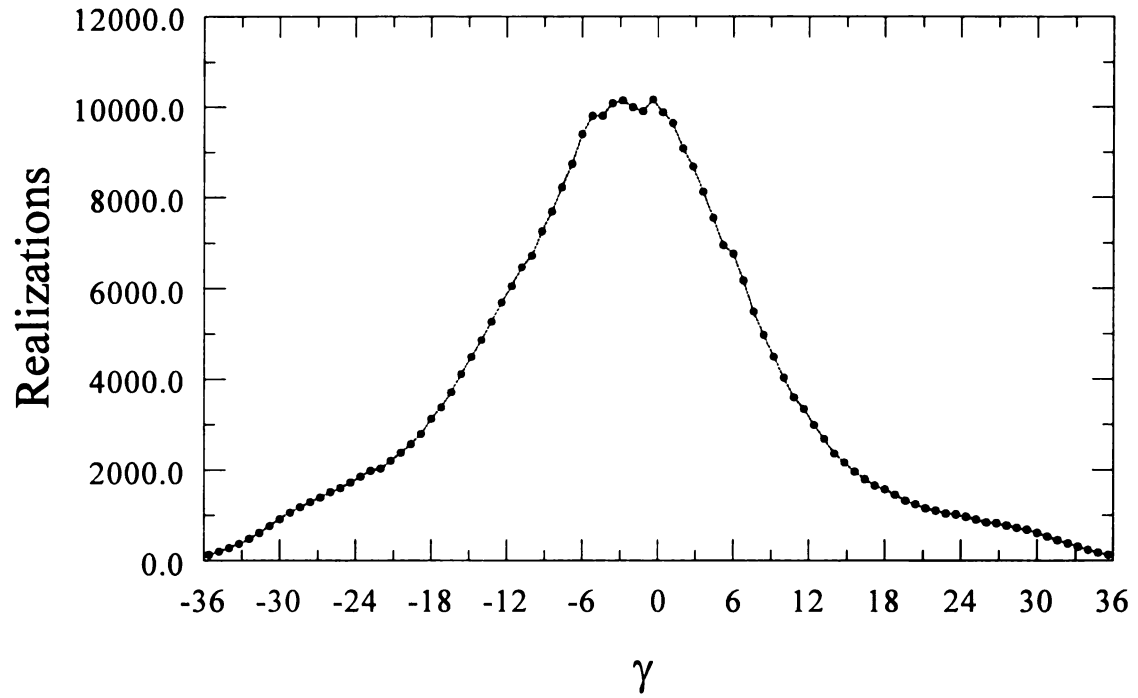
Figure 4.11 Histogram of flow angles for a properly aligned probe
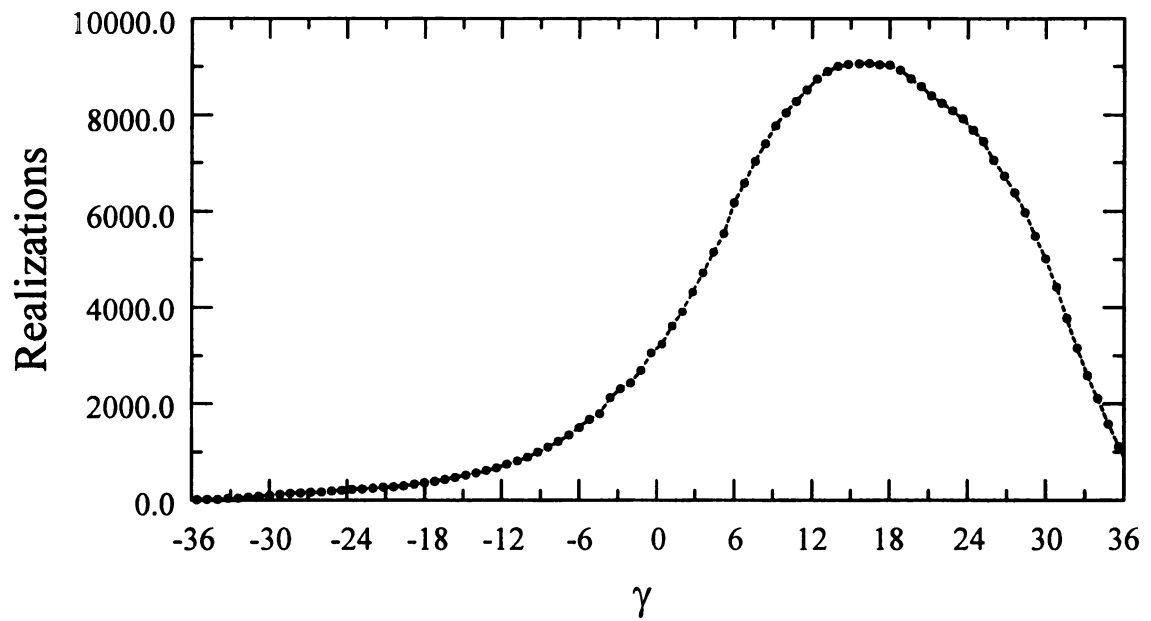
Figure 4.12 Histogram of flow angles for an improperly aligned probe
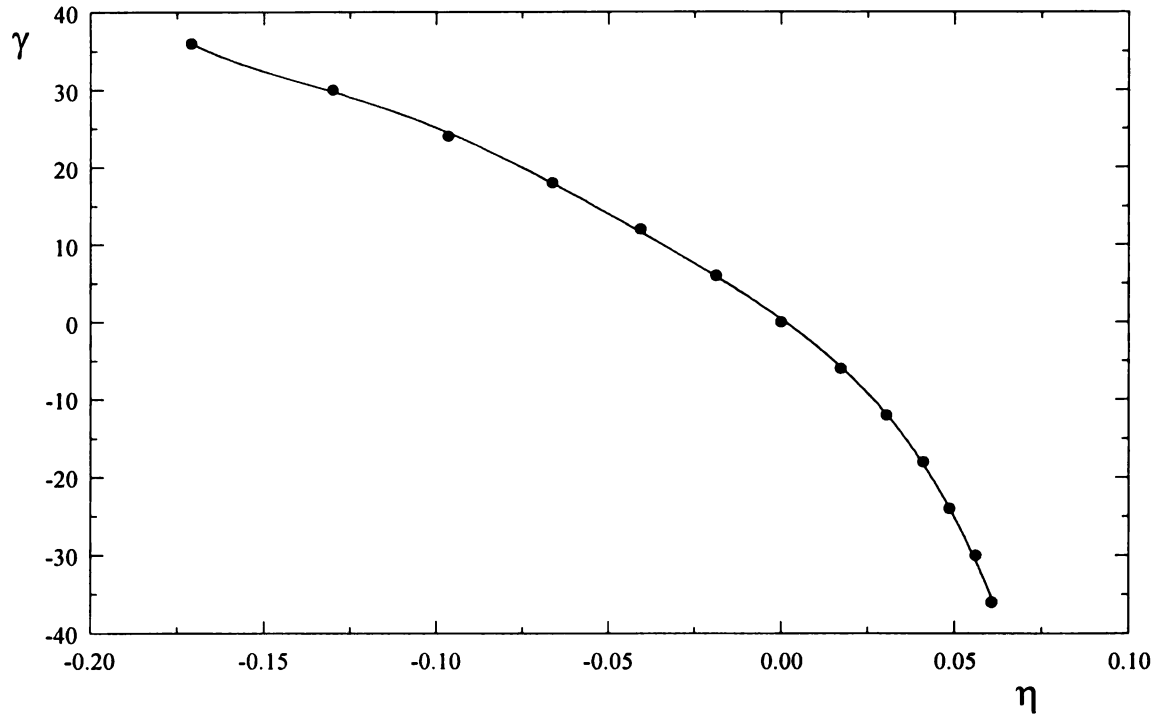
Figure 4.13 η versus γ with 5th order polynomial curve fit
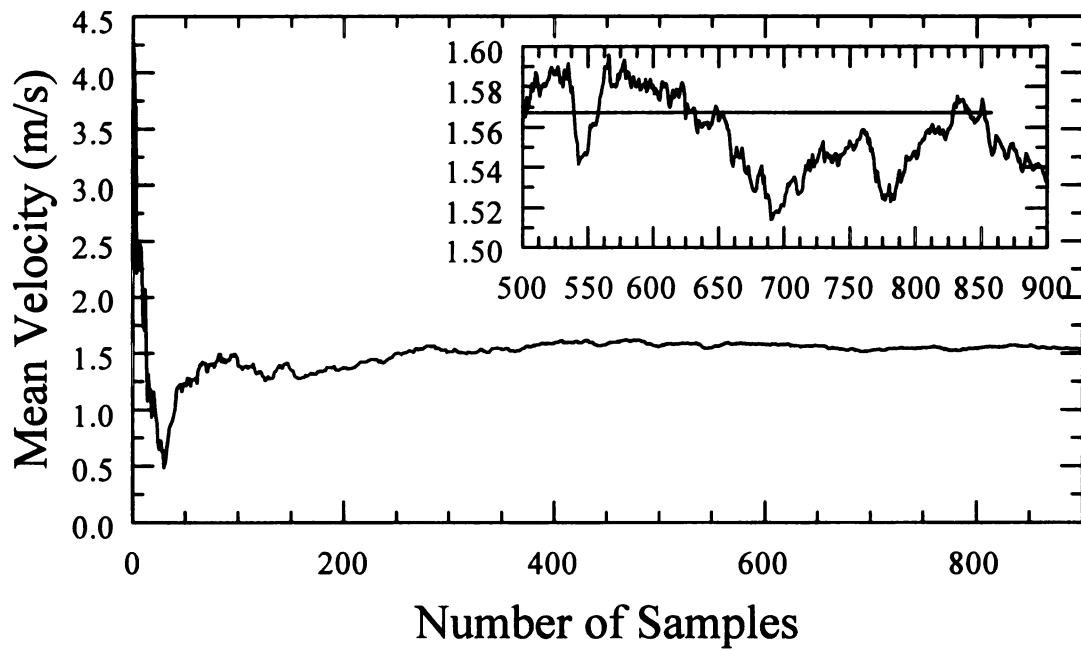
Figure 4.14 Example of statistical convergence of phase averaged data

5. RESULTS AND DISCUSSION – INTEGRAL PARAMETERS

The efficacy of the aerodynamic shroud concept has been demonstrated using performance and efficiency data for the fan and shroud system. This chapter will present and discuss these integral performance characteristics. A description of the dimensional conditions tested are given in Section 5.1. System performance and efficiency will be discussed in Sections 5.2 and 5.3 respectively. Experiments were also executed using the test fan with a small tip clearance boundary condition for comparison with the aerodynamic shroud results; these data are presented in Section 5.4.

5.1 Experimental Program

The system performance was established as the pressure rise across the fan as a function of the flow rate through the fan (i.e. $Q_{fan} = Q_{total} - Q_{shr}$.) Typically 15 points were acquired from $0 < \Delta P_{fan} < \Delta P_{fan\text{-}max}$ to define this "characteristic curve." These data were acquired for fan speeds of 800, 1000, 1200, 1400, 1600, and 1800 rpm with the shroud gap (g) set to 2mm. Data were also taken for g = 1.0, 1.5, 2.0, 2.5, and 3.0 mm with a fan speed of 1000 rpm. For each of the above tests typically 5 shroud pressure conditions were tested; these ranged from 0 to 800 Pa. This combination of variables led to a total of 50 curves to fully characterize the shroud and fan performance. The above dimensional conditions can be described in non-dimensional form as $0.000 < \chi < 0.068$ where χ is defined in equation (2-9).

5.2 Performance Data

The system performance is defined in terms of dimensionless variables by equation (2-7). An empirically based simplification of (2.7) has been identified by the process of examining correlations of the data. Specifically

$$\psi = \psi\left(\phi, \chi\right) \tag{5-1}$$

provides a two parameter representation of the pressure rise data for the present system. This equation implies that the pressure created by the fan/shroud combination is only a function of the flow rate through the fan, and the energy delivered to the shroud. This simplification of equation (2-7) can not be argued to be a necessary result of the

48

boundary value problem. However, the analysis and presentation of the experimental data have been greatly simplified by the reduced (3→2) number of independent variables.

The system performance for several χ values is shown in Figure 5-1. This "characteristic curve" type of data presentation is common in fan studies. Note that χ is not a unique function of ψ and ϕ as seen by the crossing of the curves in Figure 5-1 at lower flow rates. Therefore a clearer and more descriptive method of data representation is a contour plot of ψ on a ϕ versus χ plane allowing the functional dependence of equation (5-1) to be clearly shown; see Figure 5-2. Note that all the dimensional conditions listed in Section 5.1 were used in this figure.

The data show increased performance for higher flow rates, and decreased performance for lower flow rates in terms of the pressure rise at a given flow rate. As seen in Figure 5-1, the data for each χ value tested "crosses" the $\chi=0$ curve. For $\phi<\phi_{cross}$, the pressure rise at a given flow rate is decreased for $\chi>0$ when compared to $\psi(\chi=0)$. However, the pressure rise is increased for $\phi>\phi_{cross}$. For $\chi=0.0010$, this crossing occurs at $\phi_{cross}=0.17$. As χ is increased, the value of ϕ_{cross} decreases to 0.10 for $\chi=0.068$. Figure 5.2 shows a line representing the locus of points representing the ϕ_{cross} for all χ values.

At the higher flow rates ($\phi>\phi_{cross}$) the pressure rise increased monotonically with increasing χ. Also, the flow rate at zero pressure rise: $\phi_o=\phi(\psi=0,\chi)$ increased dramatically for $0<\chi<0.009$ from $\phi_o=0.27$ to 0.36. For $0.009<\chi<0.068$, ϕ_o increased more gradually according to the empirical function:

$$\phi_o = 0.900(\chi) + 0.346. \tag{5-2}$$

An additional collapse of the performance data was observed to define the function of equation (5-1). Specifically, for $\chi>0.009$, and $\phi/\phi_{max}>0.21$ the performance can be described by the function:

$$\psi = \left(1000\cdot\chi\right)^{0.2}\left(-0.1708\left(\tfrac{\phi}{\phi_o}\right)+0.0365\left(\tfrac{\phi}{\phi_o}\right)+0.1351\right) \tag{5-3}$$

This data fit along with performance data from several χ values are shown in Figure 5.3. Equations (5-2) and (5-3) can be used to estimate the pressure rise across the fan given the flow rate and χ value to within an estimated error of ±5%.

5.3 Efficiency Data

The efficiency of the cooling fan and aerodynamic shroud combination is defined in equation (2-5) and given in terms of its functional dependence in equation (2-8). Analysis of the data has shown that the system efficiency, like the performance, can be described by:

$$\eta_{sys} = \eta_{sys}(\phi, \chi). \qquad (5\text{-}4)$$

Figure 5.4 shows the efficiency for the same χ values shown in Figure 5.1. Similar to the performance data, the efficiency data can also be presented as a contour plot to uniquely describe its functional dependence; see Figure 5.5. The data presented in Figures 5.4 and 5.5. were calculated using η_{shr}=1.0. Figures 5.6 and 5.7 are representations of the efficiency data using η_{shr}=0.7. Comparison of Figures 5.4 and 5.6 indicate that a less efficient shroud delivery system would cause some decrease in overall efficiency, however, the qualitative characteristics of the data remain the same.

The data shown on Figure 5.4 show that the aerodynamic shroud increases efficiency for high flow rates, and decreases efficiency for lower flow rates. The amount of increase or decrease is extremely sensitive to the shroud energy for $0<\chi<0.020$, and less sensitive to this variable for $0.020<\chi<0.068$. It is interesting to note that the flow rate at which the efficiency curves for $\chi>0$ crosses that of $\chi=0$ is approximately $\phi=0.17$ for all χ values.

5.4 Small Tip Clearance Study

The data presented in Sections 5.2 and 5.3 compare the performance of the fan and shroud combination to the shroud off condition (i.e. $\chi=0.000$). A single experiment was conducted to compare the performance and efficiency of the aerodynamic shroud with a 2.5cm tip clearance to a shroud with near zero tip clearance. A ring made from Styrofoam was manufactured to fill the annular area between the fan tip and aerodynamic shroud. The inner diameter was build slightly undersized, and then "reamed" by the rotating fan to create a small ($\approx$1.0mm) tip clearance.

Figure 5.8 and Figure 5.9 show the performance and efficiency respectively for the small tip clearance along with data presented in Section 5.2 and 5.3. The results show

that both performance and efficiency are enhanced at higher flow rates, and degraded for lower flow rates. These data indicate that fan applications where a small tip clearance is allowed could benefit from a larger tip clearance with the aerodynamic shroud. Applications which operate in an environment which has a relatively small system resistance would be the most likely to benefit, i.e., high flow rate--low pressure rise conditions. It should be understood however, that the fan used in this test was not designed to operate with a small tip clearance. Additional research will be able to determine if the general trends observed in these data would apply to other fan designs.
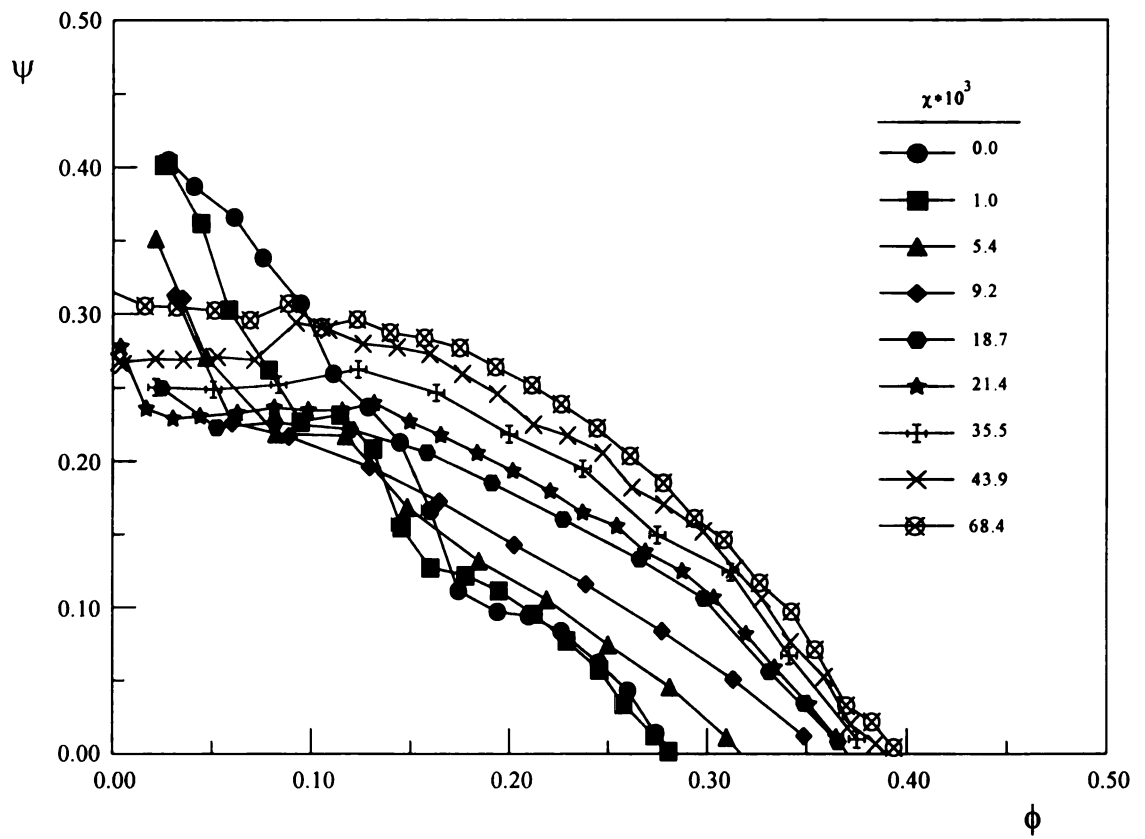
Figure 5.1 Pressure rise vs. flow rate data for selected shroud conditions
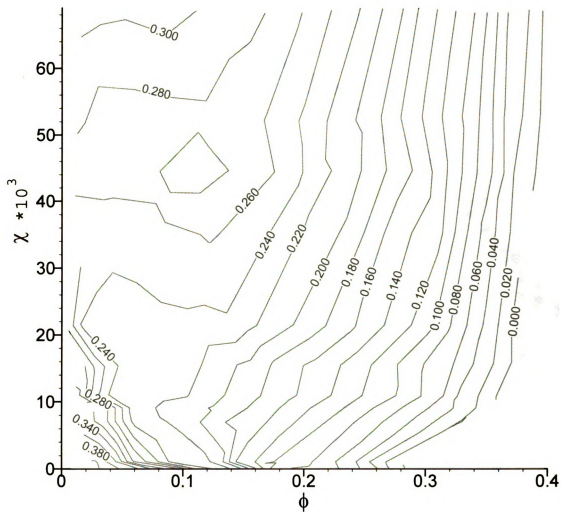
Figure 5.2 Contour plot of system performance (ψ)
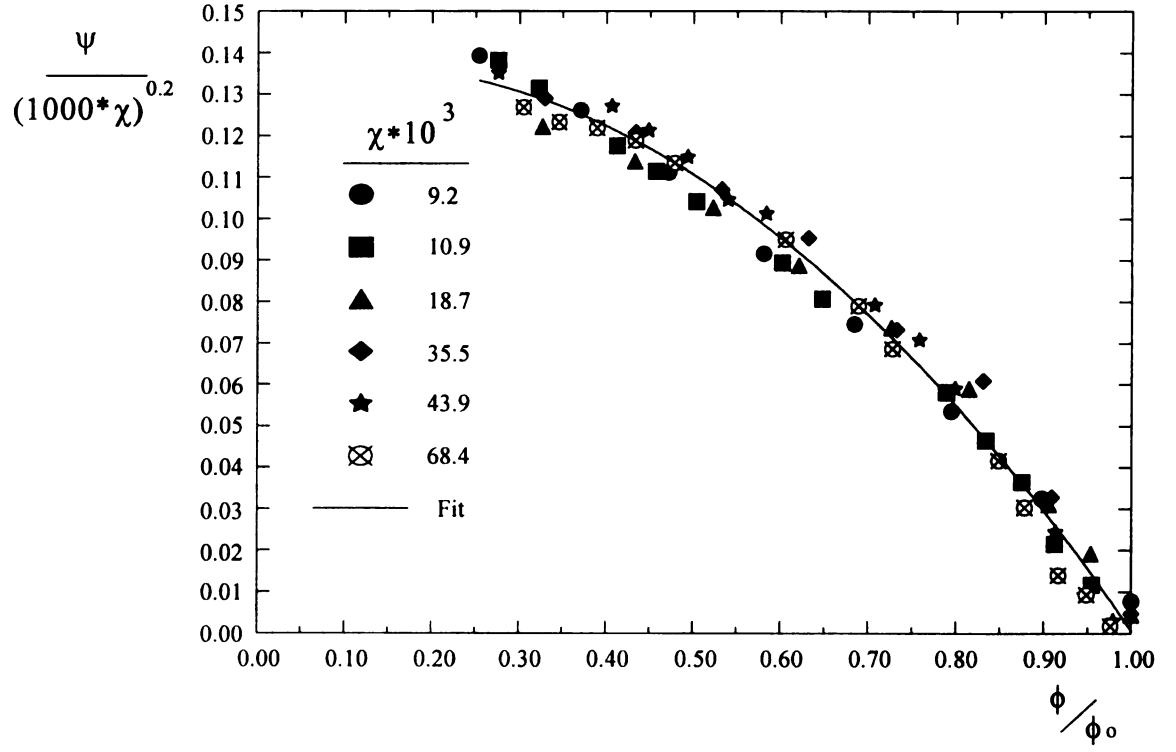
Figure 5.3 Data fit for $\chi > 0.009$
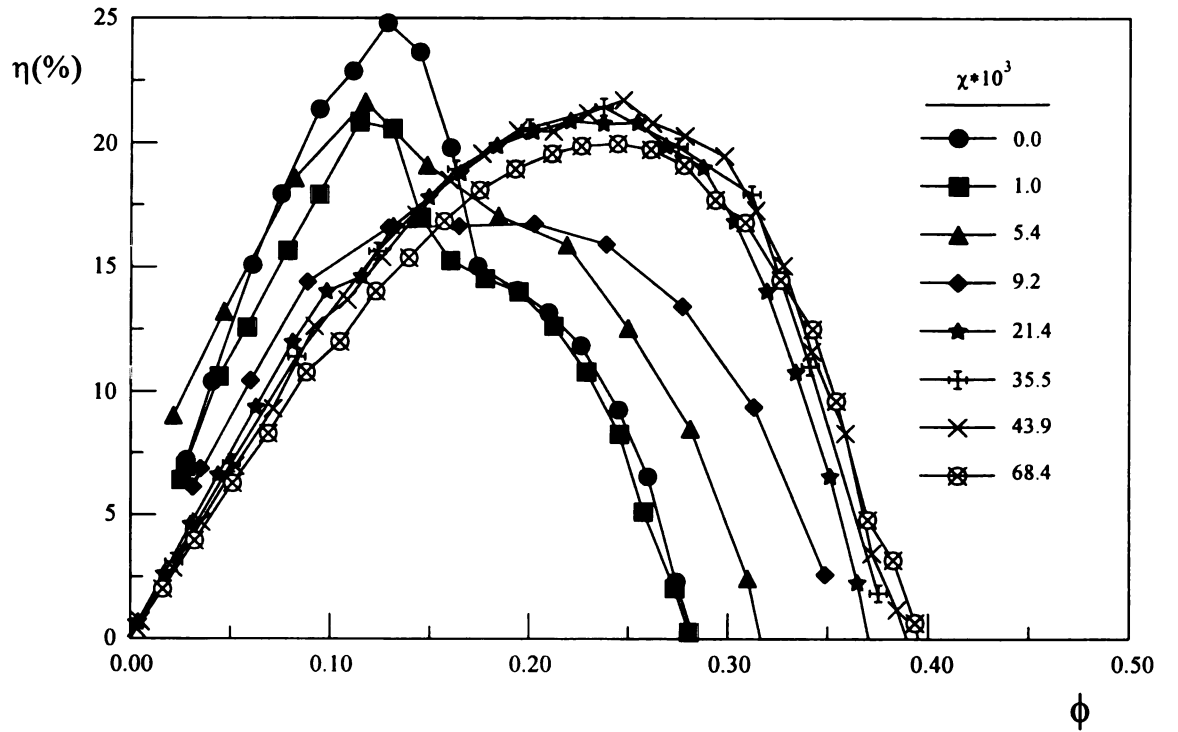
Figure 5.4 Efficiency data for selected χ values ($\eta_{shr}=1.0$)
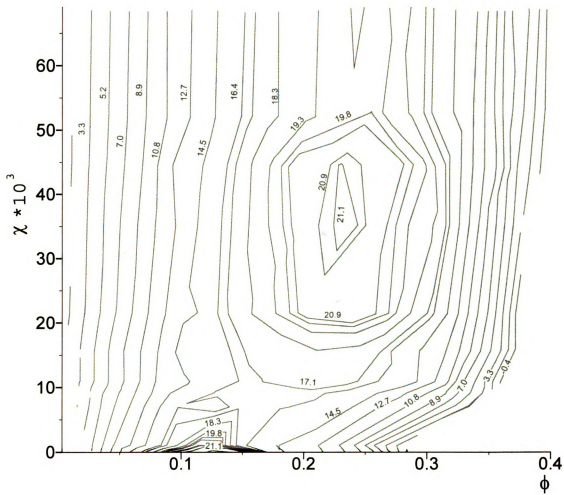
Figure 5.5 Contour plot of fan/shroud efficiency (η_{shr}=1.0)
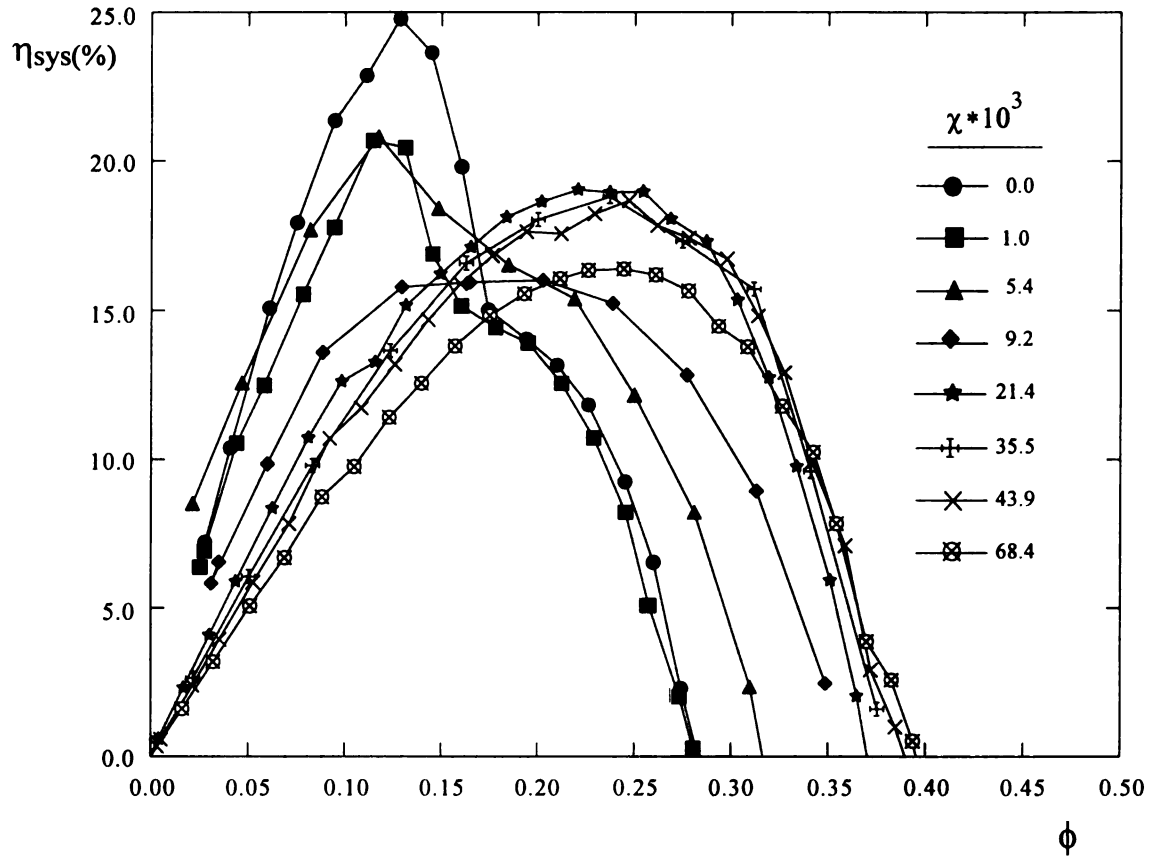
Figure 5.6 Efficiency data for $\eta_{shr}=0.70$
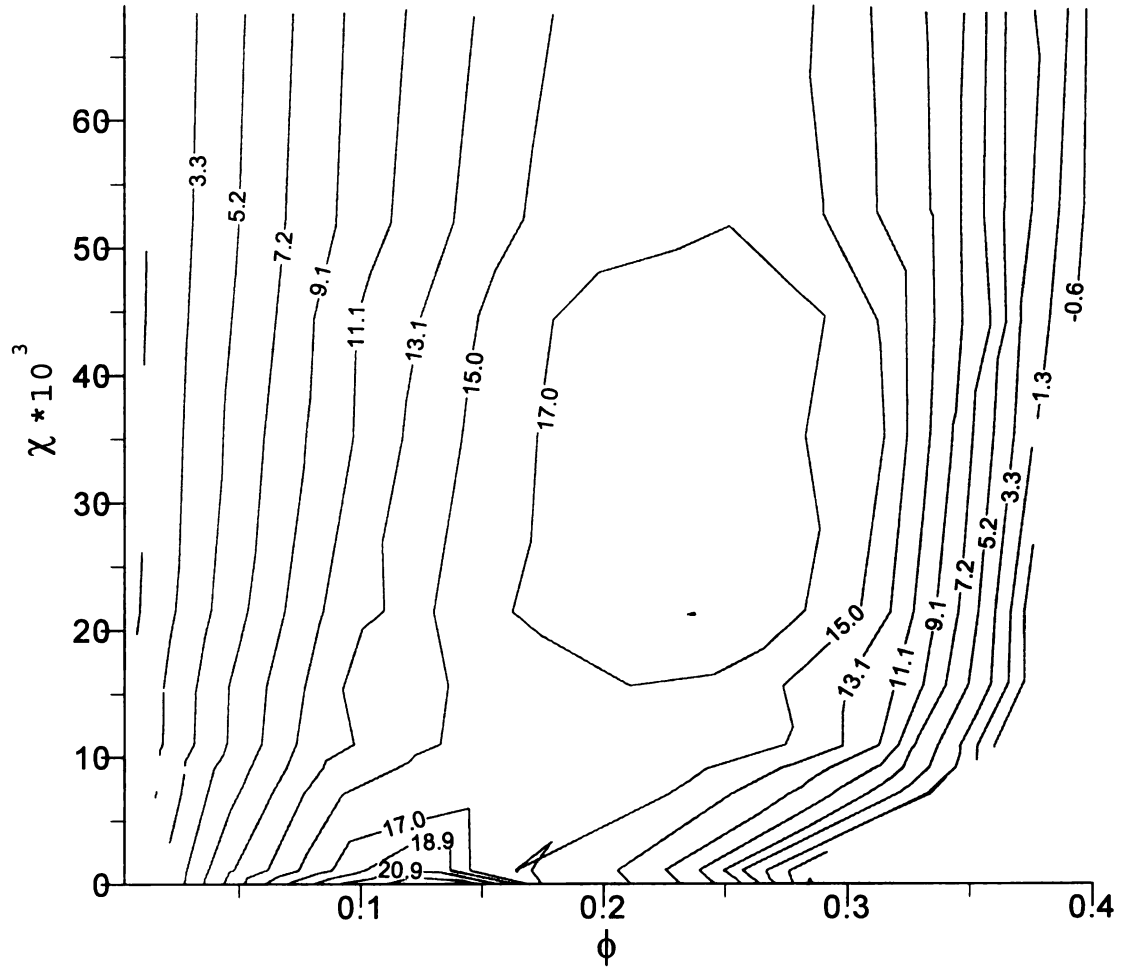
Figure 5.7 Contour plot of fan/shroud efficiency (η_{shr}=0.70)
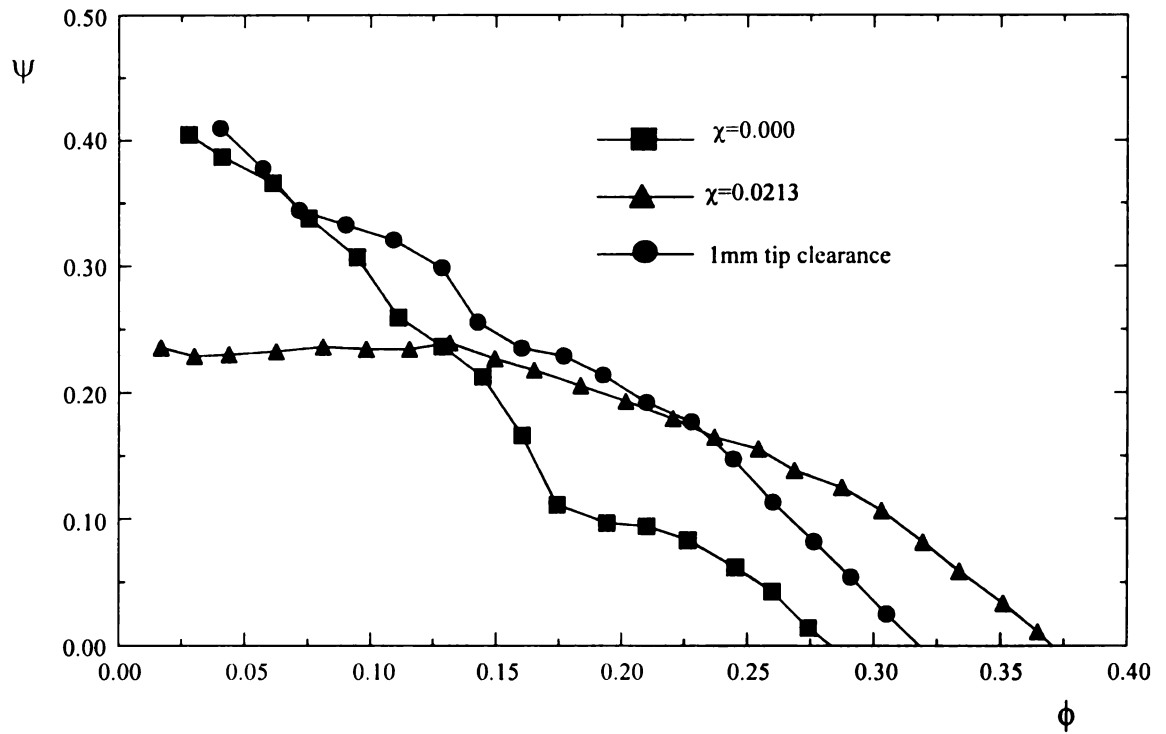
Figure 5.8 Performance curve for fan with 1.0 mm tip clearance
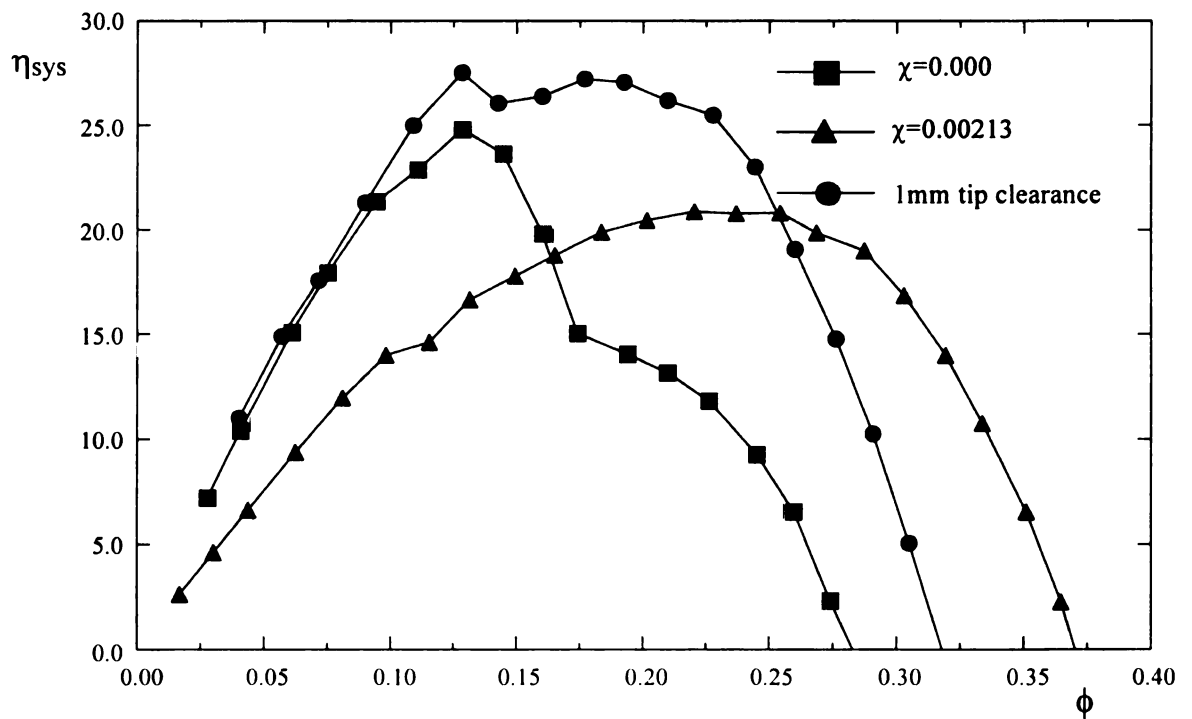
Figure 5.9 Efficiency curve for fan with 1.0mm tip clearance

6. RESULTS AND DISCUSSION – VELOCITY MEASUREMENTS

Tufts and hot-wire anemometry were used to quantify the velocity field in the wake of the fan. A single fan speed of 1000 rpm was chosen for the detailed experiments. It was assumed that different fan speeds would not significantly affect these results given the collapse of the dimensionless variables shown in Chapter 5.

The tufts were used to gain a qualitative understanding of the flow field in addition to the measurement of the time mean flow angle for use in hot-wire positioning. Tuft surveys were conducted for a wide range of operating conditions. The dimensionless parameters as well as an identification letter for these conditions are listed in Table 6-1. These conditions are represented graphically with the performance data presented in Chapter 5 on Figure 6.1.

Hot-wire surveys were conducted for conditions 'G' through 'K'. For purposes of comparison, it was decided that three points of constant ϕ with χ = 0.000 , 0.020, 0.068 would be investigated (points 'G', 'H', and 'I'.) Additionally, three points of constant ψ with χ = 0.000 , 0.020, 0.068 (points 'I', 'J', and 'K') would be examined. This would allow the details of the flow field to be compared as the shroud power is increased for constant flow rate and for constant pressure respectively.

6.1 Tuft Results

Tuft surveys were conducted for the conditions listed in Table 6-1. Ten radial locations (0.5<r/R<1.0, Δr/R=0.056) were interrogated at a single axial distance (x/R=0.11) as well as several axial locations (-0.05<x/R<+0.1, Δx/R=0.056) at a constant radius (r/R=1.17). The flow was assumed to be axisymmetric; therefore a single arbitrary

θ position was used for the traverse. These locations are shown with a schematic of the fan and shroud in Figure 6-2a. Figure 6-2b shows a view of the x-θ plane with a vector representation of the outlet flow angle (β_2). Digital images in the x-r and r-θ planes were acquired for each tuft position. An example of a digital tuft picture in the x-r plane is shown in Figure 6-3.

Results from conditions 'A' through 'K' are shown in Figures 6-4 through 6-14 respectively. Each figure contains a partial schematic of the fan and shroud, as well as a vector representation of the mean flow angle measured from the tuft as shown by vector arrows. The arrows which originate at an "X" show the angle of the vector in the x-r plane. An arrow representing the x-θ view of the same location is drawn directly below its x-r plane representation, and originates from a "+" sign; note that this view is presented only for the locations of constant x/R.. A vertical line is shown at each vector origin for reference. The symbol $\otimes$ represents a location where the tuft was extremely unsteady and a single mean flow direction was not observed.

Conditions 'C', 'F' and 'I' represent the data taken with the aerodynamic shroud "off", i.e., χ= 0.000. Condition 'I', which is a relatively high flow rate condition is characterized by nearly uniform outlet flow angle (β_2) and low radial velocities. A large region of reversed flow is noted in the tip clearance area. As the flow rate is decreased (pressure is increased) the flow near the hub separates from the suction side of the fan blades as indicated by the reversed flow directions shown near the hub in condition 'F'. This condition is referred to as "fan stall" in Baranski (1977). Past researchers (Dring et. al (1982)) have observed reversed axial flow and strongly radial flow corresponding to suction side boundary layer separation as indicated by flow visualizations. As this

separation occurs, the flow near the tip becomes predominantly radial. As the flow is further decreased, condition 'C' shows reversed flow over the entire blade span, and outwardly radial flow in the tip clearance area.

Conditions 'A' and 'B' represent the flow field as χ is increased while the flow rate is held constant from condition 'C'. Note that the aerodynamic shroud decreases both performance and efficiency at this flow rate. The results show relatively little change in the tuft directions. The entire blade span remains stalled and the radial flow in the tip clearance area appears unaffected by the aerodynamic shroud. Similarly, conditions 'D' and 'E' represent the flow field as χ is increased for the same flow rate as condition 'F'. These data also indicate that the flow directions are somewhat insensitive to the aerodynamic shroud. It is believed that the reduced performance of the fan/shroud system at these operating conditions is a result of the radial outflow at the fan's tip. Specifically, the tip clearance flow is the only positive net flow through the blades, and is therefore the only contributor to the net pressure rise across the fan. The aerodynamic shroud was designed to maintain axial flow throughout the tip clearance area, and therefore it reduces the effectiveness of the fan to produce the radial outflow.

It is interesting to note that axial flow turbomachinery typically shows low pressure rise at the lower flow rates as a result of fan stall. A peak in performance is then observed. Automotive cooling fans do not exhibit this behavior because of the partially shrouded boundary condition that allows the fan to create the radial outflow and thereby maintaining a relatively high pressure rise at low flow rates. The aerodynamic shroud which "fills" the tip clearance gap with a Coanda jet of air seems to cause the fan to behave as if it had a cylindrical boundary condition. This characteristic peak in

performance at the middle flow rates is slightly visible in Figures 5.1 and 5.2 for 0.030<χ<0.050.

Conditions 'G', 'H', and 'I' were taken at a flow rate where the performance and efficiency were enhanced by the aerodynamic shroud. The flow field directions in the wake of the blades were relatively unaffected by the shroud jet. However the tip clearance flow in this area was reversed. Specifically, the negative axial flow in the tip region observed for condition 'I' was reversed by the presence of the Coanda jet. This behavior was also observed as χ was increased at constant fan pressure (i.e., conditions 'I', 'J', and 'K'). Additional observations show that the mean flow direction in the entire clearance area:

$$A_{cl} = \frac{\pi}{4}\left(D_{shr}^2 - D_{fan}^2\right)$$

(6-1)

is in the negative axial direction for condition 'I'. The relatively large ratio of A_{cl}/A_{flow} = 0.31 indicates that a negative axial velocity through the tip clearance area would have a large effect on the net volume flow rate. Specifically, given a uniform velocity distribution, 31% of the flow through the blades would be recirculated in the tip clearance and would not contribute to the net Q_{fan}. The ability of the shroud to enhance the performance of the fan for these flow conditions is believed to be a result of the positive mean axial flow momentum cause by the shroud in the tip clearance region.

6.2 Hot-wire Results

Hot-wire surveys were conducted for conditions 'G', 'H', 'I', 'J', and 'K' listed in Table 6-1. The hot-wire locations surveyed for these test conditions were 0.5<r/R<1.1, Δr/R=0.55, with x/R=0.11. The flow was assumed to be axisymmetric. Time series

voltages were acquired from the two hot-wires as well as the optical encoder attached to the drive shaft. Data were taken as 6000hz, corresponding to a single measurement for every 1 degree of fan rotation (given a fan speed of 1000 rpm). Time averaged mean and RMS of velocity are reported in section 6.2.1. Data collected from all radial locations were organized to be presented on a grid as shown in Figure 6.15. Note that data were acquired for the full 360 degrees of revolution. Only the first 90 degrees of rotation will be presented. Phase averaged mean and RMS of velocity, as well as vorticity, will be reported in this chapter. Two additional quantities: the phase averaged kinetic energy and exit flow angle are reported in Appendices B and C respectively.

6.2.1 Time Averaged Velocity Results

Time averaged mean and RMS of velocity were calculated at a function of radius from equation (4-23) and (4-24). Axial, Tangential, and Radial mean and RMS velocities are shown in Figures 6.16 through 6.18 using U_o to normalize the data. Figures 6.19 through 6.21 show the same data scaled by U_{tip}. Note that U_o can be recomputed from equation (2-1), given the blade tip speed U_{tip}=23.94m/s at 1000 rpm. The magnitudes of the time averaged velocities were not greatly affected by the aerodynamic shroud. However, qualitative changes in the profiles were observed. For example, Figure 6.19b indicates that conditions 'J' and 'K' have considerably lower RMS levels for 0.65<r/R<0.9. Also, condition 'G' showed greater mean radial velocities for r/R>0.8 compared to conditions 'H' and 'I', whose mean radial velocities were nearly identical; see Figure 6.21a. The stalling phenomenon clearly visible at the lower flow rates from the tuft observations appears to be present in condition 'G' as seen be the negative axial velocities near the hub. Dring (1982) also noted large radial velocities in axial

turbomachinery when a "corner stall" was present. Additional discussion of these velocity data will be given in the following section where in the phase averaged representation of the results is presented.

6.2.2 Phase Averaged Velocity Results

Phase averaged data were calculated from the time series using equations given in Chapter 4. These data are presented as contour plots for the first 90 degrees of rotation. The orthogonal axis indicate the radial position normalized by blade radius $(R=D_{fan}/2)$. Tick marks are shown at 15 degree increments. Iso-velocity contours are shown and given a label number in the figures. A legend is shown which relates the contour number to the velocity scaled by U_o and U_{tip}.

Mean axial velocity results for conditions 'G' through 'K' are shown on Figures 6.22 through 6.26 respectively. The data show a periodic signal every 36 degrees indicating the passing of the fan blades. A radial line of local minimum axial velocity is observed, and believed to have been caused by the wake of the fan blades. This is most clearly seen for conditions 'J' and 'K'. For reference, tick marks with a (*) have been placed at 6.4, 42.4, and 78.4 degrees to indicate the center of the blade wake. These values were selected from local minimums in axial velocity observed for condition 'I'. The qualitative aspects of the axial flow field between the blades are similar for all five test conditions. Specifically, a local maximum is observed for all conditions near $r/R=0.8$. The azimuthal position of the maximum did however vary for the different conditions. It is interesting to note that the magnitudes of U_x/U_{tip} were relatively unaffected by the increase in flow rate from 'I' to 'K'. It is therefore believed, as discussed in Section 6.1, that the increase in flow rate is a result of the positive net flow in the tip clearance area;

i.e., less flow is recirculated in the tip thereby increasing the net positive flow rate. As a result the relative values of U_x/U_o decreased for conditions 'J' and 'K'.

Tangential mean velocities are shown in Figures 6.27 through 6.31. These show the sharp gradients in velocity near the hub and tip areas showing the shearing of the flow exiting the fan with the non-rotating fluid in the upper receiver. These results show considerable variation in the qualitative character of the flow field between the different flow conditions. The magnitudes of U_θ/U_{tip} are, however, relatively insensitive to the flow condition.

Radial mean velocities are shown in Figures 6.32 through 6.36. Large positive radial velocities are observed for a range of α values slightly greater than that of the blade wake (this can be interpreted as the "suction surface" region) for all test conditions. Also, negative radial velocities are observed at values of α less than that of the blade wake (i.e., the "pressure surface"). This region of negative radial velocity is considerably larger for conditions 'J' and 'K'. There are several theories in the literature which attempt to explain this pattern of radial velocities. Several researchers (Inoune and Kuroumaru (1984), Dring et.al (1982)) have observed strong positive radial velocities near the suction side of the blades. This has been attributed to centrifugal effects acting on the blade's boundary layer. It was also noted that a corner stall at the hub will significantly increase the positive radial velocities. Note that condition 'G', which appears to exhibit corner stall as indicated by the small positive and negative axial velocities, shows the largest positive radial components. Lakshminarayana (1996) provides a different reasoning for these "secondary flow features" which is also compatible with the presented data. Specifically, the streamlines seen by an observer rotating with the blades are curved

corresponding to the pressure gradient created by the suction sides and the pressure sides of the blades. The boundary layer on the fan hub can not support this pressure gradient, and therefore a secondary flow exists. This phenomenon is identical to the secondary flow which is observed in a stirred tea cub which causes the collection of particles at the center of the bottom of the cup.

The phase averaged RMS results for the three velocity components are shown on Figures 6.37 through 6.51. Note that these results indicate the "unsteadiness" of the flow field and are not necessarily indicative of sheared or turbulent fluid. Large cycle to cycle variations have been observed in the time series, and are suspected to be a result of small disturbances in the laboratory air. These can cause the RMS calculation to show relatively high values of unsteadiness in fluid that has not been sheared by the fan. It is difficult (if not impossible) to separate cycle to cycle variations from turbulence caused by the shearing of the fluid by the fan blades.

The RMS data reported show high disturbance levels near the blade wake region, as well as the hub and tip regions. The area interior to the blades shows relatively low RMS levels. This central region of low RMS intensity is clearly seen for condition 'K'. Figure 6.1 of Lakshminarayana (1996) is a similar picture showing shaded regions of high unsteadiness. The shape of the "inviscid core region" in this reference is very similar to contour number 6 shown on Figure 6.41. As the flow rate is decreased ('J' and 'I') this region becomes smaller indicating that the boundary layer thickness on the surface of the blades is increasing. As χ is increased at constant flow rate ('H' and 'G') this region becomes even smaller indicating that the increased pressure rise across the fan caused by the aerodynamic shroud has caused the boundary layer thickness to further increase.

6.2.3 Phase Averaged Vorticity Results

Axial vorticity was calculated from equation (4-29) and normalized by $2\Omega_{fan}$. These results are shown in Figures 6.52 through 6.56. A large region of negative vorticity is observed in the wake of the blades. This is a result of the positive radial velocity on the suction surface and the negative radial velocity on the pressure surface which interact downstream of the blades. A weak region of negative vorticity is also realized for all test conditions near the hub as would be expected from the shearing of the rotating fluid through the fan with the fluid in the wake of the hub. A large region of strong positive vorticity is observed for all conditions in the tip clearance area. This is also expected based on the above comments for the hub flow. Relatively low magnitudes of ω_x were observed for conditions 'J' and 'K' for much of the region interior to the blade wakes. It is interesting to note that this region becomes smaller for conditions 'I', 'H', and 'G'. Note that the contour of near zero ω_x is similar in shape to the contours of low RMS values for all five test conditions, i.e. there is an obvious correlation between the areas of low disturbance level and low vorticity level.

Large regions of concentrated positive vorticity are observed for conditions 'J' and 'K' near the tip of the fan. This is also observed for conditions 'G', 'H', and 'I', however it is more difficult to see. Many previous researchers (see, e.g. Lakshminarayana (1970), Inoue (1986)) have measured similar behavior in axial fans. The literature often refers to this as the "tip clearance vortex". It is believed (Lakshminarayana (1996)) that this is caused by a "rolling up" of the vorticity caused by the tip leakage flow. Specifically, a vortex sheet is created by flow separation at the tip of the blades. There is a great deal of

literature which attempts to correlate tip clearance effects with the "losses" in the blade

row (Storer (1994), Lakshminarayana (1970), Adamczyk (1993)).

Table 1 Test conditions for detailed study

Test Condition	ψ	ϕ	χ
'A'	0.30	0.05	0.068
'B'	0.24	0.05	0.020
'C'	0.38	0.05	0.000
'D'	0.30	0.10	0.068
'E'	0.23	0.10	0.020
'F'	0.30	0.10	0.000
'G'	0.28	0.17	0.068
'H'	0.20	0.17	0.020
'I'	0.10	0.17	0.000
'J'	0.10	0.30	0.020
'K'	0.10	0.34	0.068
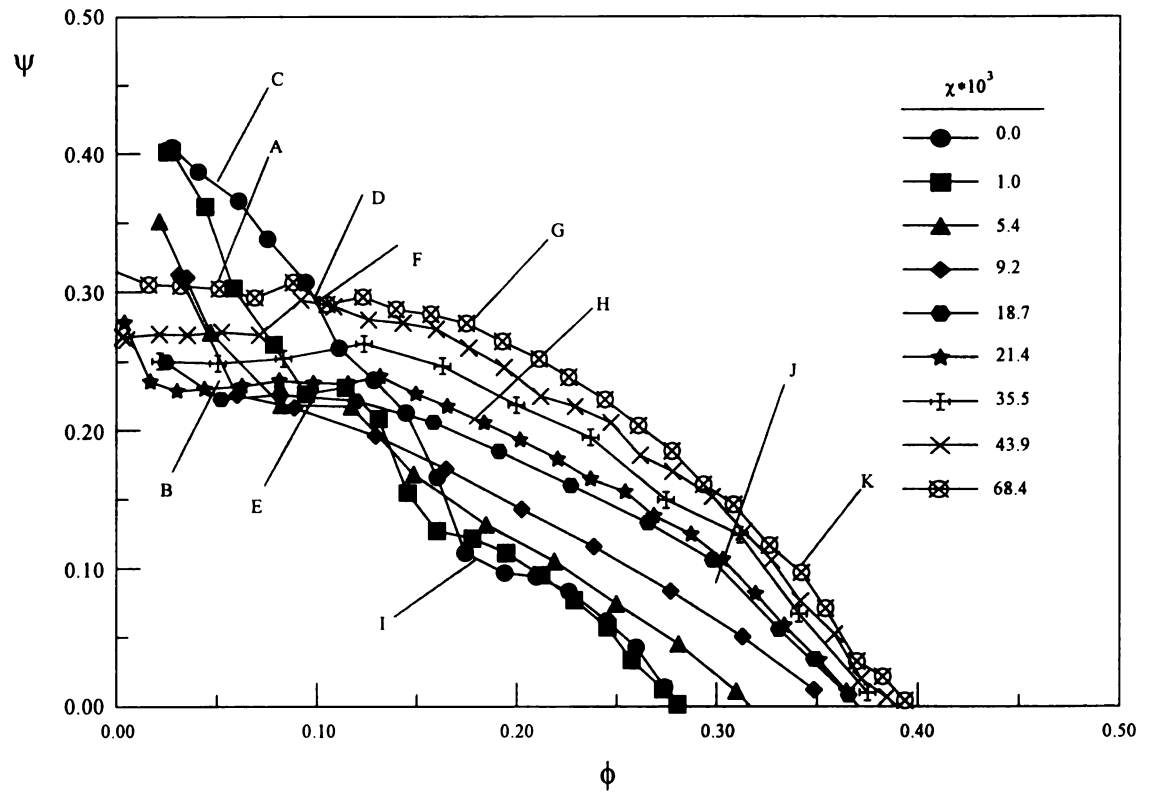
Figure 6.1 Performance data with test conditions for detailed study labeled
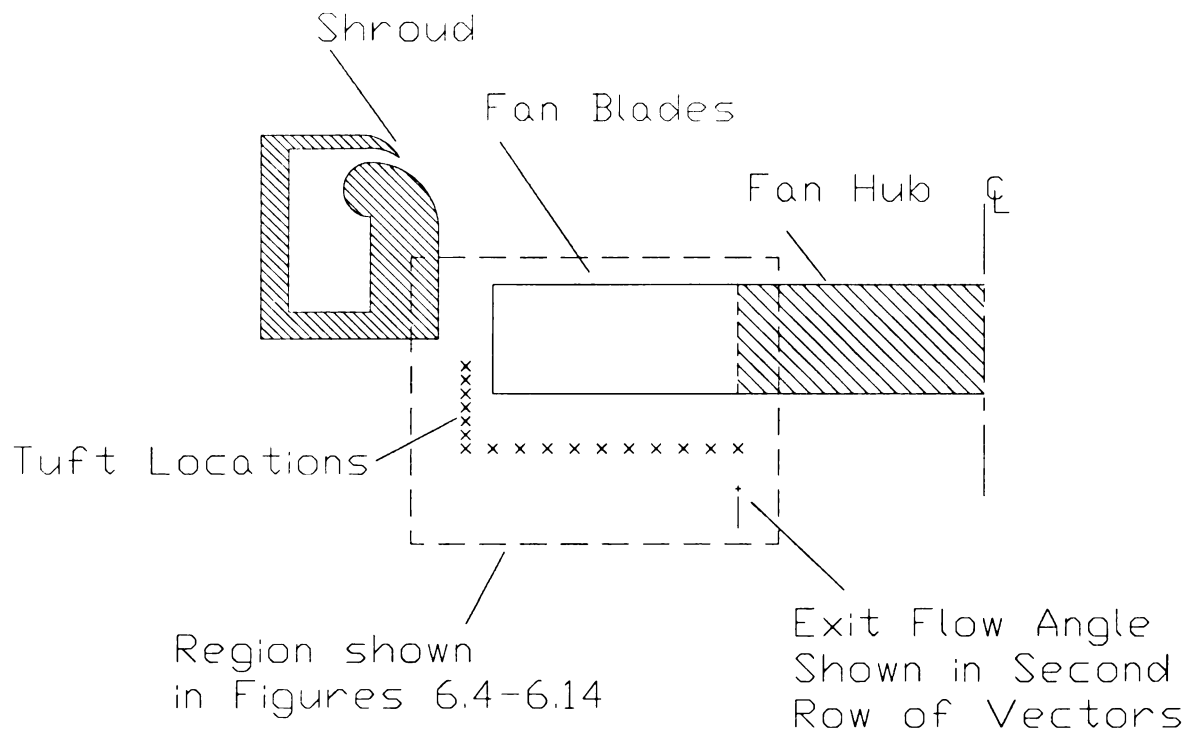
Note: Symbol ⊗ represents undetermined flow angle

Figure 6.2a Schematic of tuft survey locations
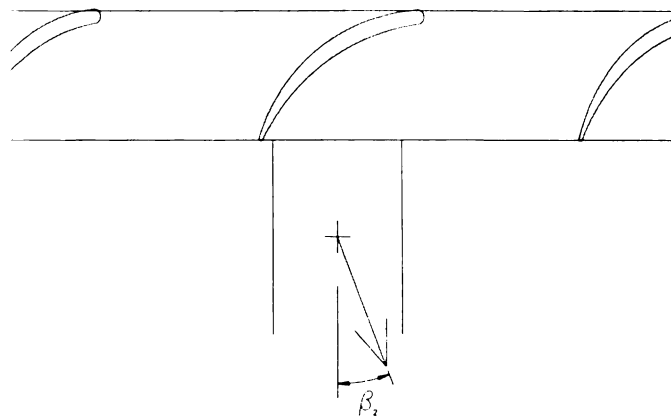
Figure 6.2b Representation of exit flow angle β_2.

Figure 6.3 Representative digital image of tuft
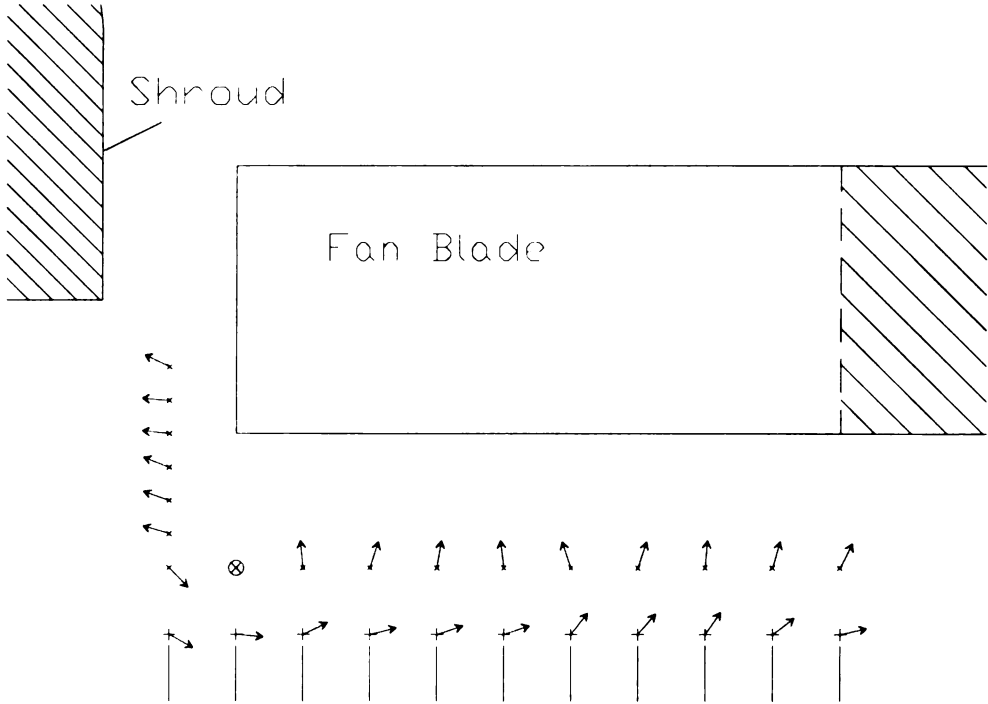
Figure 6.4 Tuft results from condition 'A'
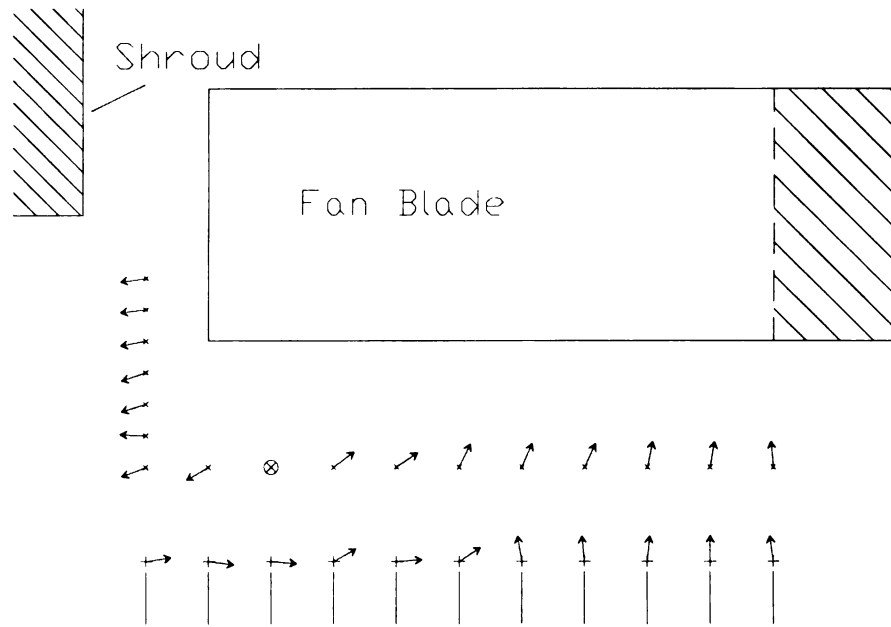
See Figure 6.1 for definition of symbols

Figure 6.5 Tuft results from condition 'B'
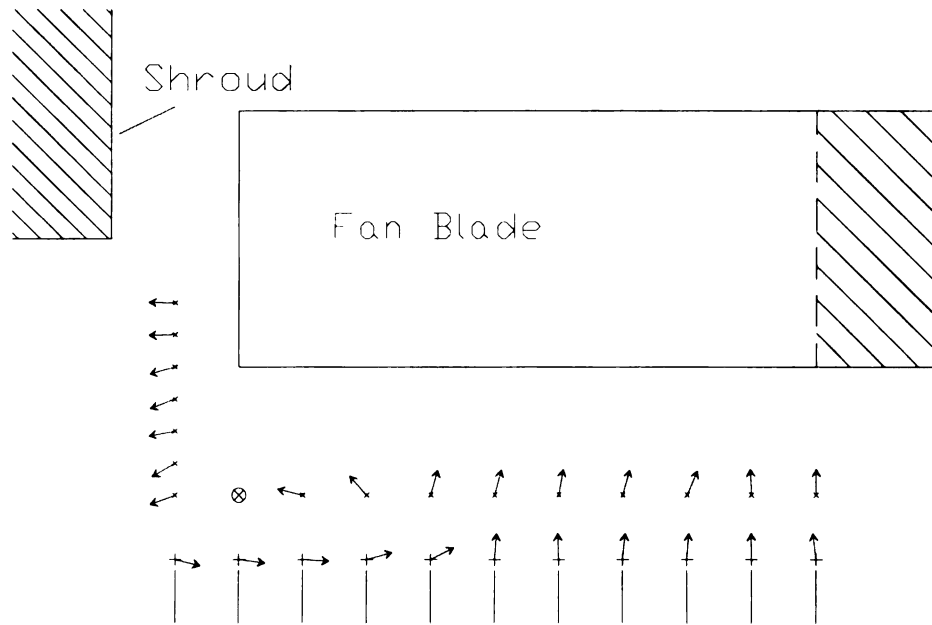
See Figure 6.1 for definition of symbols

Figure 6.6 Tuft results from condition 'C'
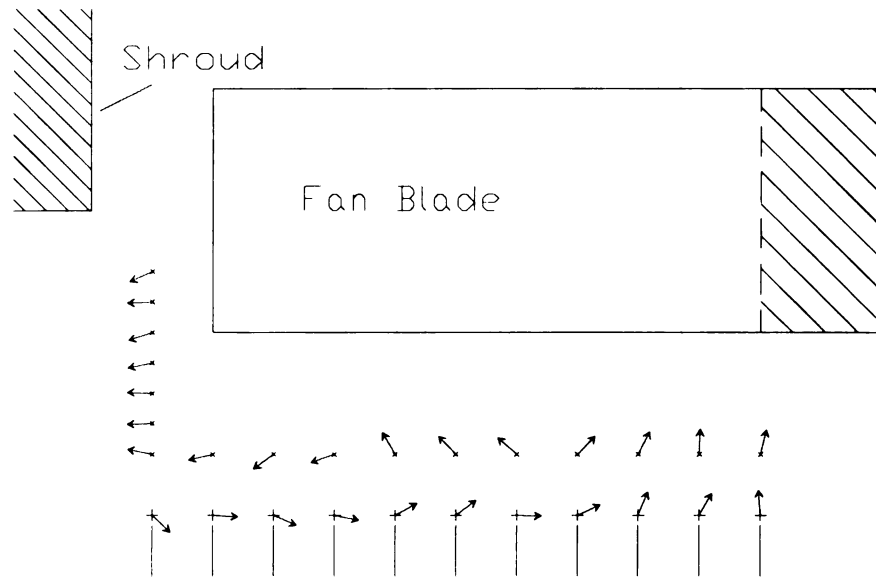
See Figure 6.1 for definition of symbols

Figure 6.7 Tuft results from condition 'D'
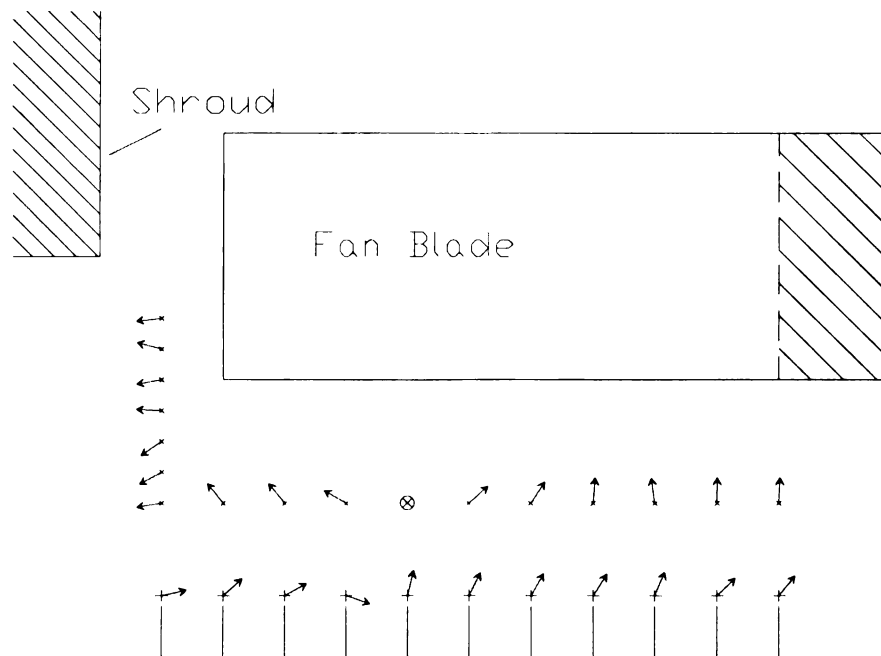
See Figure 6.1 for definition of symbols

Figure 6.8 Tuft results from condition 'E'

Shroud

Fan Blade
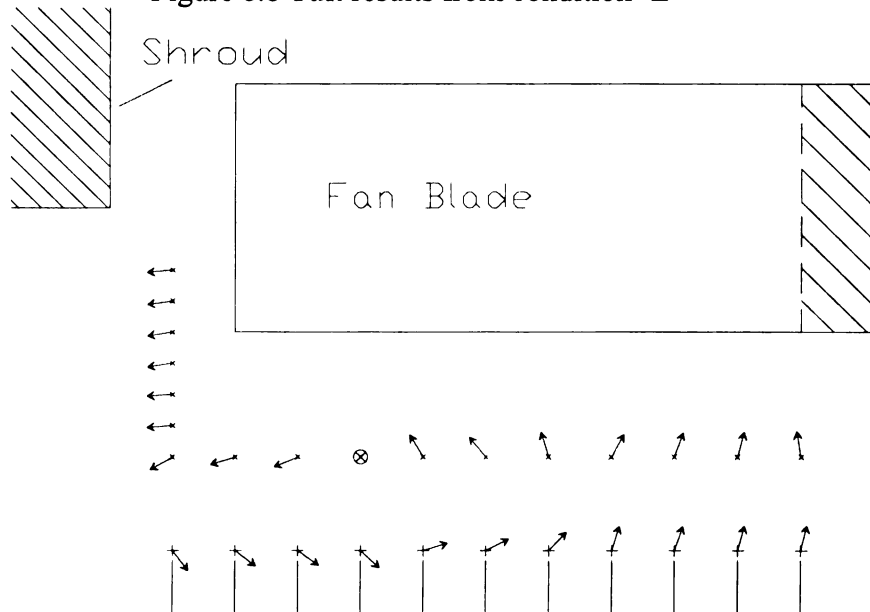
See Figure 6.1 for definition of symbols

Figure 6.9 Tuft results from condition 'F'
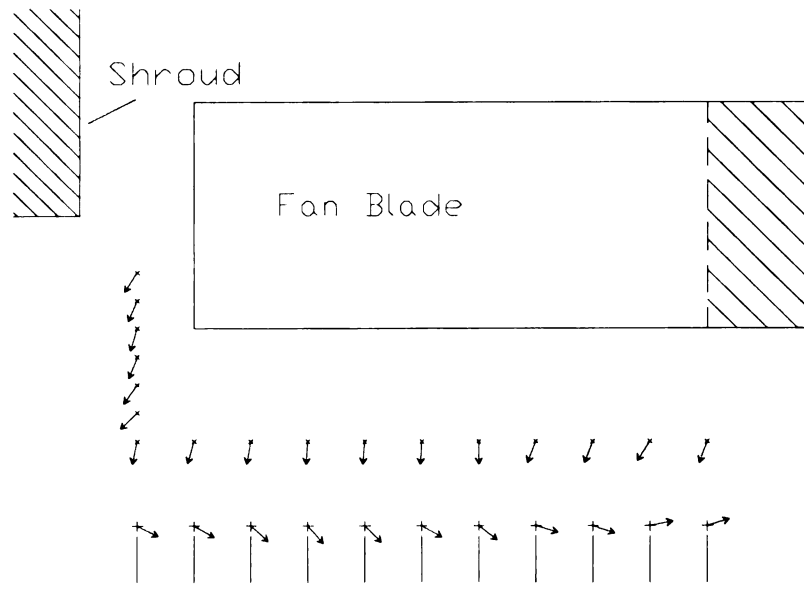
See Figure 6.1 for definition of symbols

Figure 6.10 Tuft results from condition 'G'
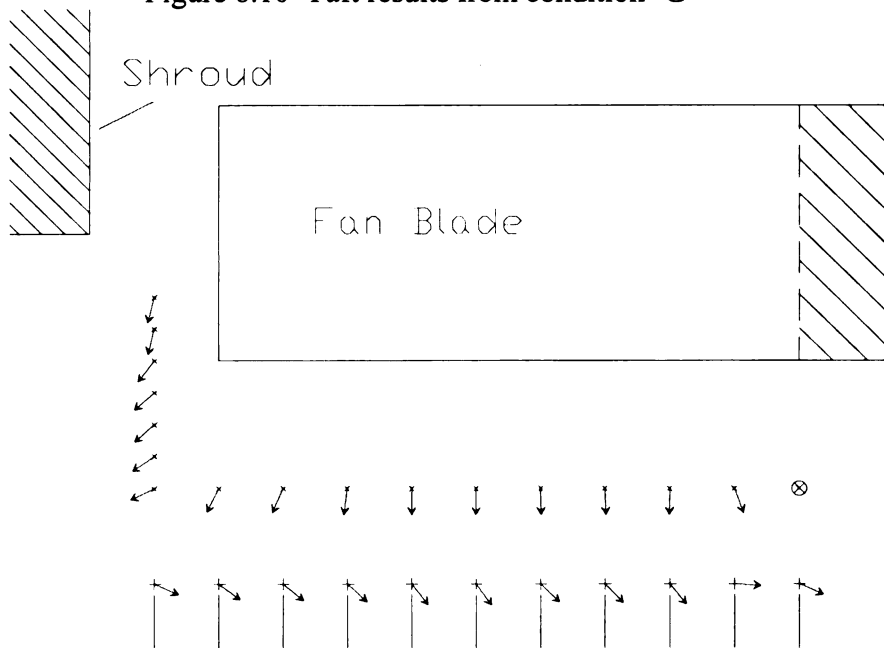
See Figure 6.1 for definition of symbols

Figure 6.11 Tuft results from condition 'H'
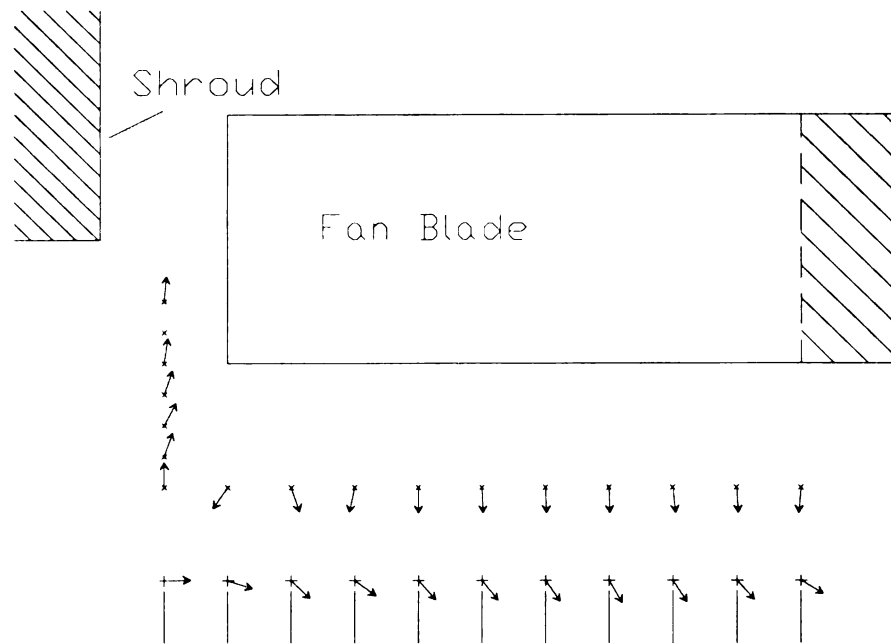
See Figure 6.1 for definition of symbols

Figure 6.12 Tuft results from condition 'I'
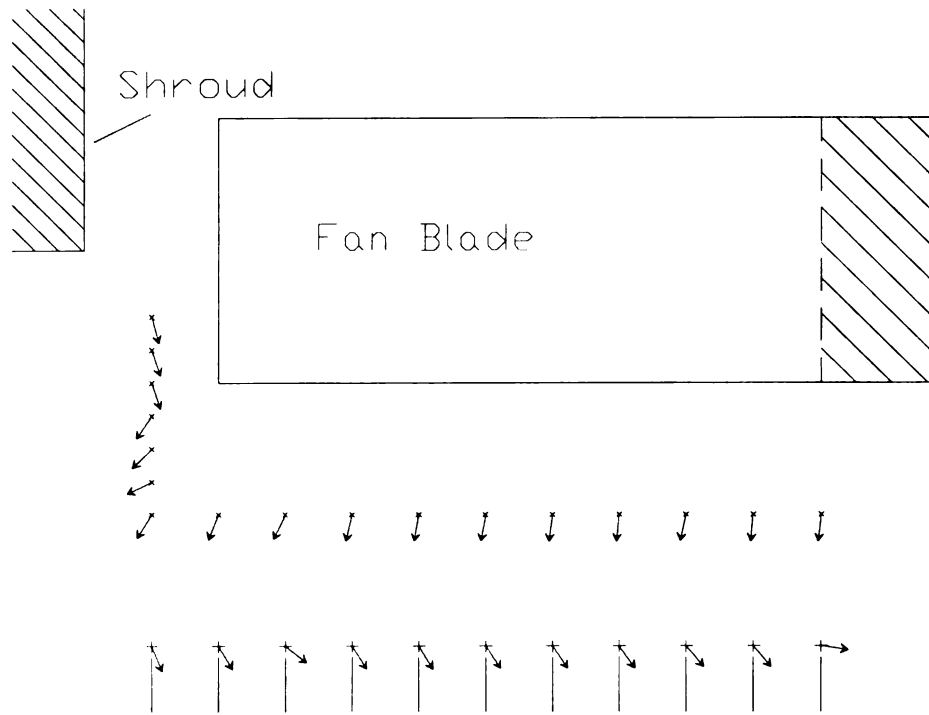
See Figure 6.1 for definition of symbols

Figure 6.13 Tuft results from condition 'J'
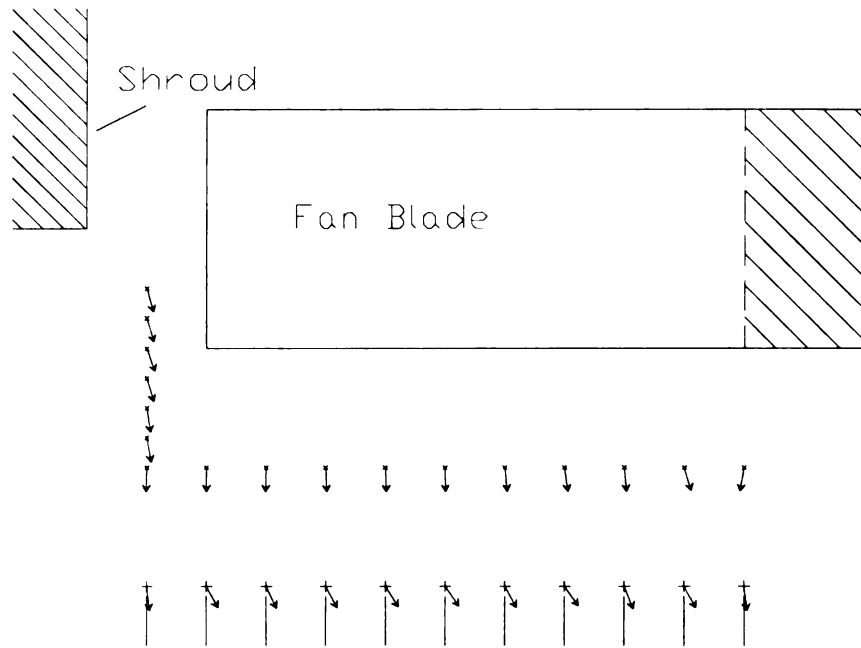
Figure 6.14 Tuft results from condition 'K'
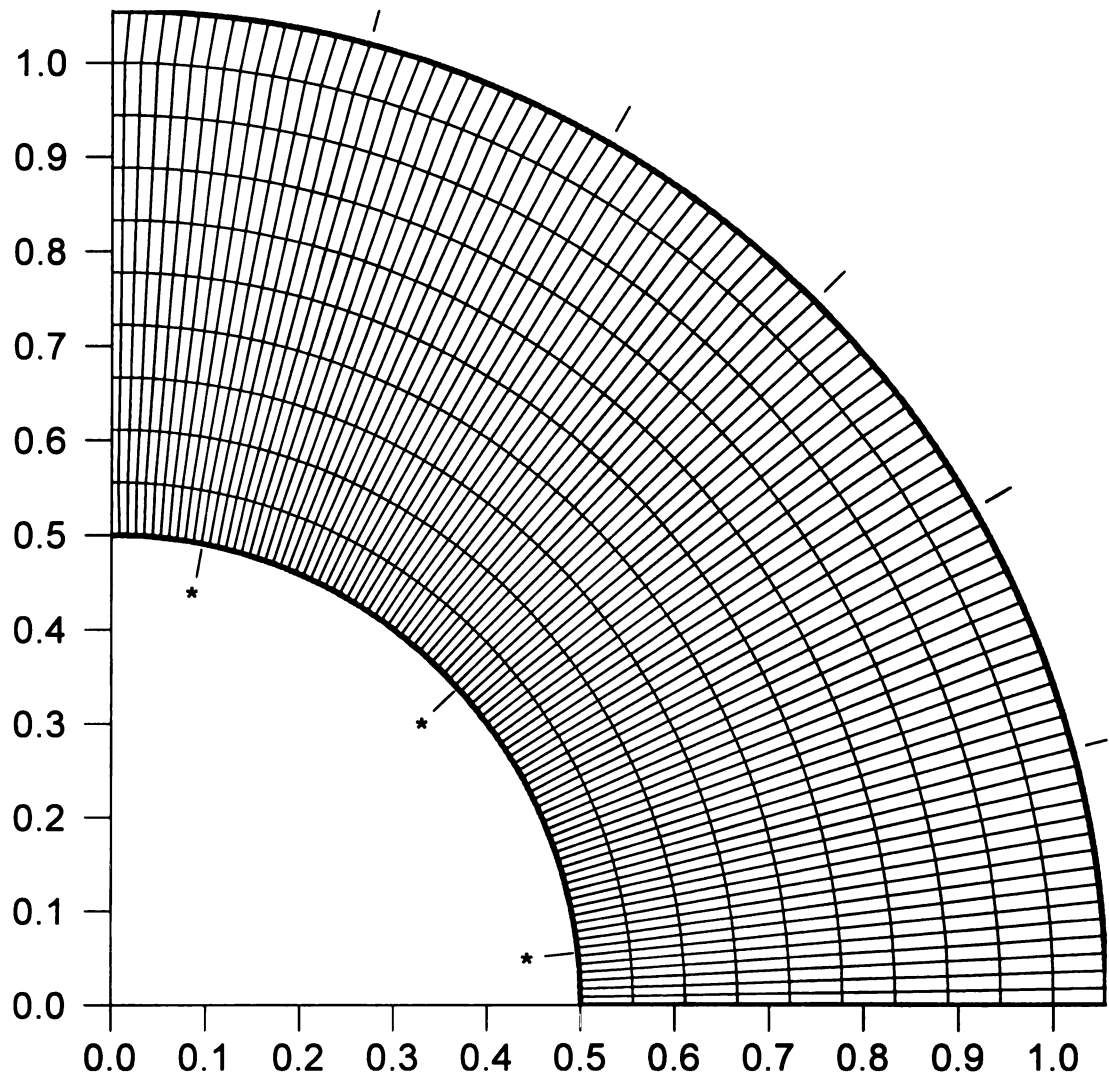
Figure 6.15 Mesh of experimental data locations
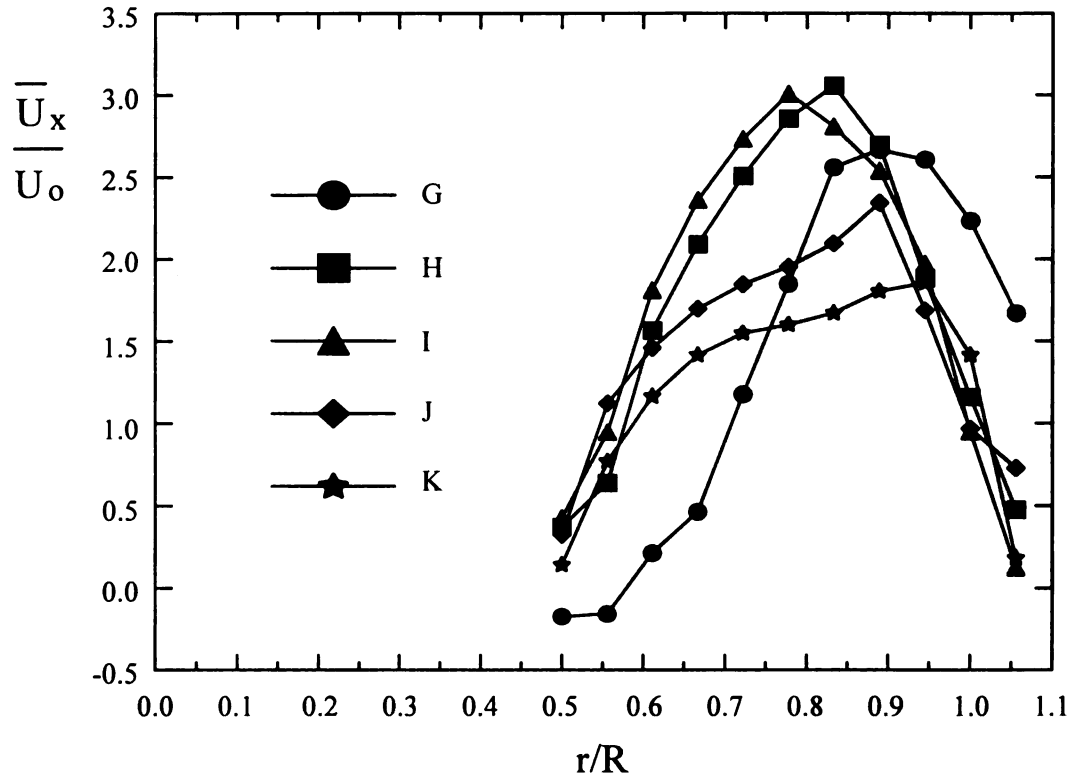
Figure 6.16a Time averaged mean axial velocity normalized by U_o
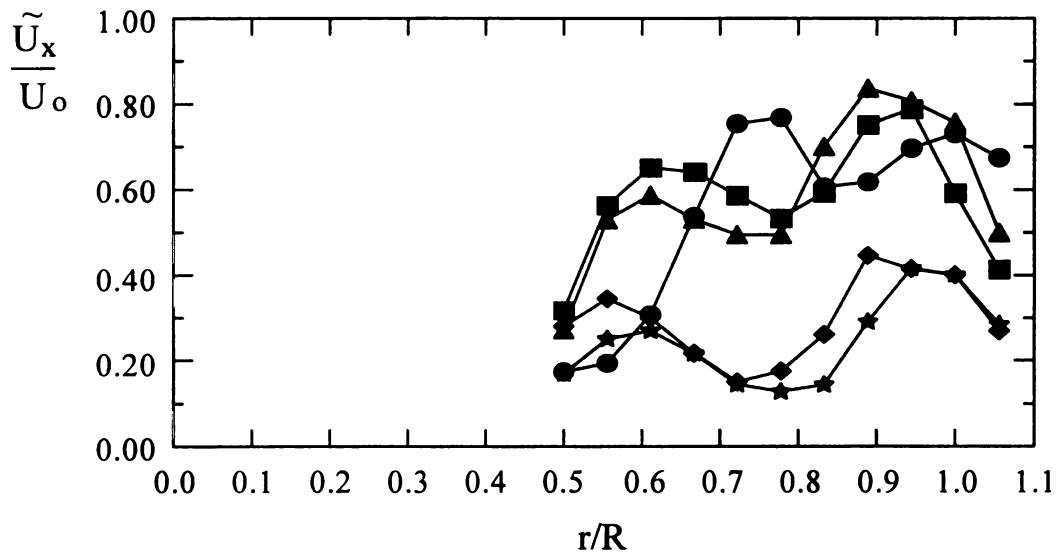
Figure 6.16b Time averaged RMS of axial velocity normalized by U_o
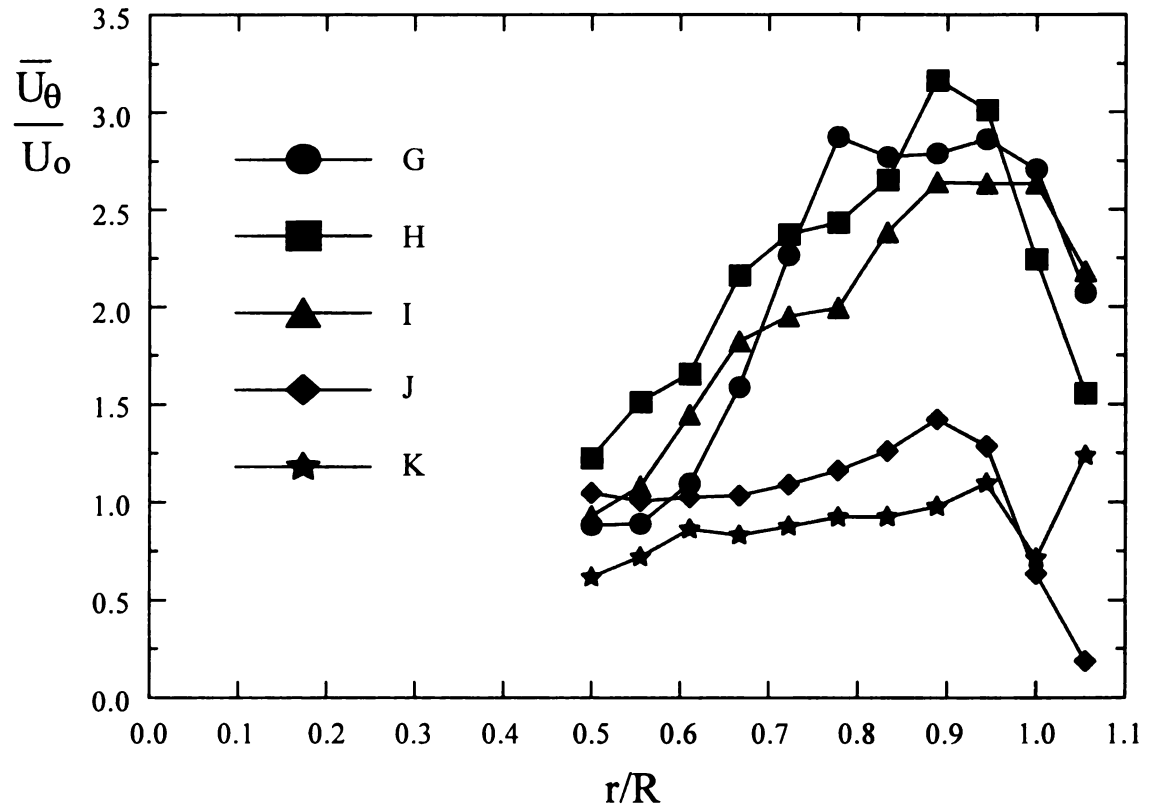
Figure 6.17a Time averaged mean tangential velocity normalized by U_o
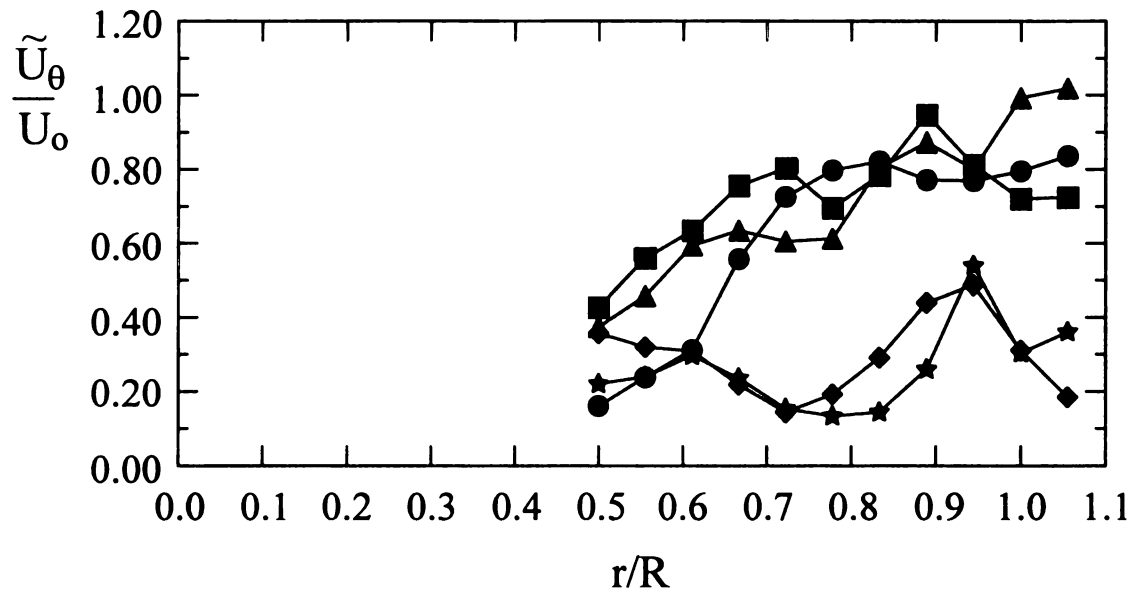
Figure 6.17b Time averaged RMS of tangential velocity normalized by U_o
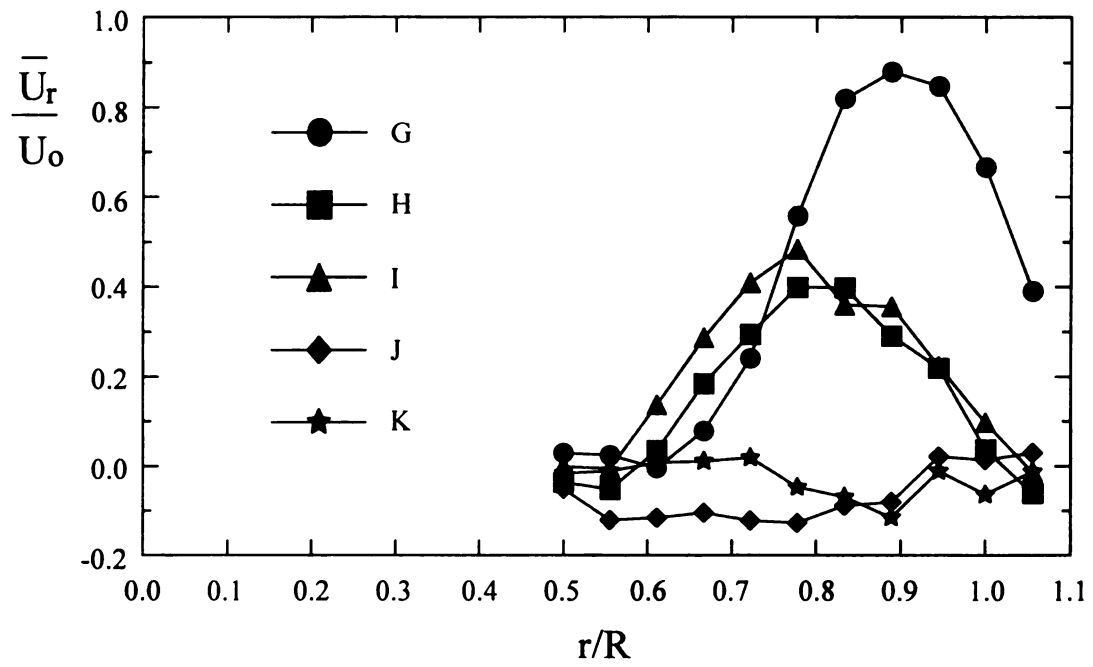
Figure 6.18a Time averaged mean radial velocity normalized by U_o
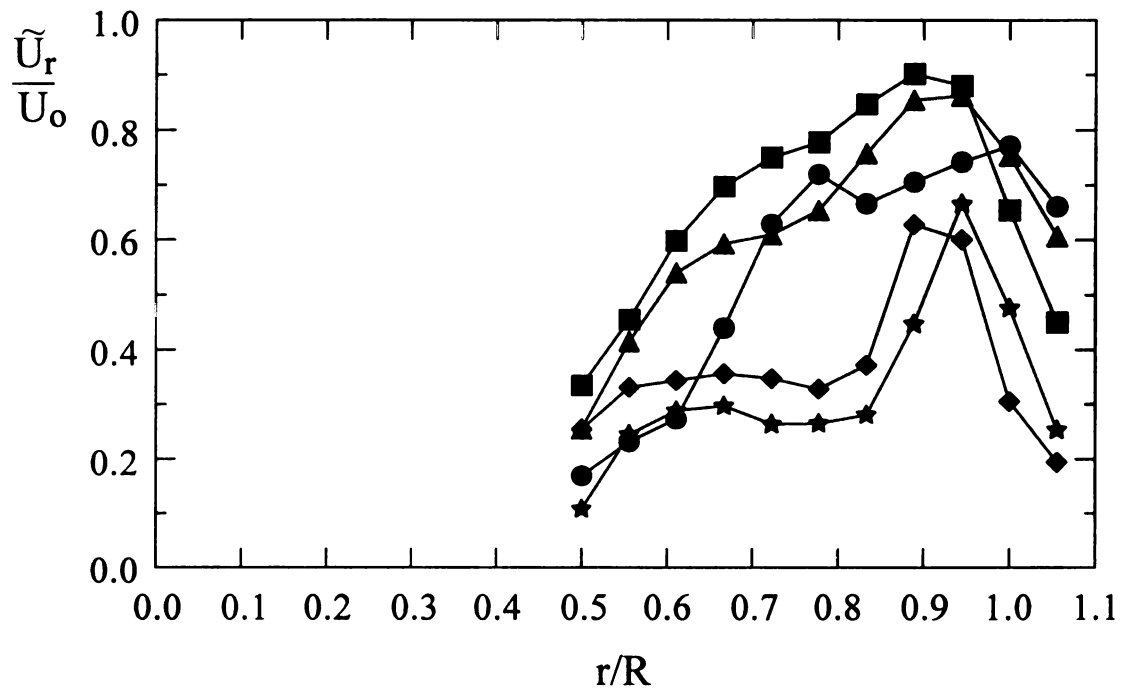
Figure 6.18b Time averaged RMS of radial velocity normalized by U_o
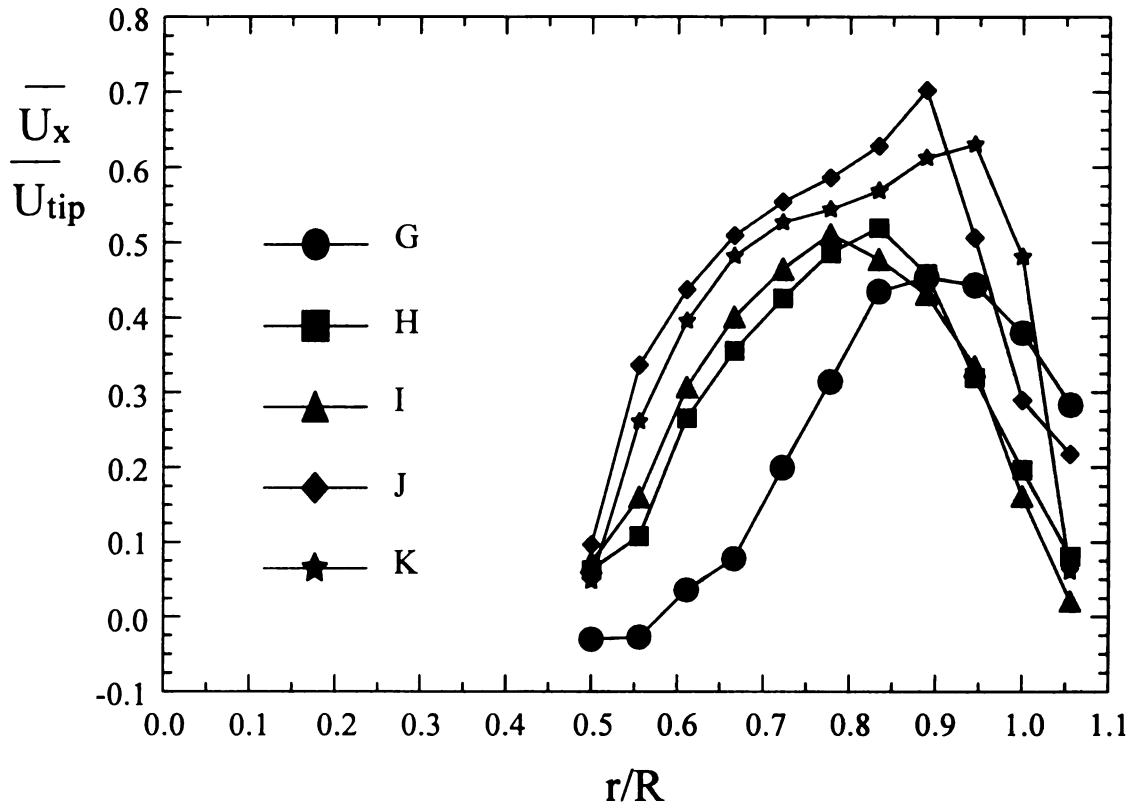
Figure 6.19a Time averaged mean axial velocity normalized by U_{tip}
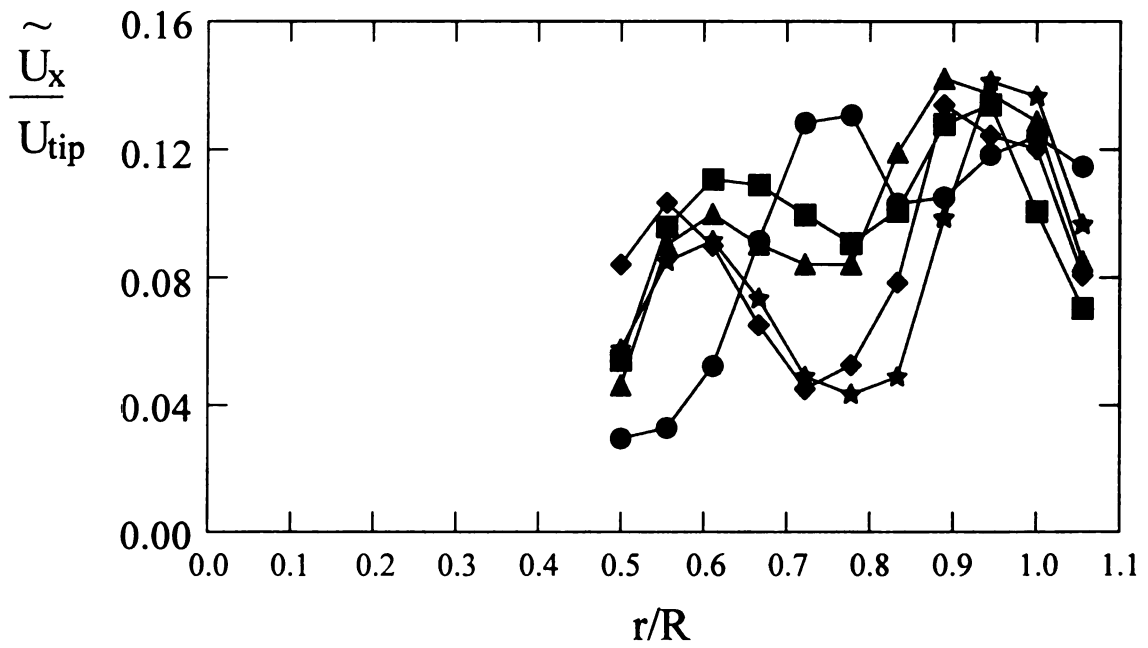
Figure 6.19 Time averaged RMS of axial velocity normalized by U_{tip}
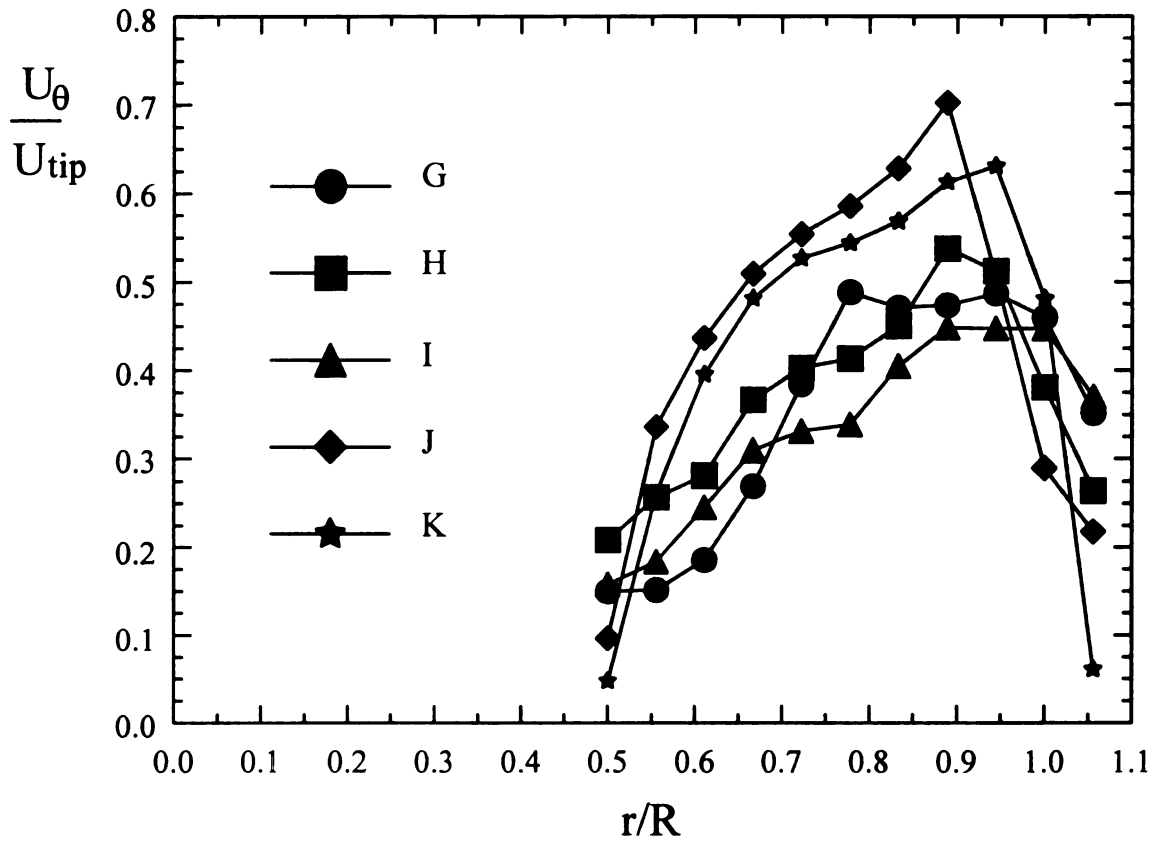
Figure 6.20a Time averaged mean tangential velocity normalized by U_{tip}
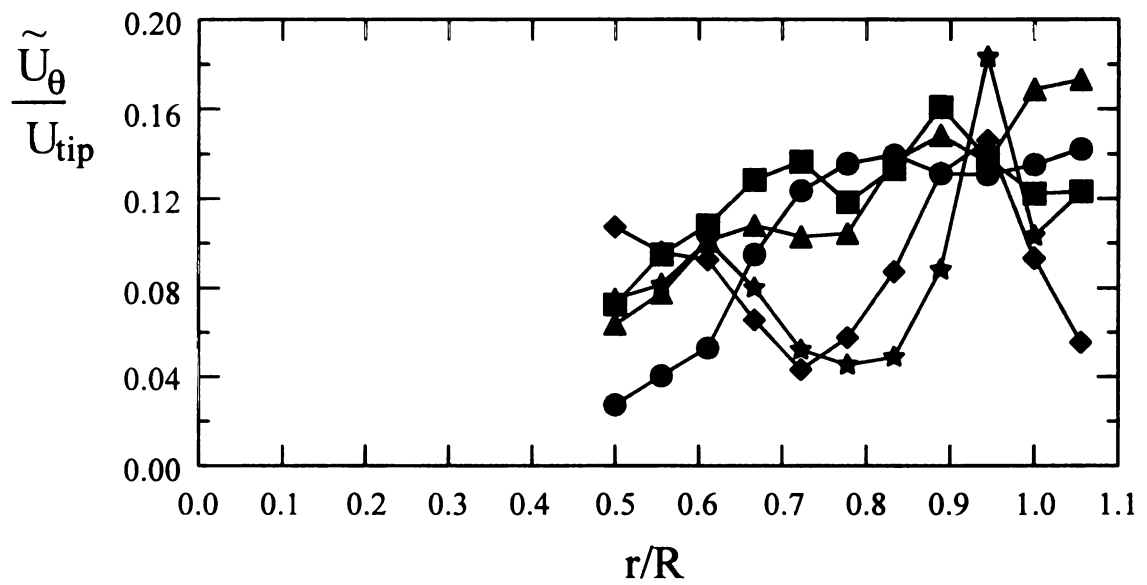
Figure 6.20b Time averaged RMS of tangential velocity normalized by U_{tip}
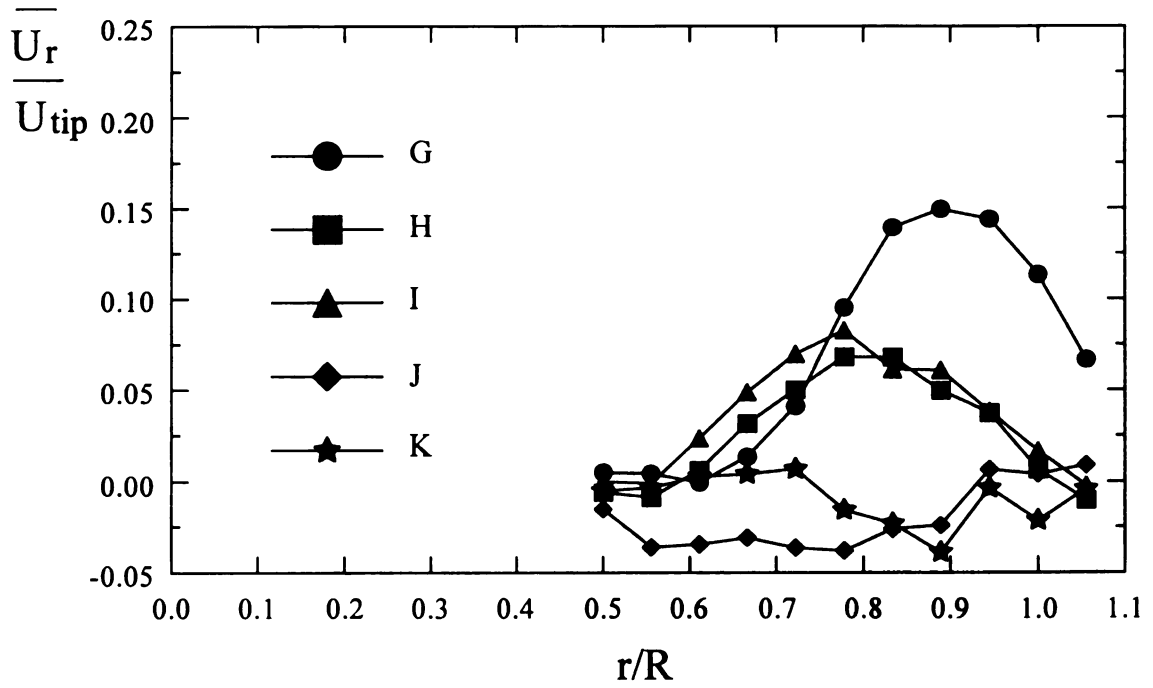
Figure 6.21a Time averaged mean radial velocity normalized by U_{tip}
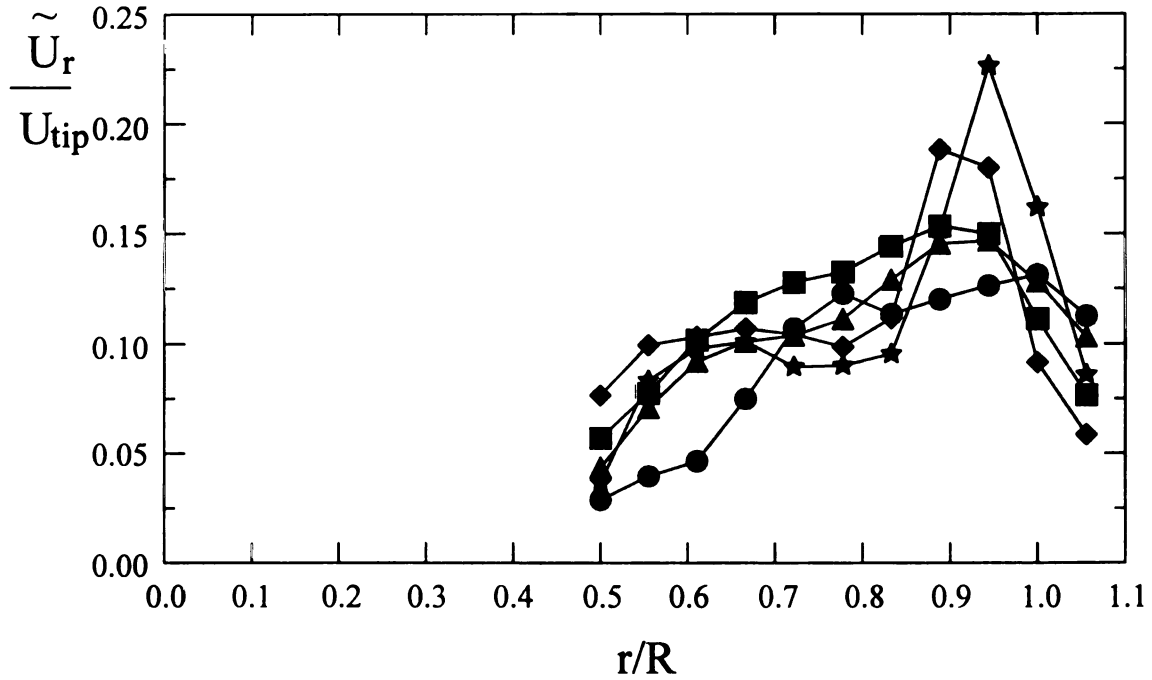
Figure 6.21b Time averaged RMS of radial velocity normalized by U_{tip}

Contour Number	$\dfrac{\overline{U}_x}{U_o}$	$\dfrac{\overline{U}_x}{U_{tip}}$
15	2.878	0.489
14	2.671	0.454
13	2.465	0.419
12	2.259	0.384
11	2.052	0.349
10	1.846	0.314
9	1.640	0.279
8	1.434	0.244
7	1.227	0.209
6	1.021	0.174
5	0.815	0.138
4	0.608	0.103
3	0.402	0.068
2	0.196	0.033
1	-0.011	-0.002
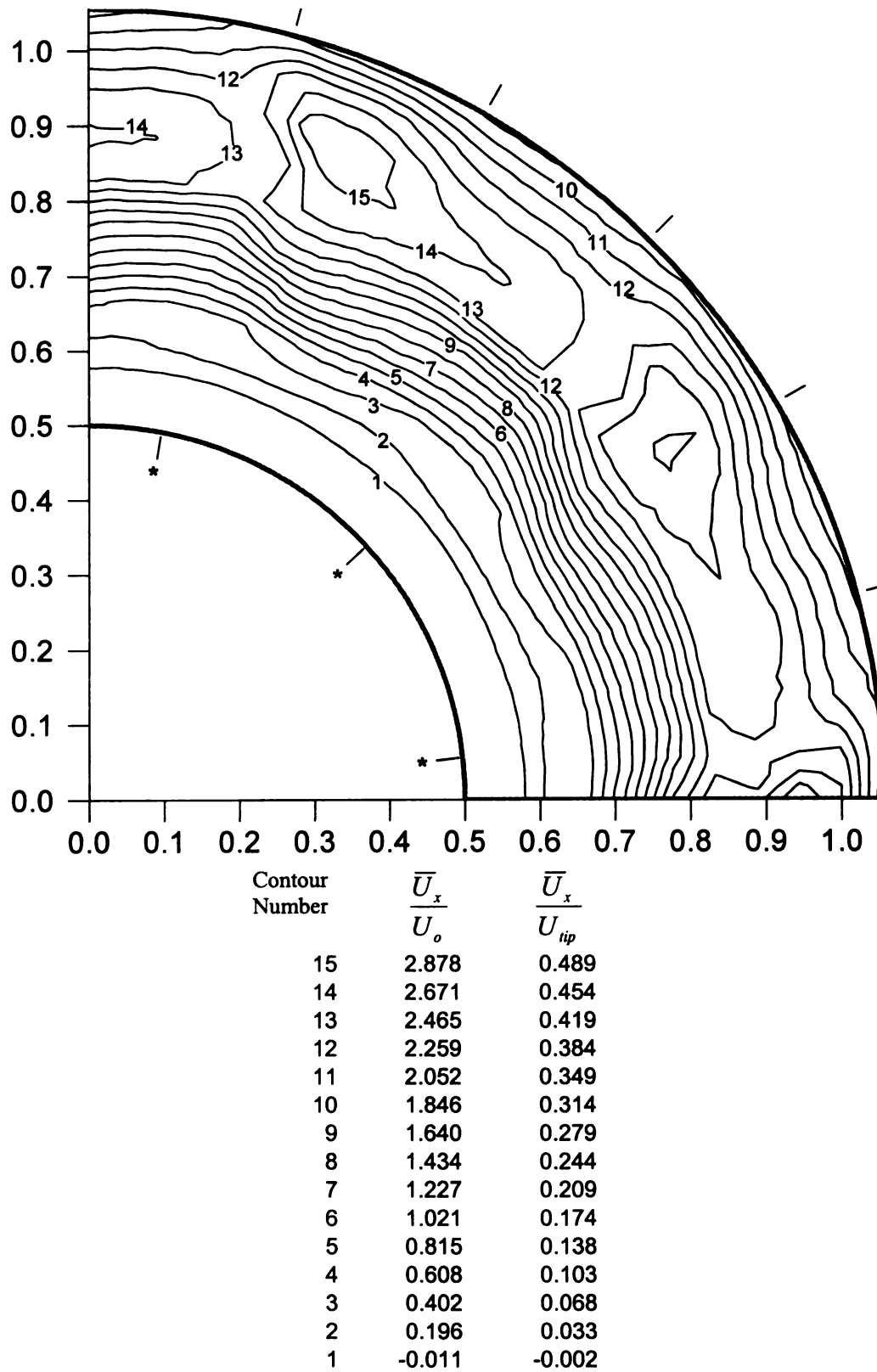
Figure 6.22 Phase averaged mean axial velocity for condition 'G'
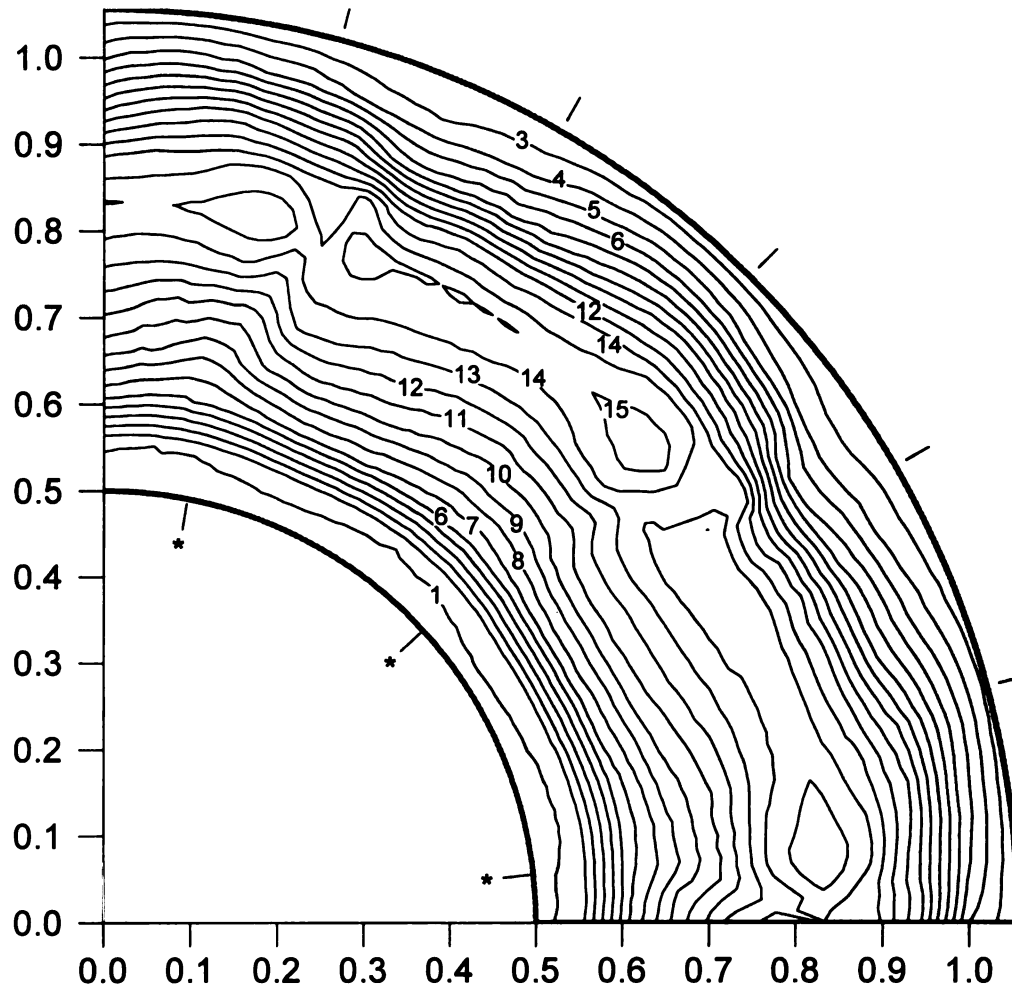
Contour Number	$\dfrac{\overline{U}_x}{U_o}$	$\dfrac{\overline{U}_x}{U_{tip}}$
15	3.083	0.524
14	2.899	0.493
13	2.716	0.462
12	2.532	0.430
11	2.348	0.399
10	2.165	0.368
9	1.981	0.337
8	1.798	0.306
7	1.614	0.274
6	1.430	0.243
5	1.247	0.212
4	1.063	0.181
3	0.880	0.150
2	0.696	0.118
1	0.512	0.087

Figure 6.23 Phase averaged mean axial velocity for condition 'H'
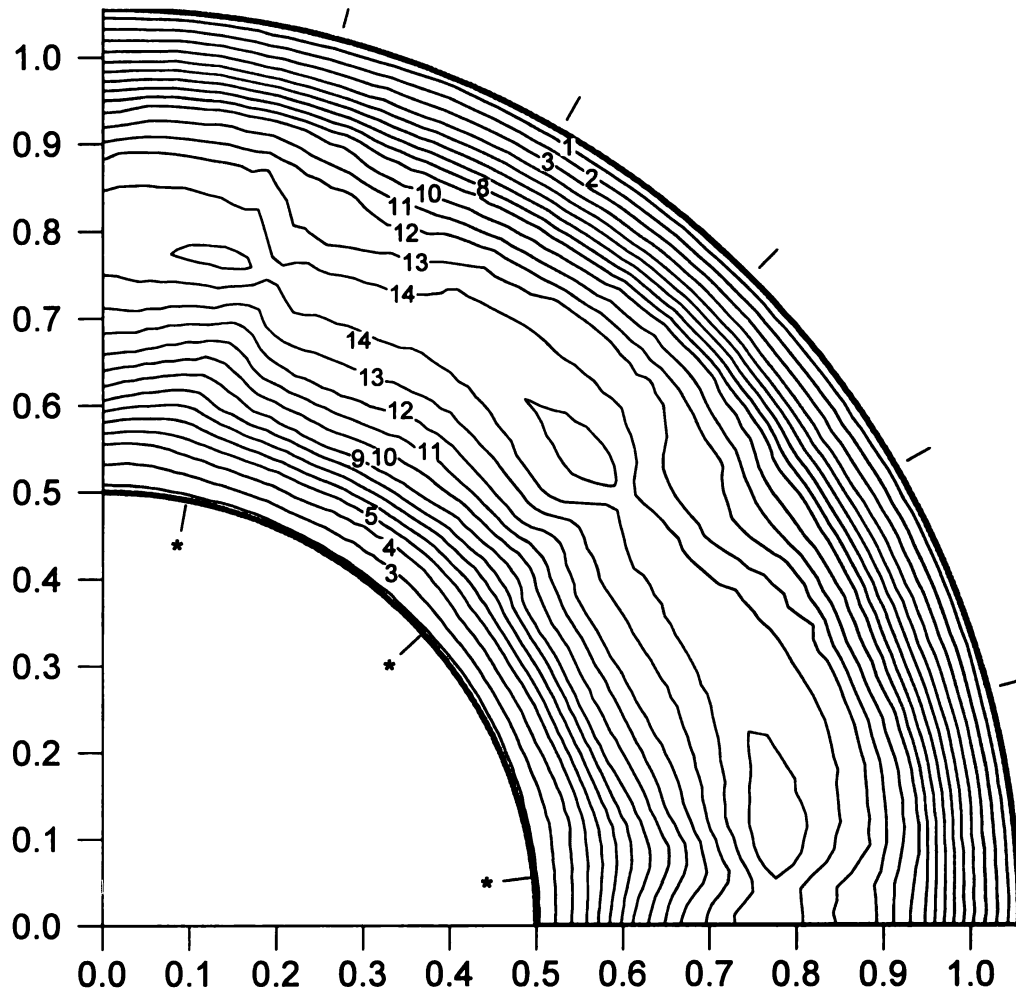
Contour Number	$\dfrac{\overline{U}_x}{U_o}$	$\dfrac{\overline{U}_x}{U_{tip}}$
15	3.039	0.517
14	2.841	0.483
13	2.644	0.450
12	2.447	0.416
11	2.250	0.383
10	2.053	0.349
9	1.856	0.316
8	1.659	0.282
7	1.462	0.248
6	1.265	0.215
5	1.067	0.181
4	0.870	0.148
3	0.673	0.114
2	0.476	0.081
1	0.279	0.047

Figure 6.24 Phase averaged mean axial velocity for condition 'I'
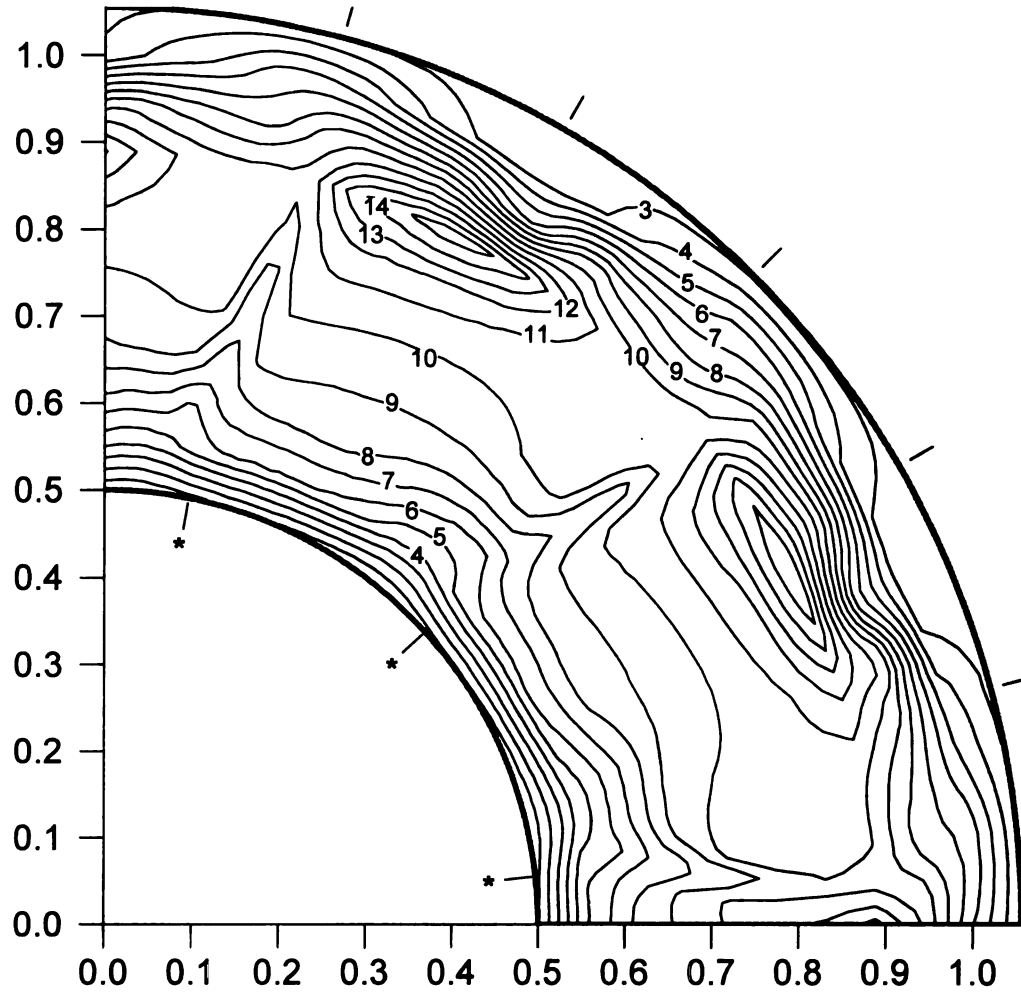
Contour Number	$\dfrac{\overline{U}_x}{U_o}$	$\dfrac{\overline{U}_x}{U_{tip}}$
15	2.723	0.817
14	2.559	0.768
13	2.394	0.718
12	2.229	0.669
11	2.065	0.619
10	1.900	0.570
9	1.736	0.521
8	1.571	0.471
7	1.406	0.422
6	1.242	0.373
5	1.077	0.323
4	0.913	0.274
3	0.748	0.224
2	0.584	0.175
1	0.419	0.126

Figure 6.25 Phase averaged mean axial velocity for condition 'J'

Contour Number	$\dfrac{\overline{U}_x}{U_o}$	$\dfrac{\overline{U}_x}{U_{tip}}$
15	2.171	0.738
14	2.027	0.689
13	1.883	0.640
12	1.740	0.592
11	1.596	0.543
10	1.453	0.494
9	1.309	0.445
8	1.165	0.396
7	1.022	0.347
6	0.878	0.299
5	0.735	0.250
4	0.591	0.201
3	0.447	0.152
2	0.304	0.103
1	0.160	0.054
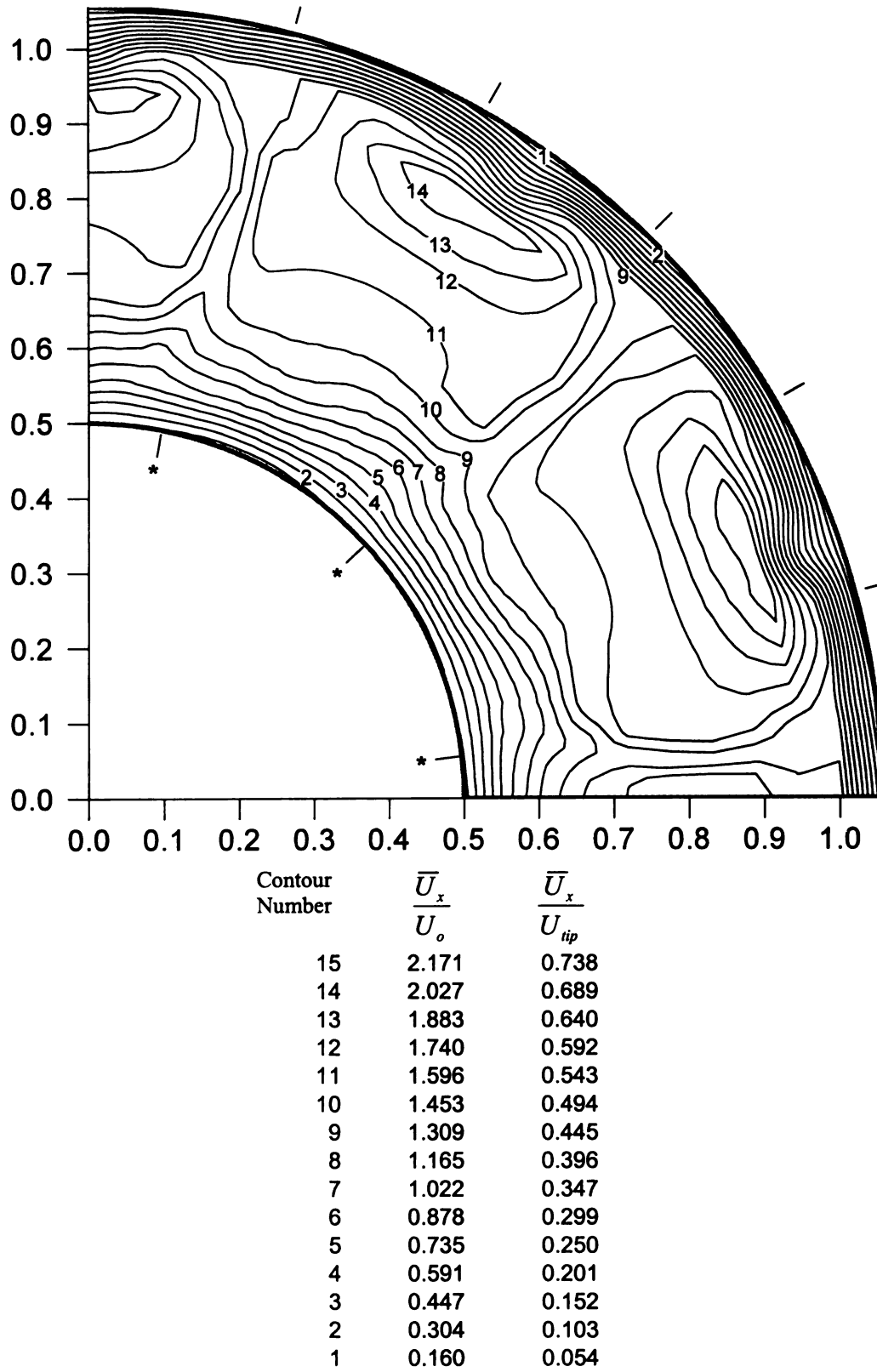
Figure 6.26 Phase averaged mean axial velocity for condition 'K'

Contour Number	$\dfrac{\overline{U}_\theta}{U_o}$	$\dfrac{\overline{U}_\theta}{U_{tip}}$
15	3.238	0.551
14	3.077	0.523
13	2.916	0.496
12	2.755	0.468
11	2.594	0.441
10	2.433	0.414
9	2.272	0.386
8	2.111	0.359
7	1.949	0.331
6	1.788	0.304
5	1.627	0.277
4	1.466	0.249
3	1.305	0.222
2	1.144	0.194
1	0.983	0.167
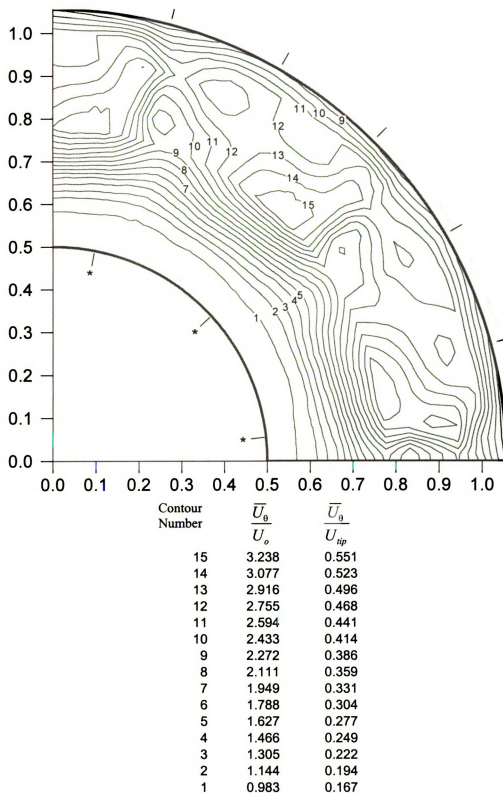
Figure 6.27 Phase averaged mean tangential velocity for condition 'G'

Contour Number	$\dfrac{\overline{U}_\theta}{U_o}$	$\dfrac{\overline{U}_\theta}{U_{tip}}$
15	4.024	0.684
14	3.836	0.652
13	3.648	0.620
12	3.460	0.588
11	3.271	0.556
10	3.083	0.524
9	2.895	0.492
8	2.706	0.460
7	2.518	0.428
6	2.330	0.396
5	2.142	0.364
4	1.953	0.332
3	1.765	0.300
2	1.577	0.268
1	1.388	0.236
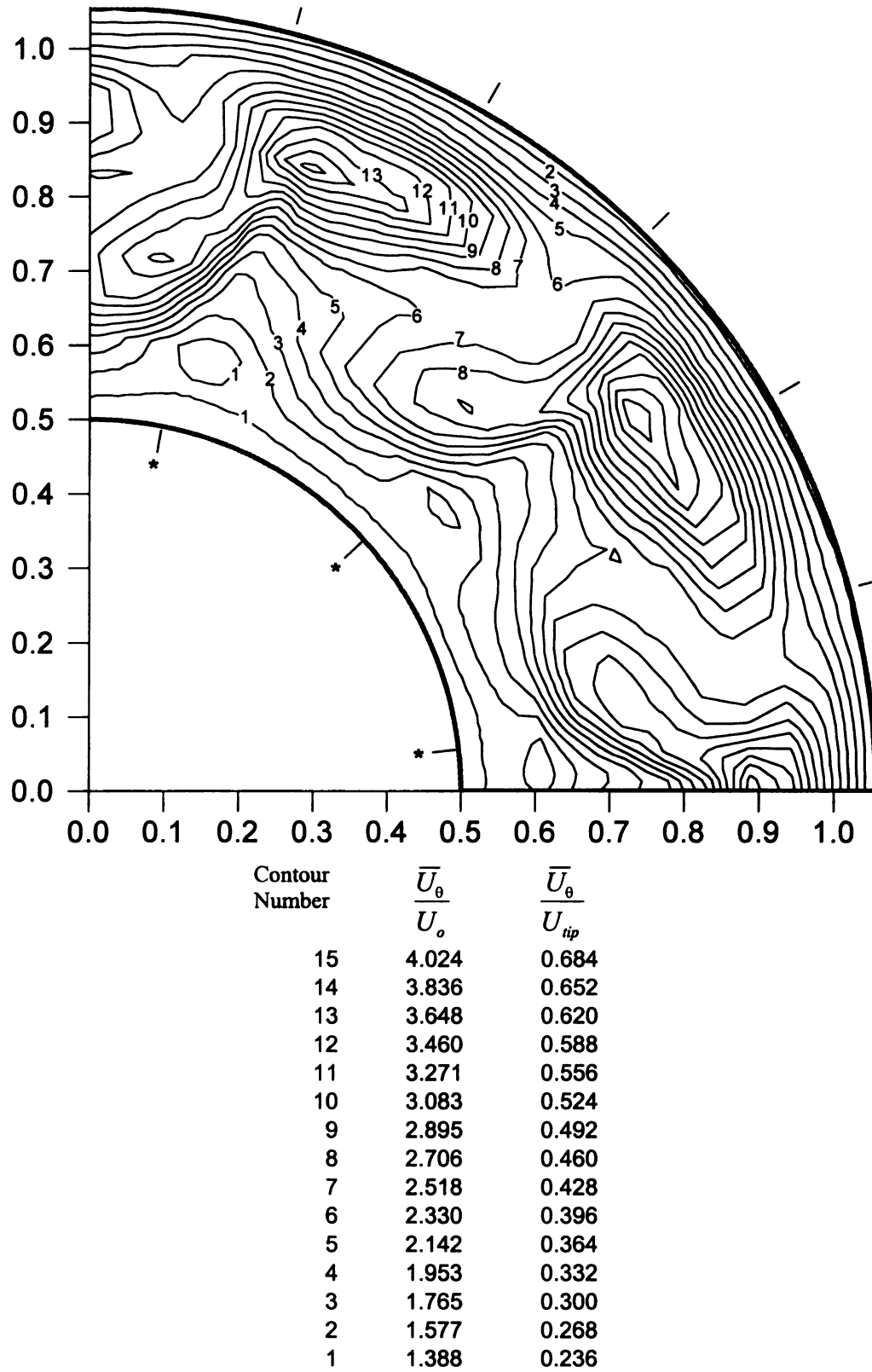
Figure 6.28 Phase averaged mean tangential velocity for condition 'H'

Contour Number	$\dfrac{\overline{U}_\theta}{U_o}$	$\dfrac{\overline{U}_\theta}{U_{tip}}$
15	3.062	0.521
14	2.917	0.496
13	2.773	0.471
12	2.628	0.447
11	2.483	0.422
10	2.338	0.397
9	2.193	0.373
8	2.048	0.348
7	1.903	0.324
6	1.758	0.299
5	1.613	0.274
4	1.468	0.250
3	1.324	0.225
2	1.179	0.200
1	1.034	0.176
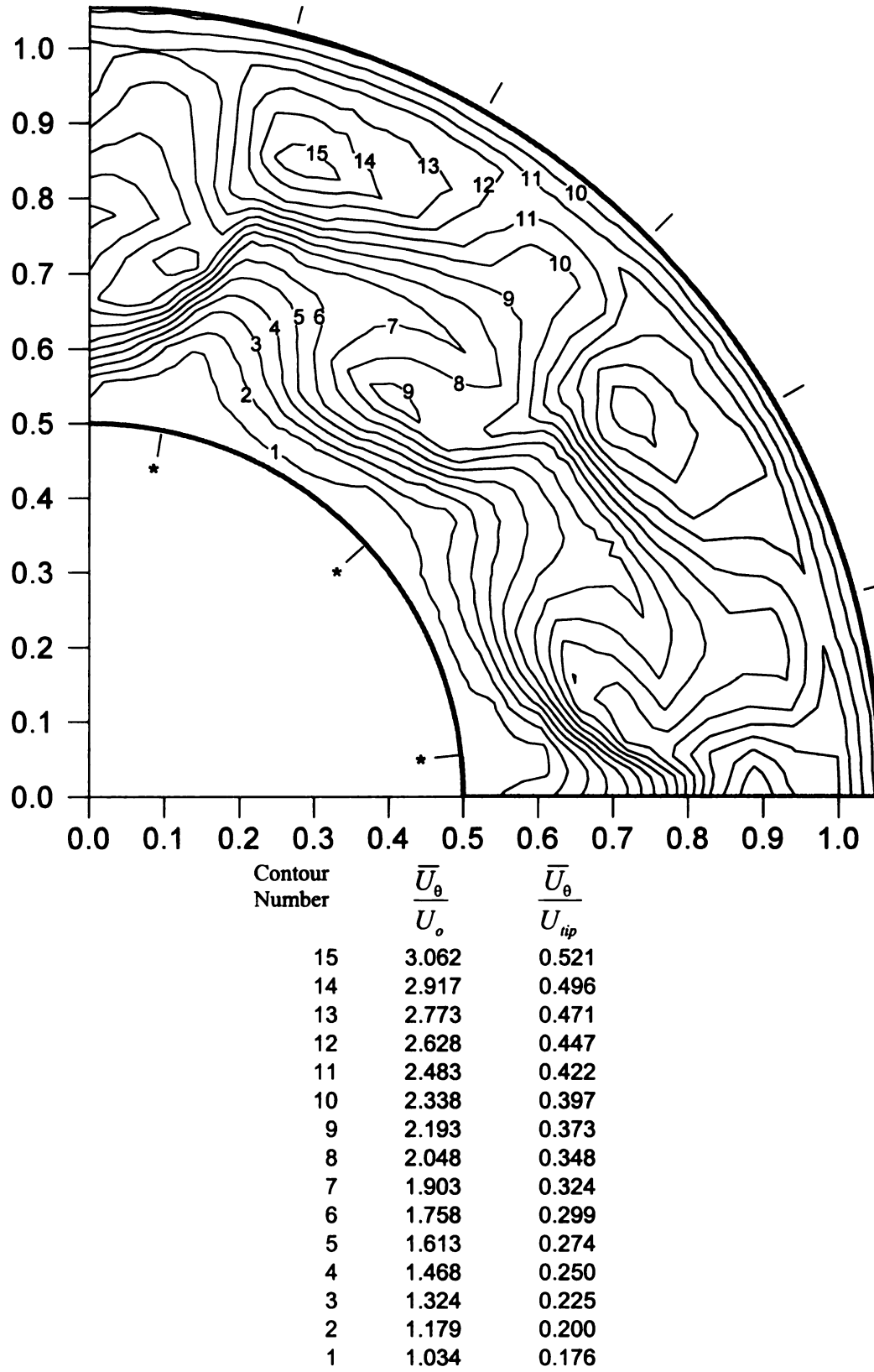
Figure 6.29 Phase averaged mean tangential velocity for condition 'I'

Contour Number	$\dfrac{\overline{U_\theta}}{U_o}$	$\dfrac{\overline{U_\theta}}{U_{tip}}$
15	1.814	0.544
14	1.702	0.510
13	1.589	0.477
12	1.477	0.443
11	1.365	0.410
10	1.253	0.376
9	1.141	0.342
8	1.029	0.309
7	0.917	0.275
6	0.805	0.242
5	0.693	0.208
4	0.581	0.174
3	0.469	0.141
2	0.357	0.107
1	0.245	0.073
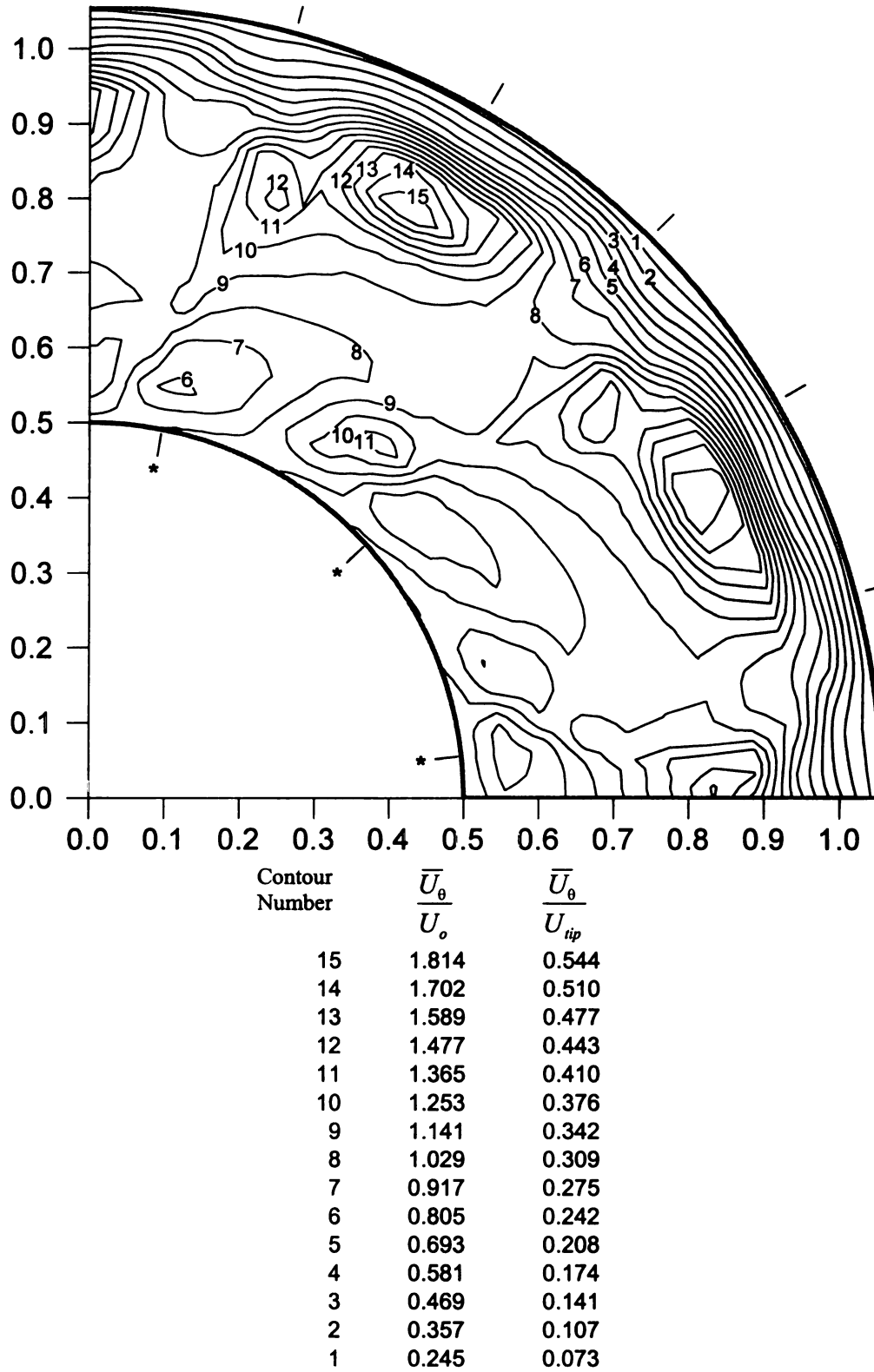
Figure 6.30 Phase averaged mean tangential velocity for condition 'J'

Contour Number	$\dfrac{\overline{U}_\theta}{U_o}$	$\dfrac{\overline{U}_\theta}{U_{tip}}$
15	1.890	0.643
14	1.795	0.610
13	1.700	0.578
12	1.604	0.545
11	1.509	0.513
10	1.414	0.481
9	1.319	0.448
8	1.223	0.416
7	1.128	0.384
6	1.033	0.351
5	0.938	0.319
4	0.843	0.286
3	0.747	0.254
2	0.652	0.222
1	0.557	0.189
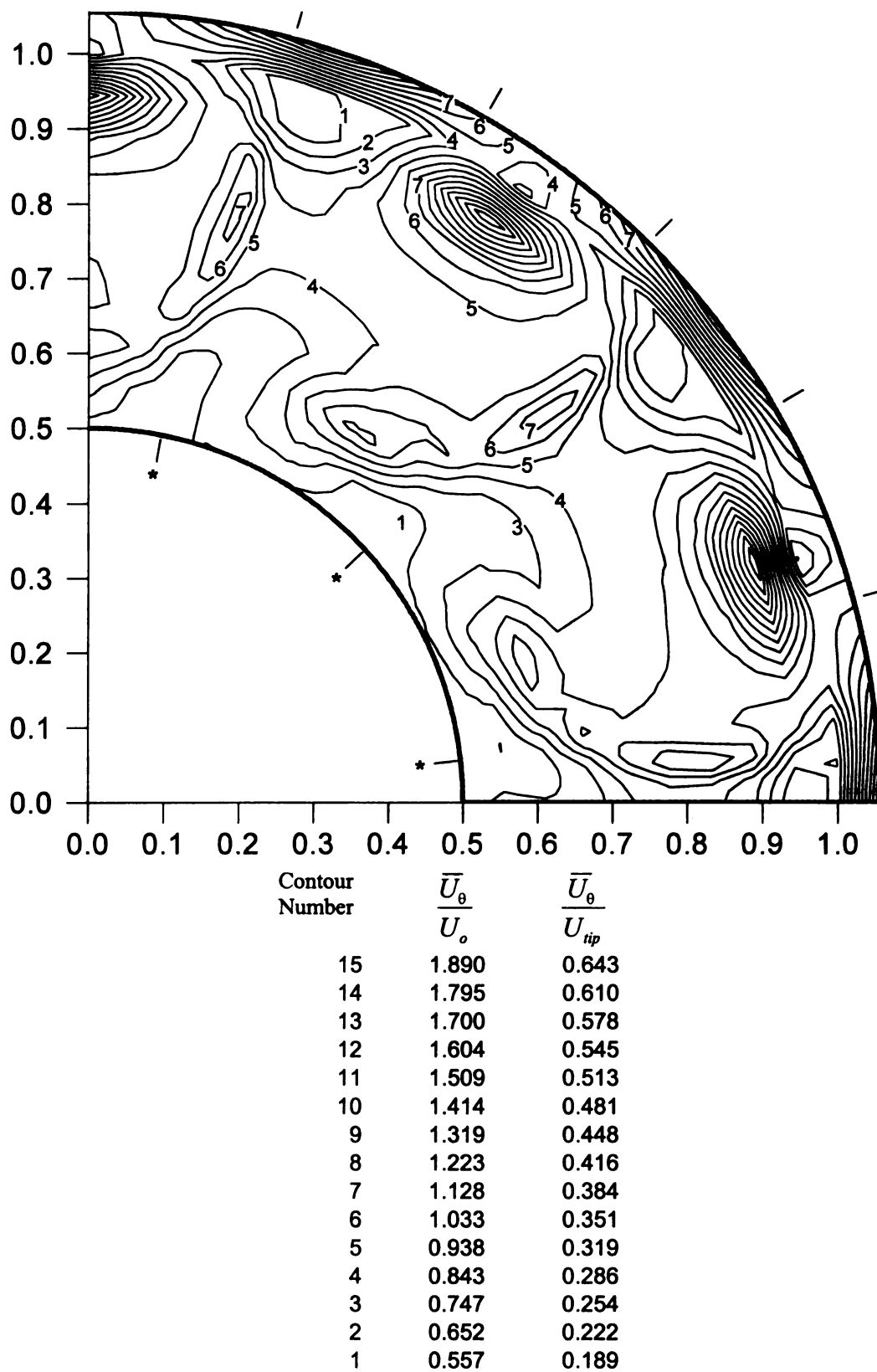
Figure 6.31 Phase averaged mean tangential velocity for condition 'K'

Contour Number	$\dfrac{\overline{U}_r}{U_o}$	$\dfrac{\overline{U}_r}{U_{tip}}$
15	1.165	0.198
14	1.074	0.183
13	0.983	0.167
12	0.892	0.152
11	0.801	0.136
10	0.710	0.121
9	0.619	0.105
8	0.528	0.090
7	0.437	0.074
6	0.346	0.059
5	0.255	0.043
4	0.164	0.028
3	0.073	0.012
2	-0.019	-0.003
1	-0.110	-0.019

Figure 6.32 Phase averaged mean radial velocity for condition 'G'

Contour Number	$\dfrac{\overline{U}_r}{U_o}$	$\dfrac{\overline{U}_r}{U_{tip}}$
15	0.974	0.165
14	0.832	0.142
13	0.691	0.118
12	0.550	0.094
11	0.409	0.070
10	0.268	0.046
9	0.127	0.022
8	-0.014	-0.002
7	-0.155	-0.026
6	-0.296	-0.050
5	-0.437	-0.074
4	-0.578	-0.098
3	-0.719	-0.122
2	-0.860	-0.146
1	-1.002	-0.170
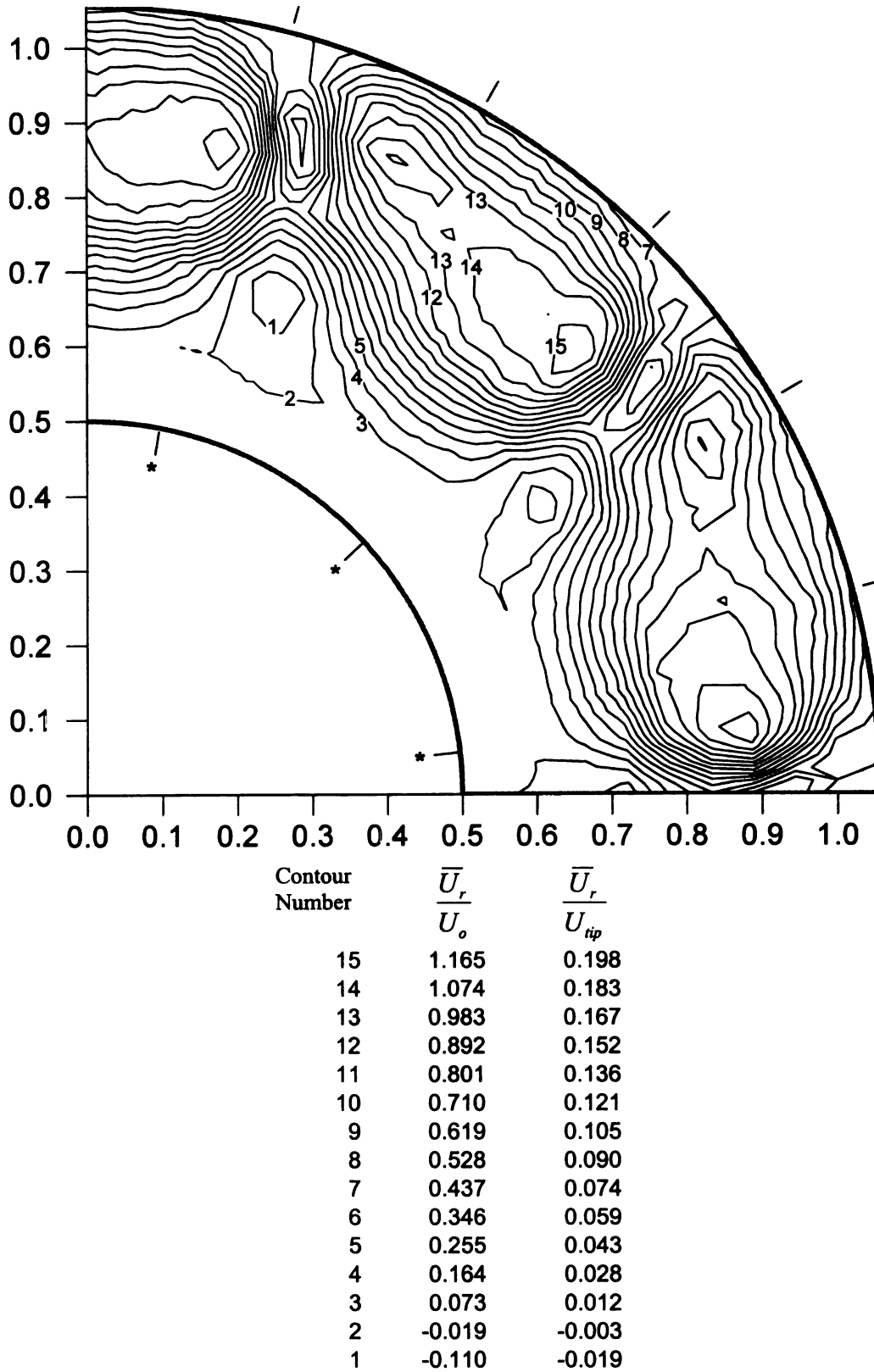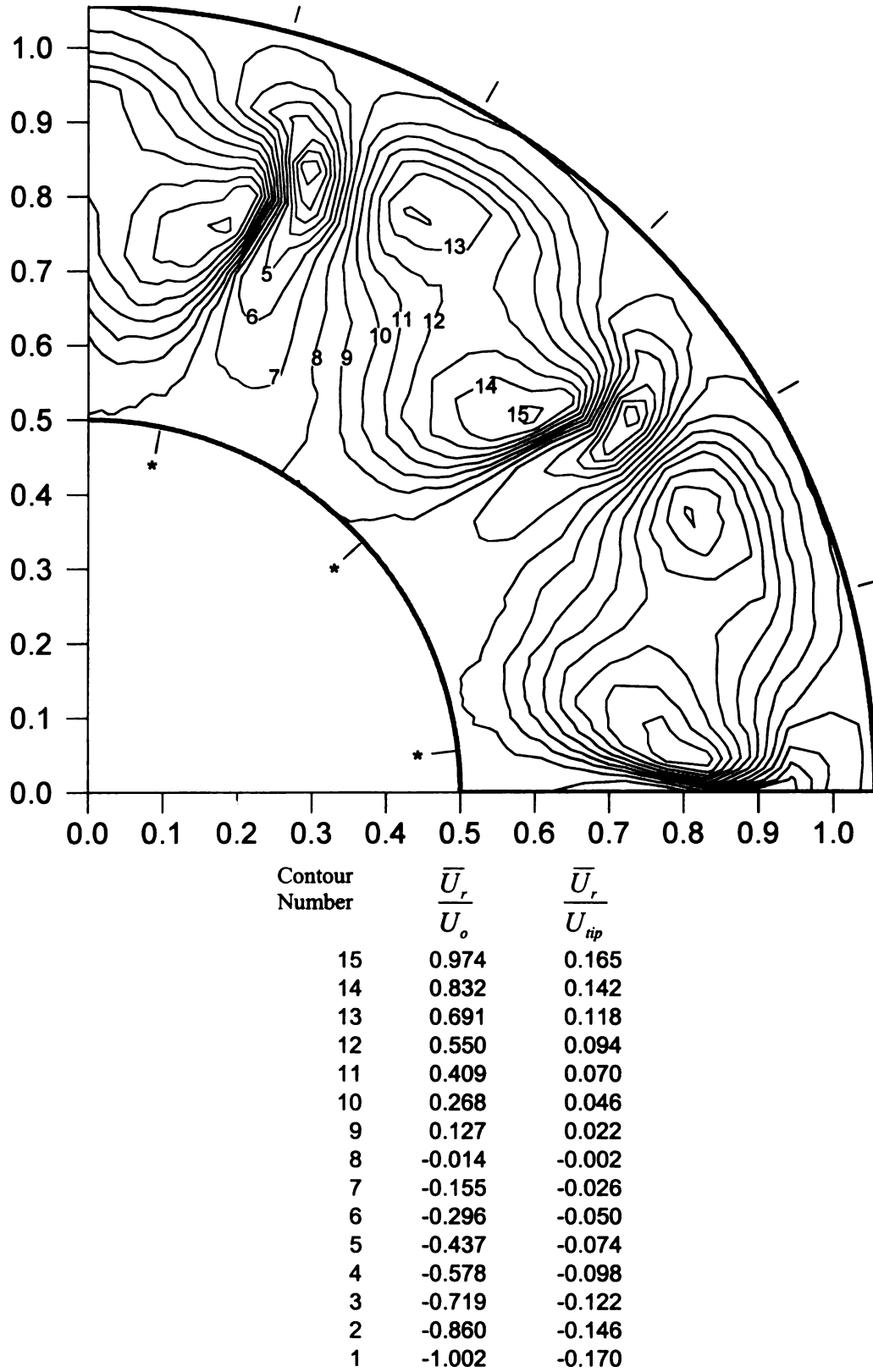
Figure 6.33 Phase averaged mean radial velocity for condition 'H'

Contour Number	$\dfrac{\overline{U}_r}{U_o}$	$\dfrac{\overline{U}_r}{U_{tip}}$
15	0.868	0.148
14	0.793	0.135
13	0.718	0.122
12	0.643	0.109
11	0.568	0.097
10	0.493	0.084
9	0.418	0.071
8	0.344	0.058
7	0.269	0.046
6	0.194	0.033
5	0.119	0.020
4	0.044	0.007
3	-0.031	-0.005
2	-0.106	-0.018
1	-0.181	-0.031
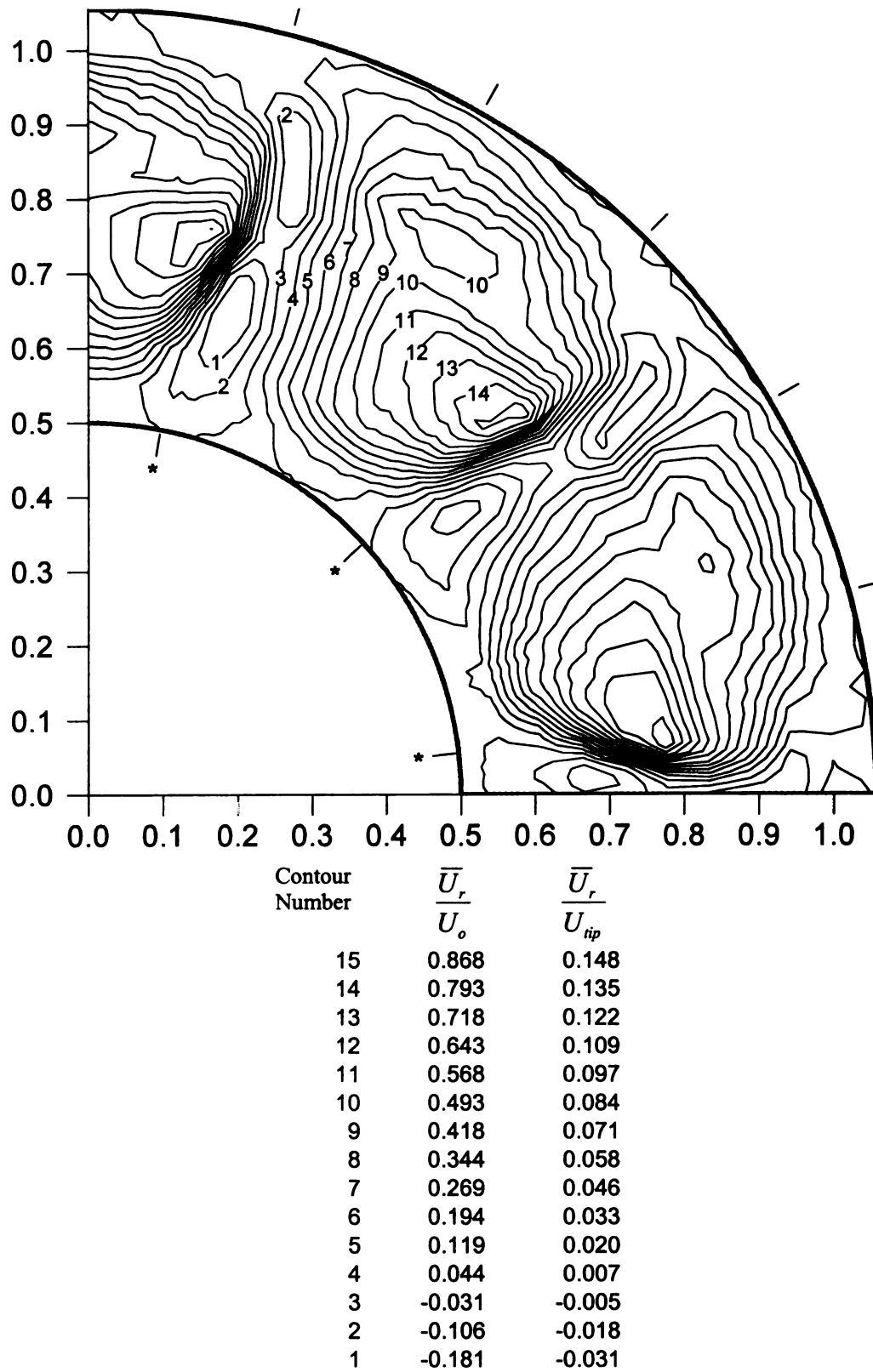
Figure 6.34 Phase averaged mean radial velocity for condition 'I'

Contour Number	$\dfrac{\overline{U}_r}{U_o}$	$\dfrac{\overline{U}_r}{U_{tip}}$
15	0.751	0.225
14	0.644	0.193
13	0.536	0.161
12	0.428	0.128
11	0.321	0.096
10	0.213	0.064
9	0.105	0.032
8	-0.002	-0.001
7	-0.110	-0.033
6	-0.218	-0.065
5	-0.325	-0.098
4	-0.433	-0.130
3	-0.541	-0.162
2	-0.648	-0.194
1	-0.756	-0.227
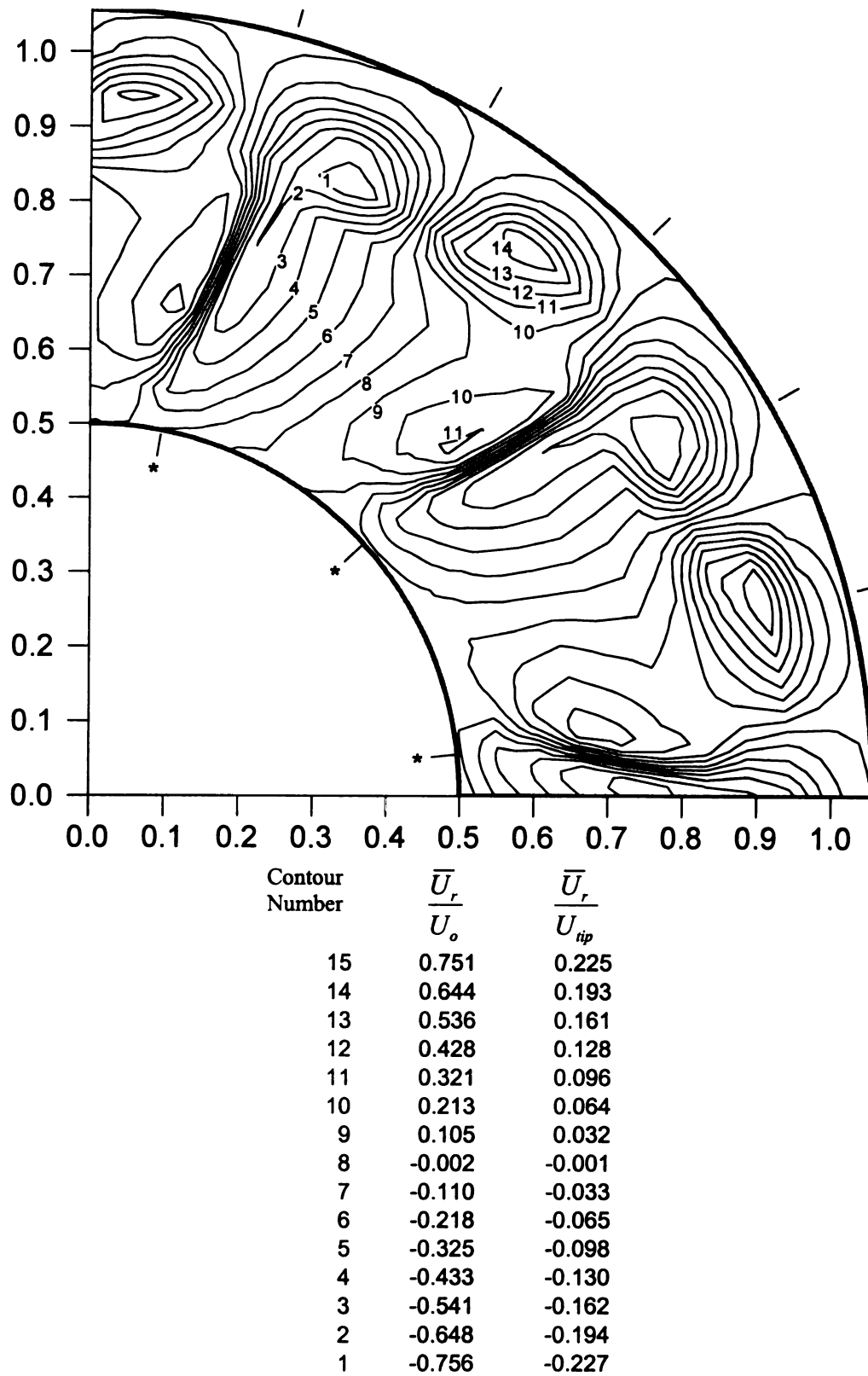
Figure 6.35 Phase averaged mean radial velocity for condition 'J'

Contour Number	$\dfrac{\overline{U}_r}{U_o}$	$\dfrac{\overline{U}_r}{U_{tip}}$
15	0.812	0.276
14	0.697	0.237
13	0.581	0.198
12	0.466	0.159
11	0.351	0.119
10	0.236	0.080
9	0.121	0.041
8	0.006	0.002
7	-0.110	-0.037
6	-0.225	-0.076
5	-0.340	-0.116
4	-0.455	-0.155
3	-0.570	-0.194
2	-0.685	-0.233
1	-0.801	-0.272
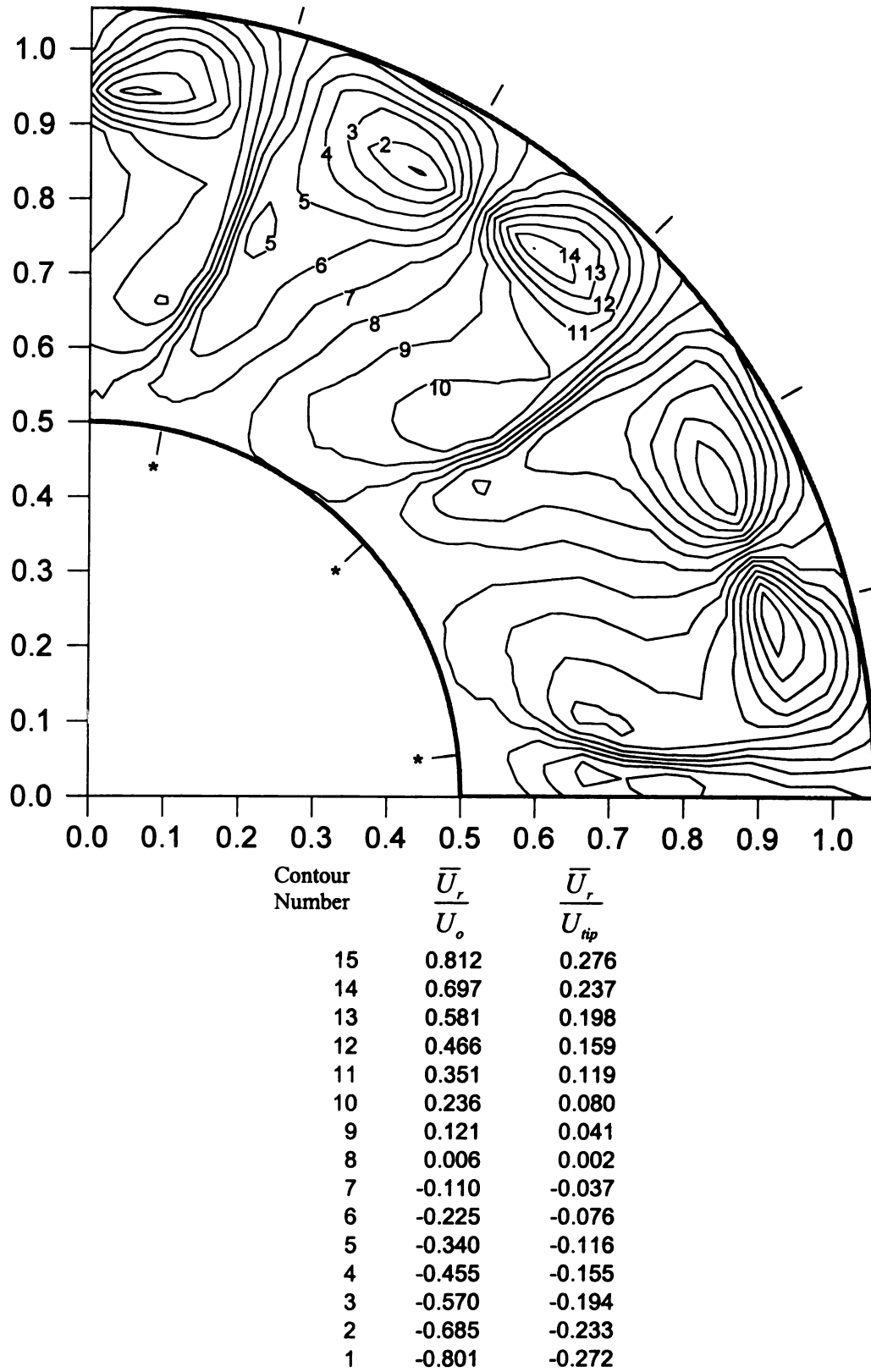
Figure 6.36 Phase averaged mean radial velocity for condition 'K'

Contour Number	$\dfrac{\widetilde{U}_x}{U_o}$	$\dfrac{\widetilde{U}_x}{U_{tip}}$
15	0.978	0.166
14	0.925	0.157
13	0.871	0.148
12	0.818	0.139
11	0.764	0.130
10	0.711	0.121
9	0.657	0.112
8	0.604	0.103
7	0.550	0.094
6	0.497	0.084
5	0.443	0.075
4	0.390	0.066
3	0.336	0.057
2	0.283	0.048
1	0.229	0.039
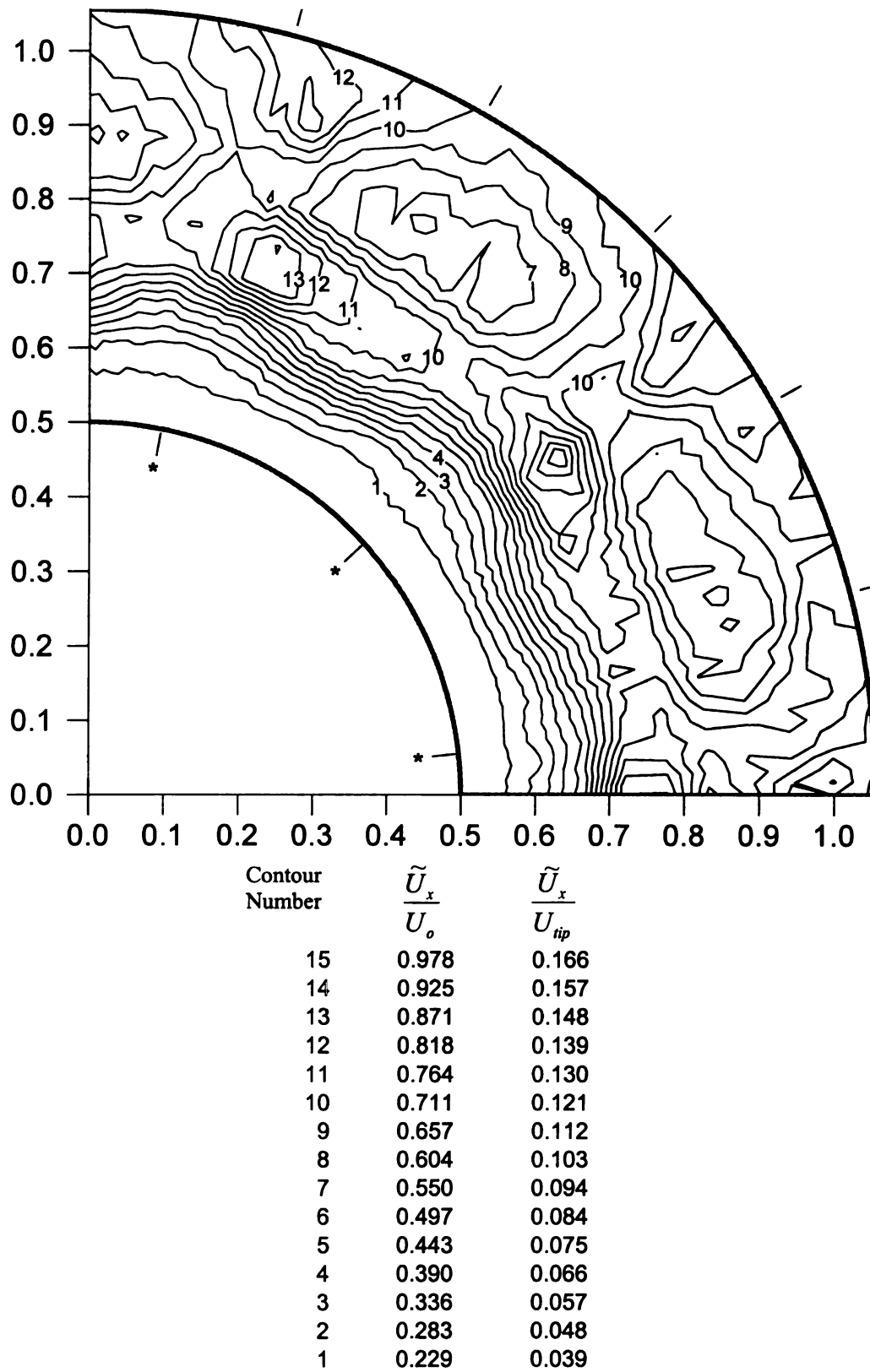
Figure 6.37 Phase averaged RMS of axial velocity for condition 'G'

Contour Number	$\dfrac{\tilde{U}_x}{U_o}$	$\dfrac{\tilde{U}_x}{U_{tip}}$
15	1.074	0.183
14	1.023	0.174
13	0.971	0.165
12	0.919	0.156
11	0.868	0.148
10	0.816	0.139
9	0.765	0.130
8	0.713	0.121
7	0.661	0.112
6	0.610	0.104
5	0.558	0.095
4	0.507	0.086
3	0.455	0.077
2	0.403	0.069
1	0.352	0.060
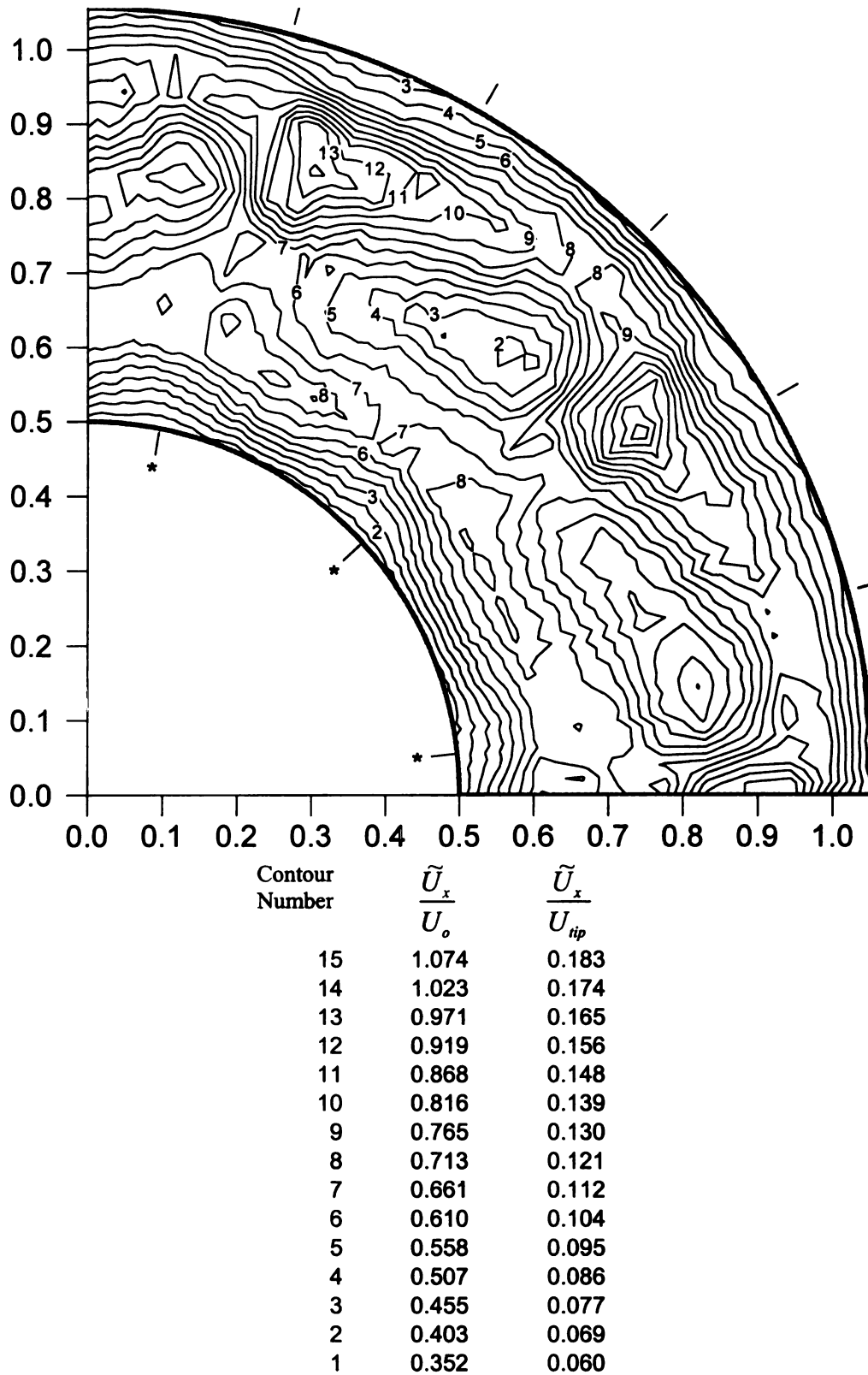
Figure 6.38 Phase averaged RMS of axial velocity for condition 'H'

Contour Number	$\dfrac{\widetilde{U}_x}{U_o}$	$\dfrac{\widetilde{U}_x}{U_{tip}}$
15	1.032	0.175
14	0.982	0.167
13	0.931	0.158
12	0.880	0.150
11	0.829	0.141
10	0.779	0.132
9	0.728	0.124
8	0.677	0.115
7	0.627	0.107
6	0.576	0.098
5	0.525	0.089
4	0.475	0.081
3	0.424	0.072
2	0.373	0.063
1	0.323	0.055
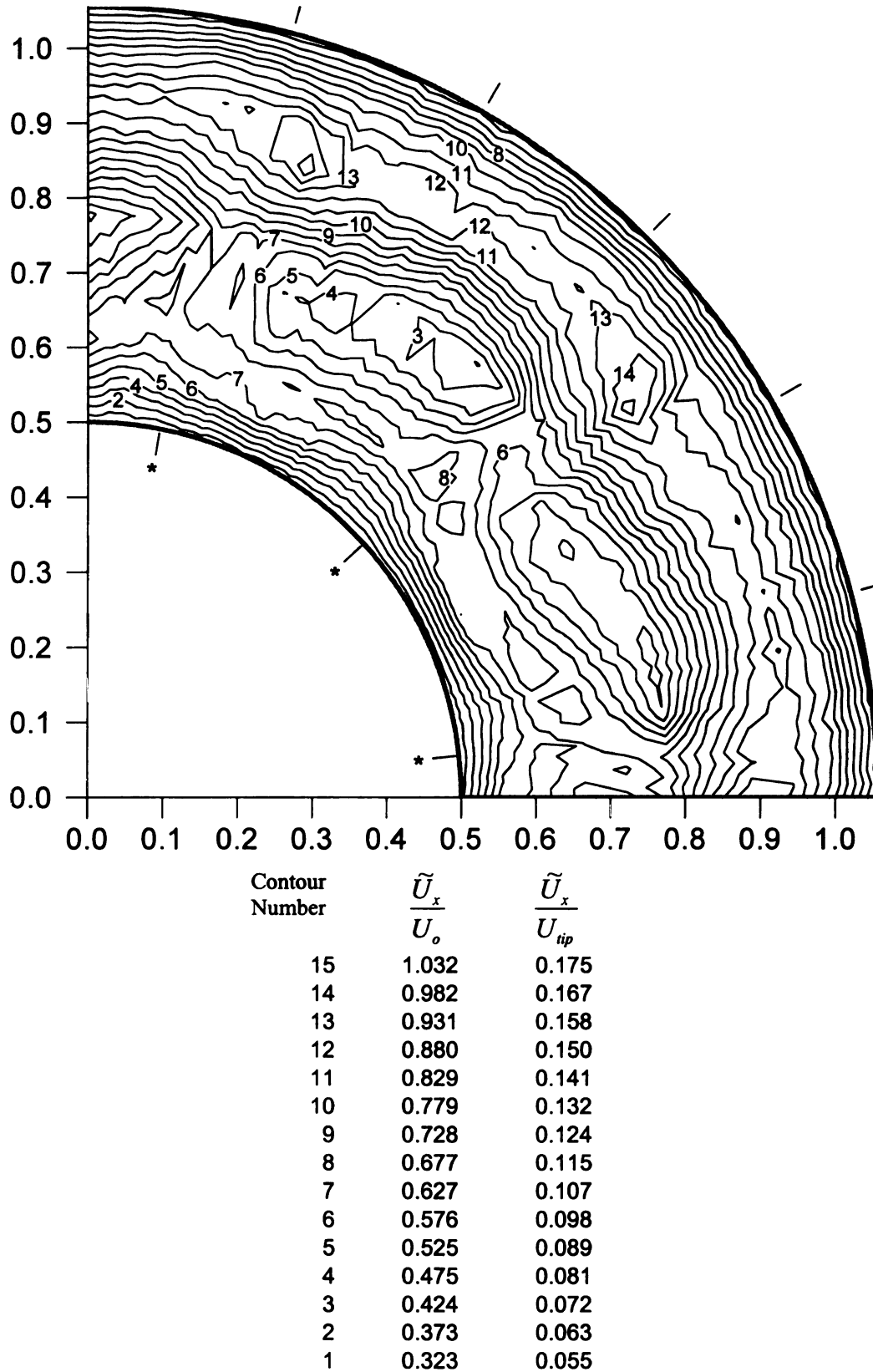
Figure 6.39 Phase averaged RMS of axial velocity for condition 'I'

Contour Number	$\dfrac{\widetilde{U}_x}{U_o}$	$\dfrac{\widetilde{U}_x}{U_{tip}}$
15	0.596	0.179
14	0.557	0.167
13	0.518	0.155
12	0.479	0.144
11	0.440	0.132
10	0.401	0.120
9	0.362	0.109
8	0.323	0.097
7	0.284	0.085
6	0.245	0.074
5	0.206	0.062
4	0.167	0.050
3	0.128	0.038
2	0.089	0.027
1	0.050	0.015
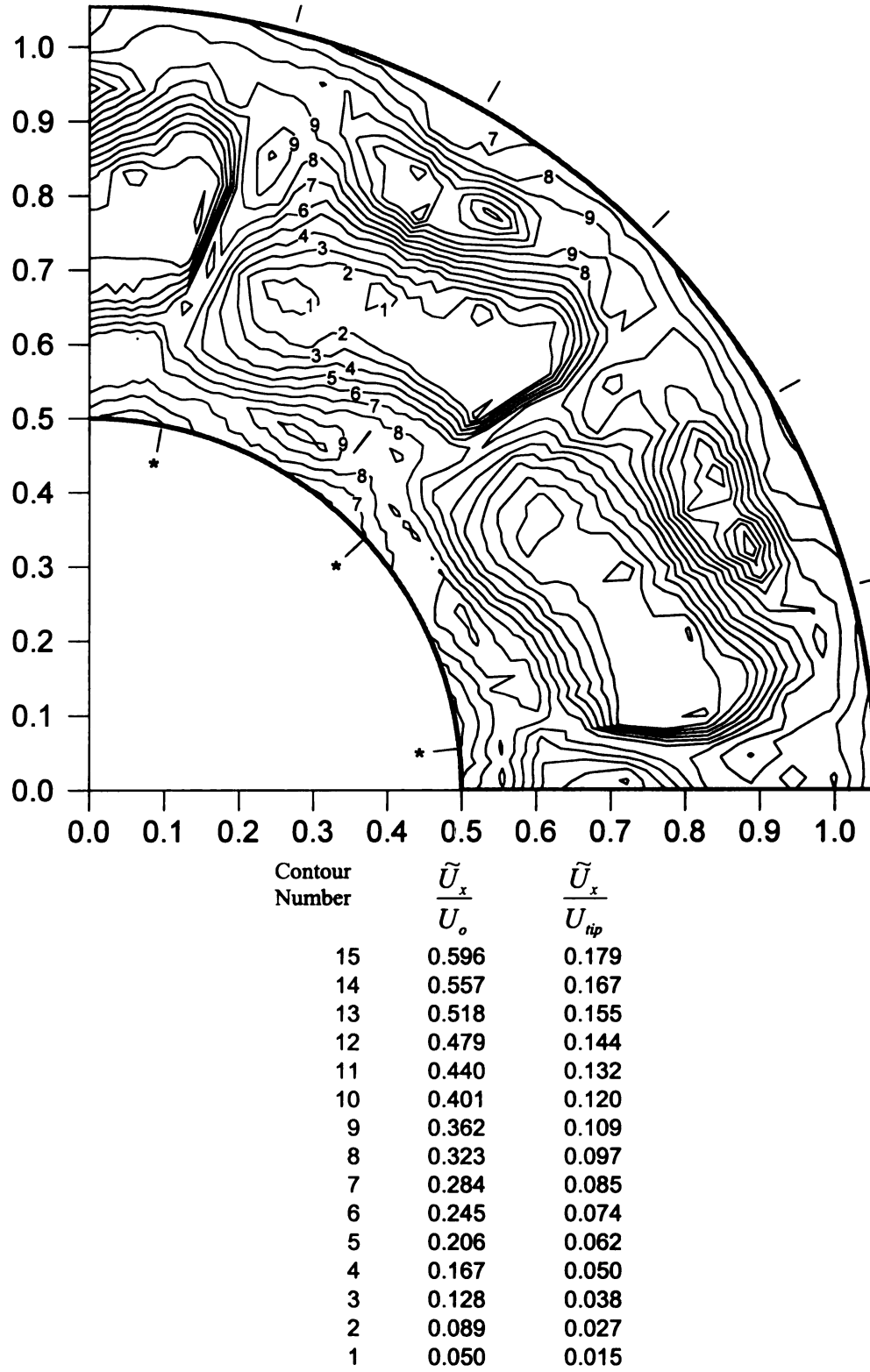
Figure 6.40 Phase averaged RMS of axial velocity for condition 'J'

Contour Number	$\dfrac{\widetilde{U}_x}{U_o}$	$\dfrac{\widetilde{U}_x}{U_{tip}}$
15	0.523	0.178
14	0.489	0.166
13	0.454	0.154
12	0.419	0.142
11	0.384	0.131
10	0.350	0.119
9	0.315	0.107
8	0.280	0.095
7	0.245	0.083
6	0.211	0.072
5	0.176	0.060
4	0.141	0.048
3	0.106	0.036
2	0.072	0.024
1	0.037	0.013
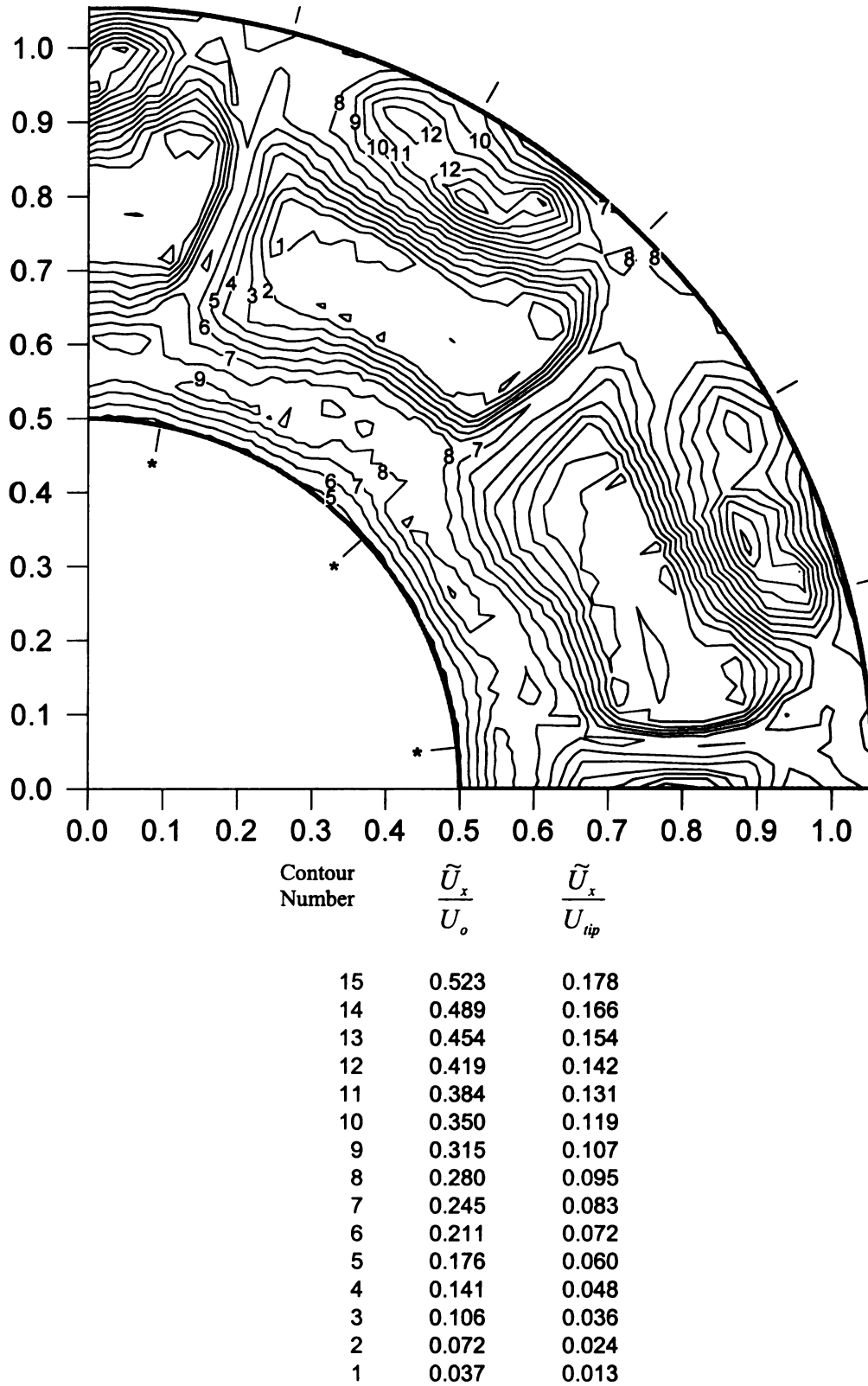
Figure 6.41 Phase averaged RMS axial velocity for condition 'K'

Contour Number	$\dfrac{\widetilde{U}_\theta}{U_o}$	$\dfrac{\widetilde{U}_\theta}{U_{tip}}$
15	1.062	0.181
14	1.012	0.172
13	0.962	0.164
12	0.912	0.155
11	0.863	0.147
10	0.813	0.138
9	0.763	0.130
8	0.713	0.121
7	0.663	0.113
6	0.614	0.104
5	0.564	0.096
4	0.514	0.087
3	0.464	0.079
2	0.414	0.070
1	0.365	0.062
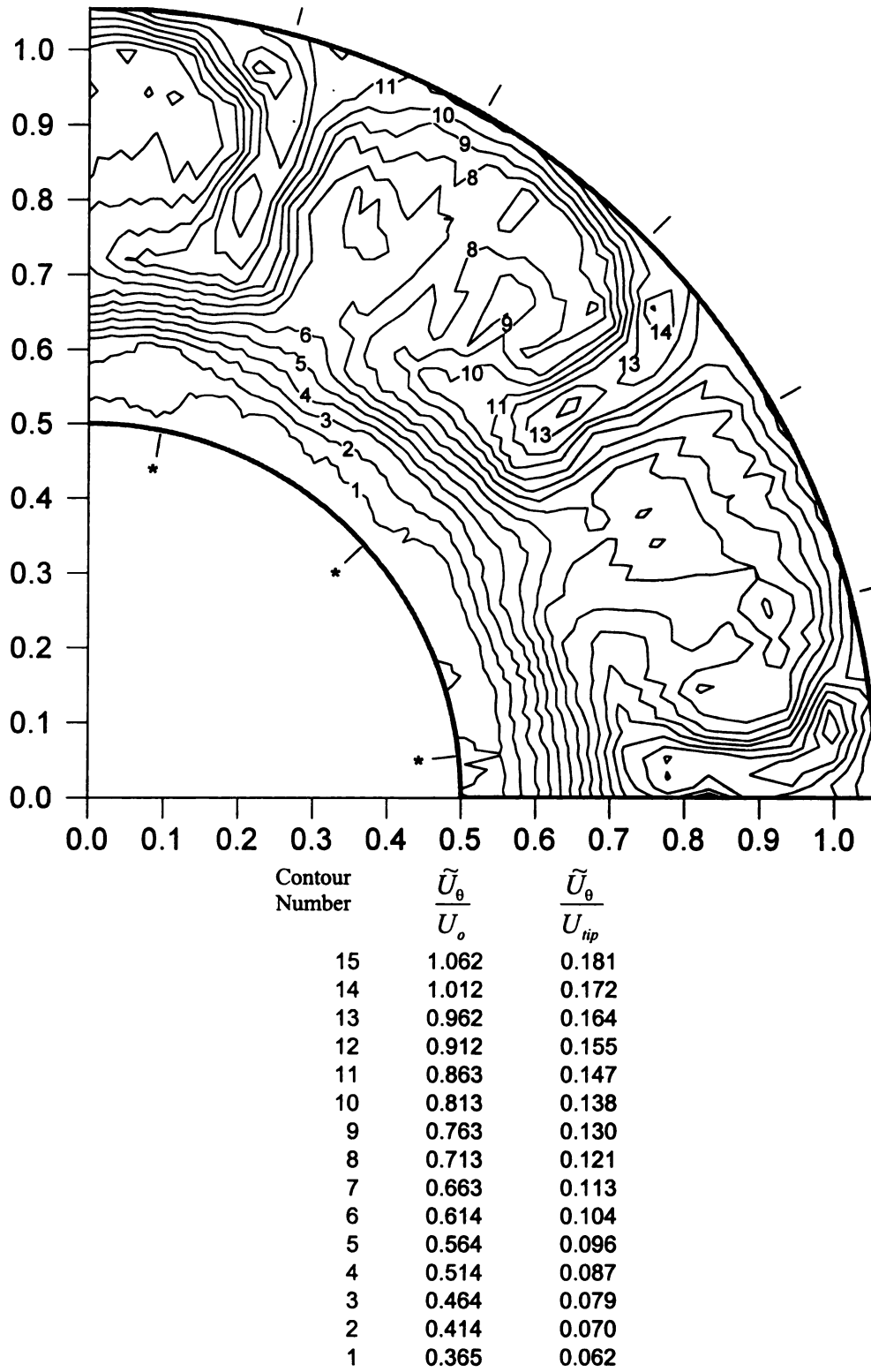
Figure 6.42 Phase averaged RMS of tangential velocity for condition 'G'

Contour Number	$\dfrac{\tilde{U}_\theta}{U_o}$	$\dfrac{\tilde{U}_\theta}{U_{tip}}$
15	1.190	0.202
14	1.143	0.194
13	1.095	0.186
12	1.048	0.178
11	1.000	0.170
10	0.953	0.162
9	0.905	0.154
8	0.857	0.146
7	0.810	0.138
6	0.762	0.130
5	0.715	0.122
4	0.667	0.113
3	0.620	0.105
2	0.572	0.097
1	0.525	0.089
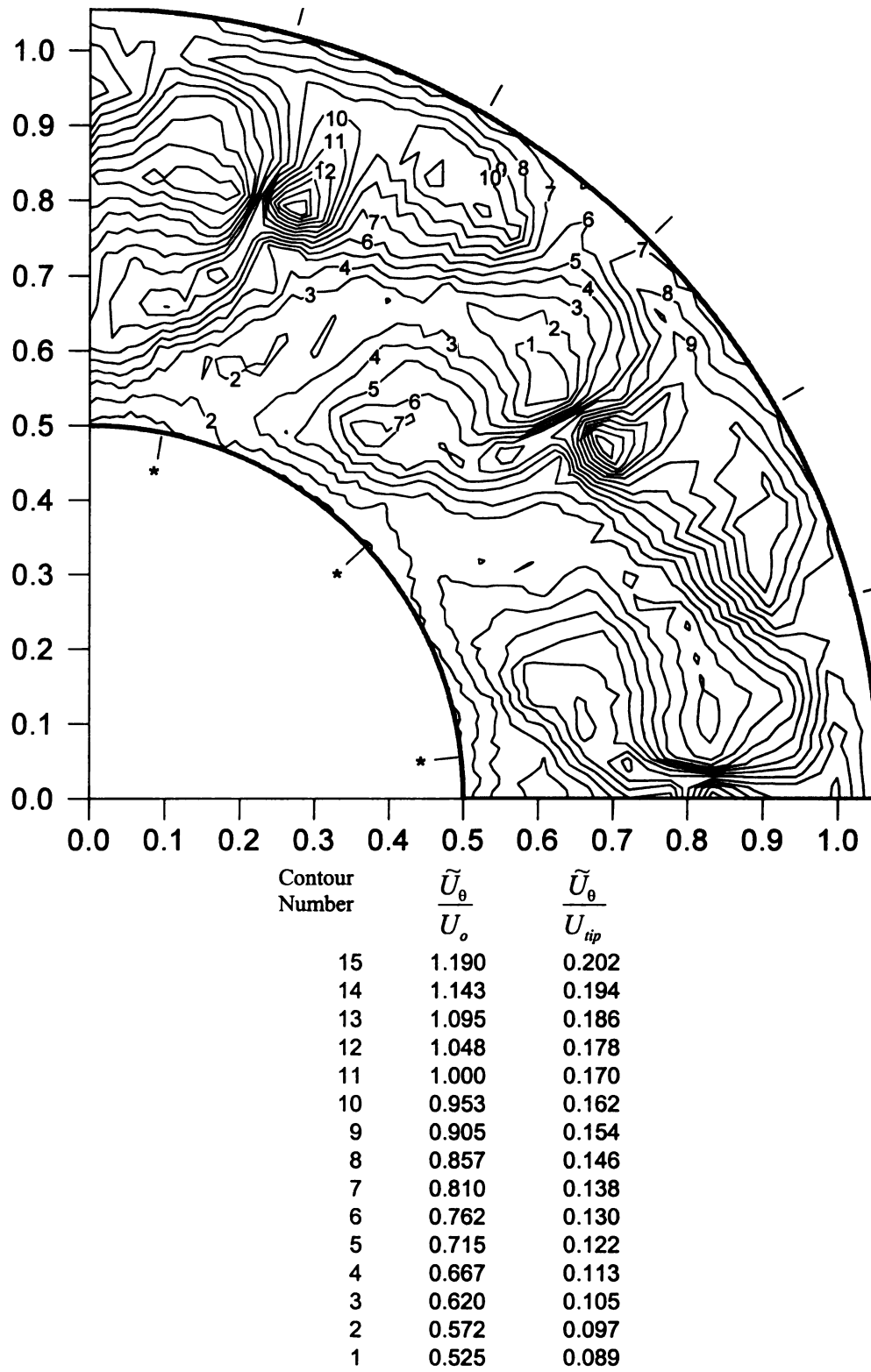
Figure 6.43 Phase averaged RMS of tangential velocity for condition 'H'

Contour Number	$\dfrac{\tilde{U}_\theta}{U_o}$	$\dfrac{\tilde{U}_\theta}{U_{tip}}$
15	1.136	0.193
14	1.084	0.184
13	1.031	0.175
12	0.979	0.166
11	0.926	0.157
10	0.874	0.149
9	0.822	0.140
8	0.769	0.131
7	0.717	0.122
6	0.665	0.113
5	0.612	0.104
4	0.560	0.095
3	0.508	0.086
2	0.455	0.077
1	0.403	0.068
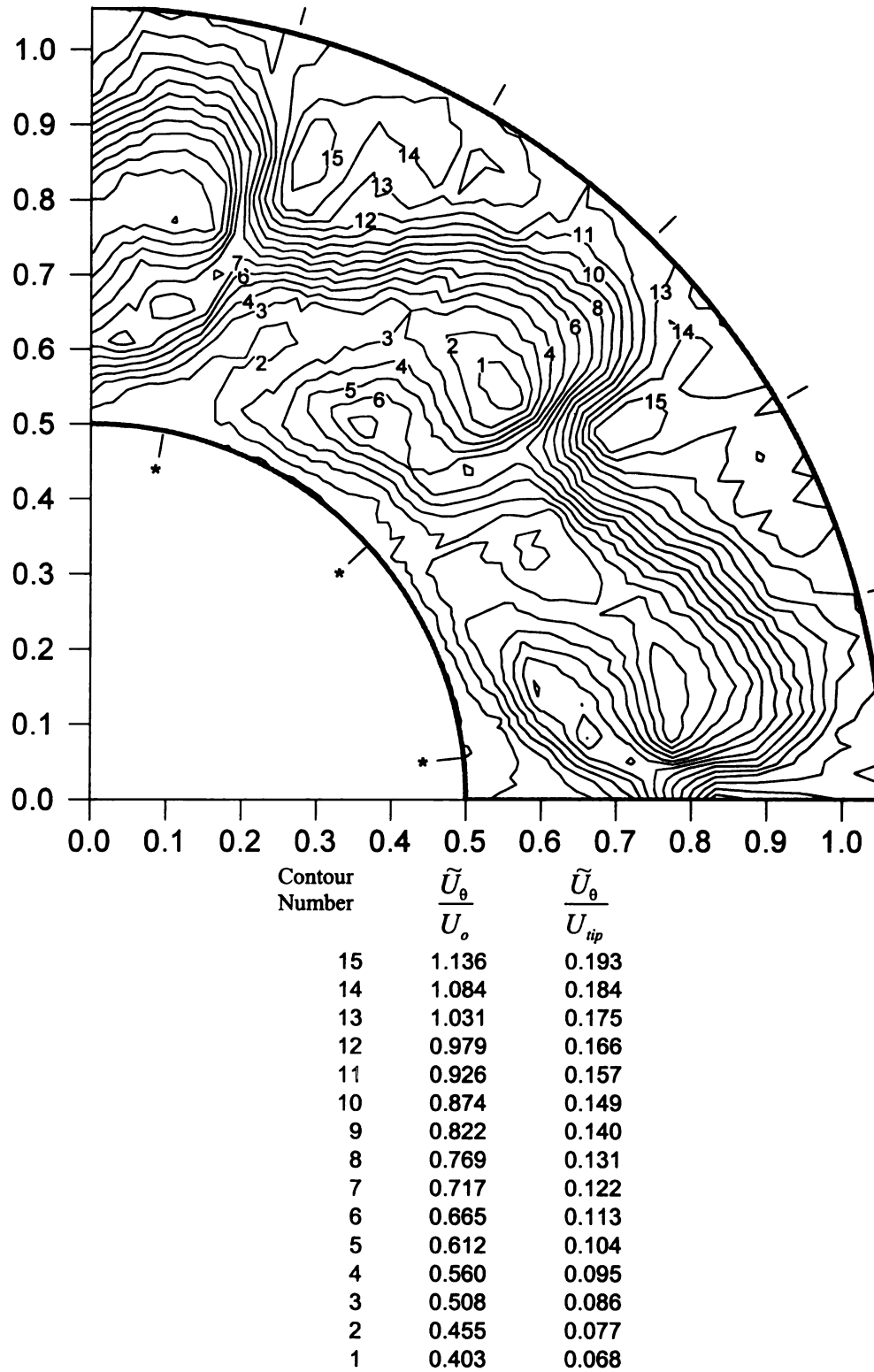
Figure 6.44 Phase averaged RMS of tangential velocity for condition 'I'

Contour Number	$\dfrac{\widetilde{U}_\theta}{U_o}$	$\dfrac{\widetilde{U}_\theta}{U_{tip}}$
15	0.597	0.179
14	0.560	0.168
13	0.524	0.157
12	0.487	0.146
11	0.451	0.135
10	0.414	0.124
9	0.377	0.113
8	0.341	0.102
7	0.304	0.091
6	0.268	0.080
5	0.231	0.069
4	0.195	0.058
3	0.158	0.047
2	0.121	0.036
1	0.085	0.025
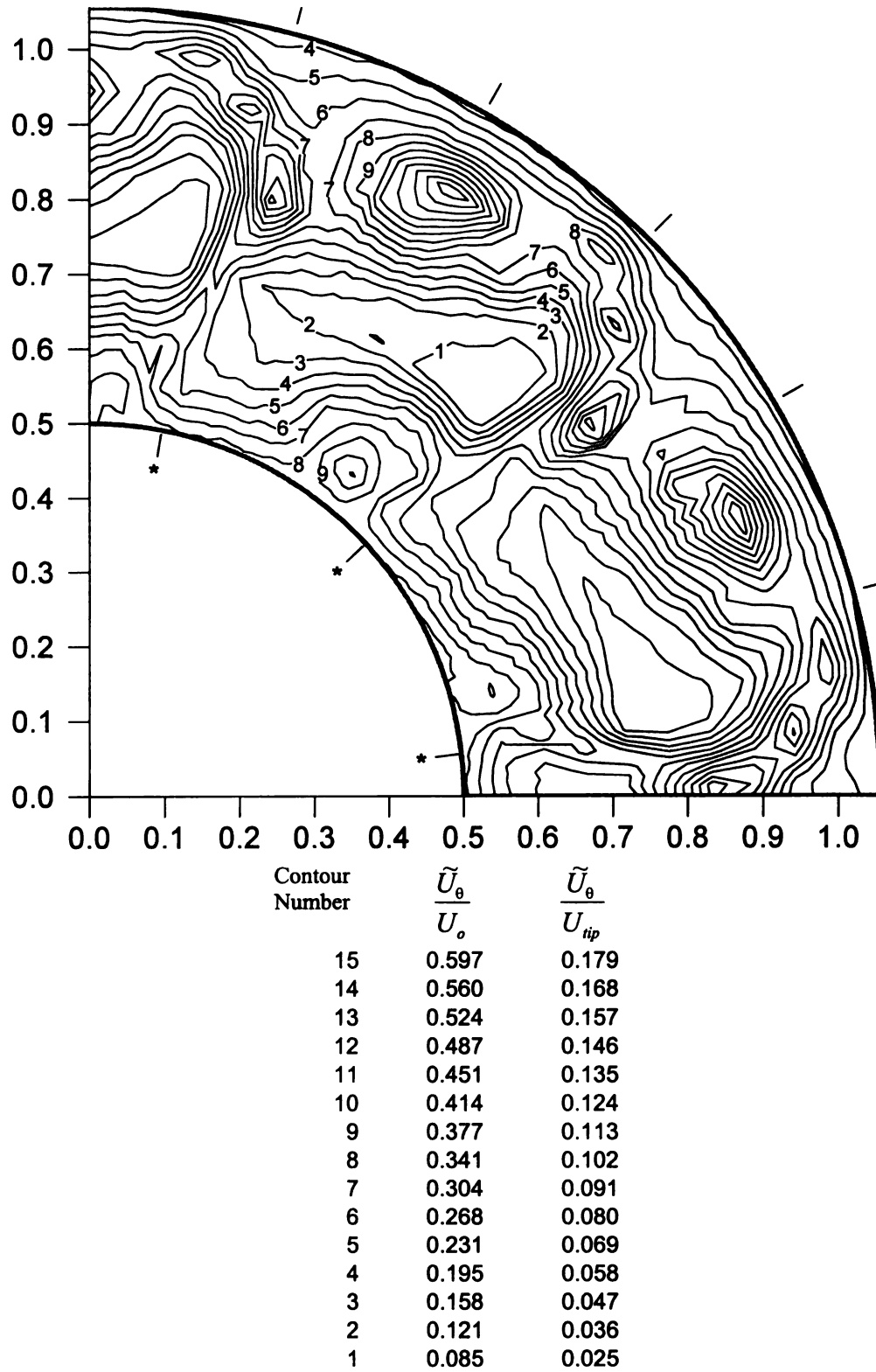
Figure 6.45 Phase averaged RMS of tangential velocity for condition 'J'

Contour Number	$\dfrac{\widetilde{U}_\theta}{U_o}$	$\dfrac{\widetilde{U}_\theta}{U_{tip}}$
15	0.405	0.138
14	0.381	0.130
13	0.358	0.122
12	0.335	0.114
11	0.311	0.106
10	0.288	0.098
9	0.264	0.090
8	0.241	0.082
7	0.217	0.074
6	0.194	0.066
5	0.171	0.058
4	0.147	0.050
3	0.124	0.042
2	0.100	0.034
1	0.077	0.026
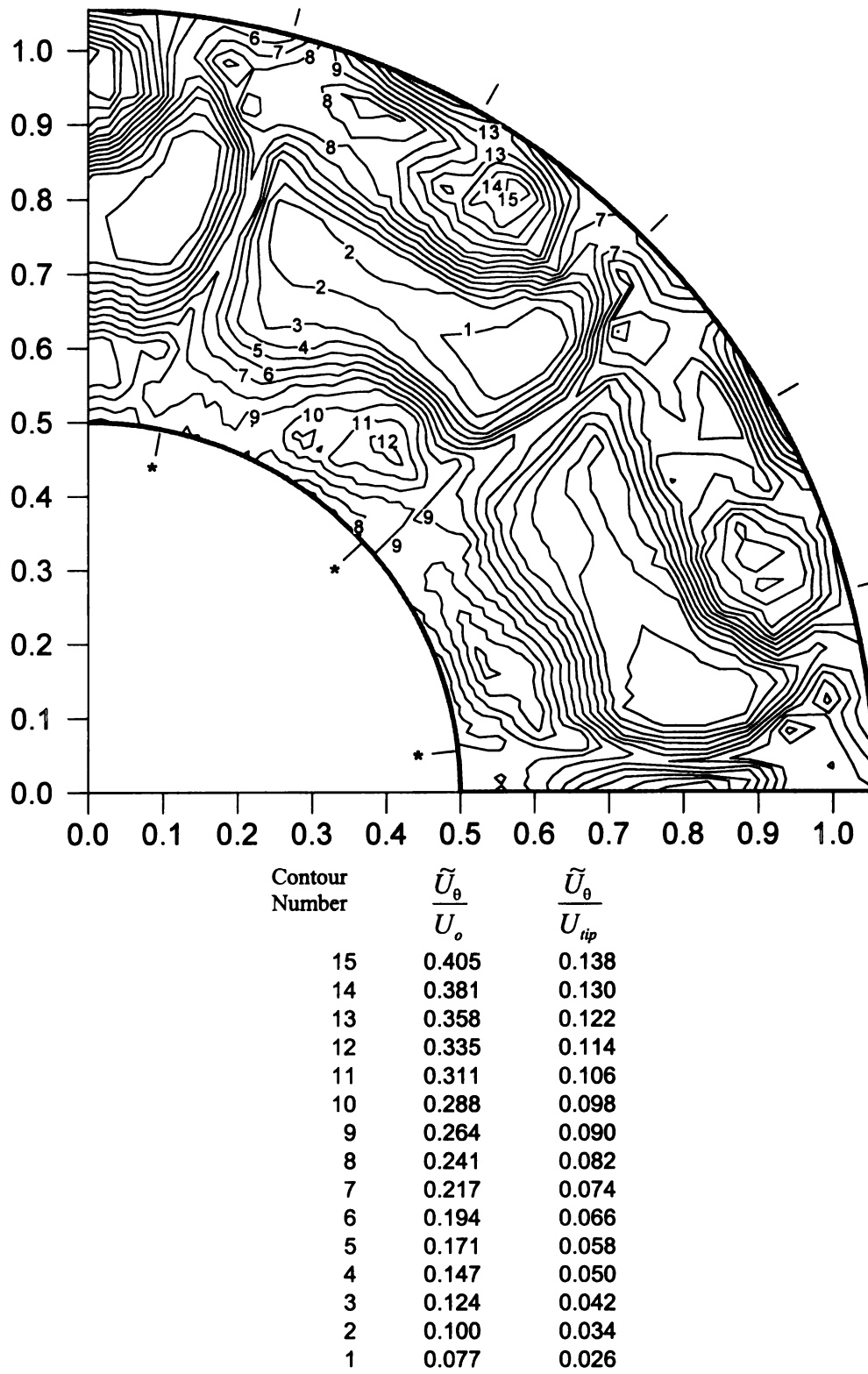
Figure 6.46 Phase averaged RMS of tangential velocity for condition 'K'

Contour Number	$\dfrac{\tilde{U}_r}{U_o}$	$\dfrac{\tilde{U}_r}{U_{tip}}$
15	0.965	0.164
14	0.911	0.155
13	0.857	0.146
12	0.803	0.137
11	0.749	0.127
10	0.695	0.118
9	0.642	0.109
8	0.588	0.100
7	0.534	0.091
6	0.480	0.082
5	0.426	0.072
4	0.373	0.063
3	0.319	0.054
2	0.265	0.045
1	0.211	0.036
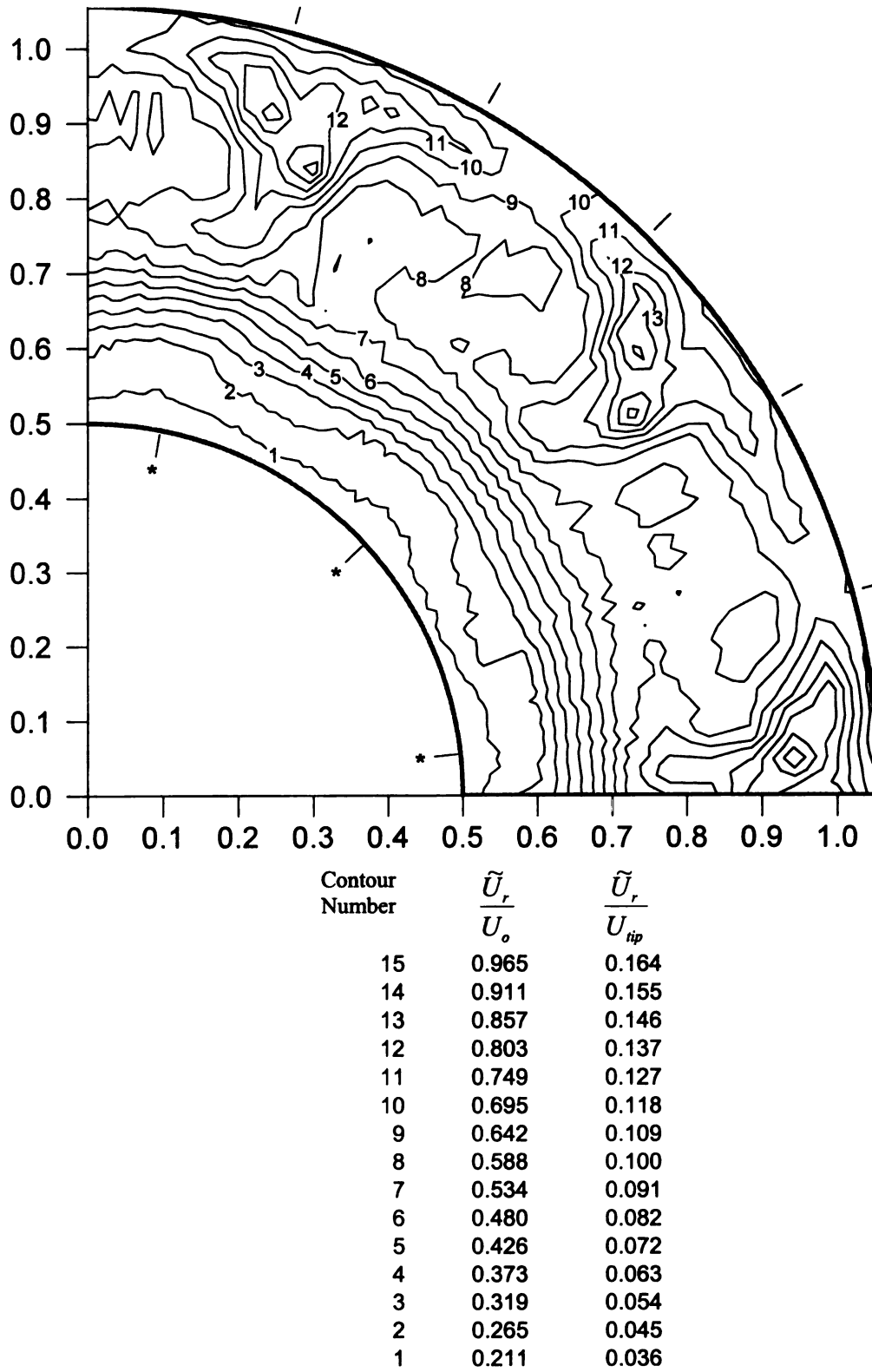
Figure 6.47 Phase averaged RMS of radial velocity for condition 'G'

Contour Number	$\dfrac{\tilde{U}_r}{U_o}$	$\dfrac{\tilde{U}_r}{U_{tip}}$
15	1.090	0.185
14	1.038	0.176
13	0.985	0.167
12	0.932	0.159
11	0.880	0.150
10	0.827	0.141
9	0.775	0.132
8	0.722	0.123
7	0.669	0.114
6	0.617	0.105
5	0.564	0.096
4	0.512	0.087
3	0.459	0.078
2	0.407	0.069
1	0.354	0.060
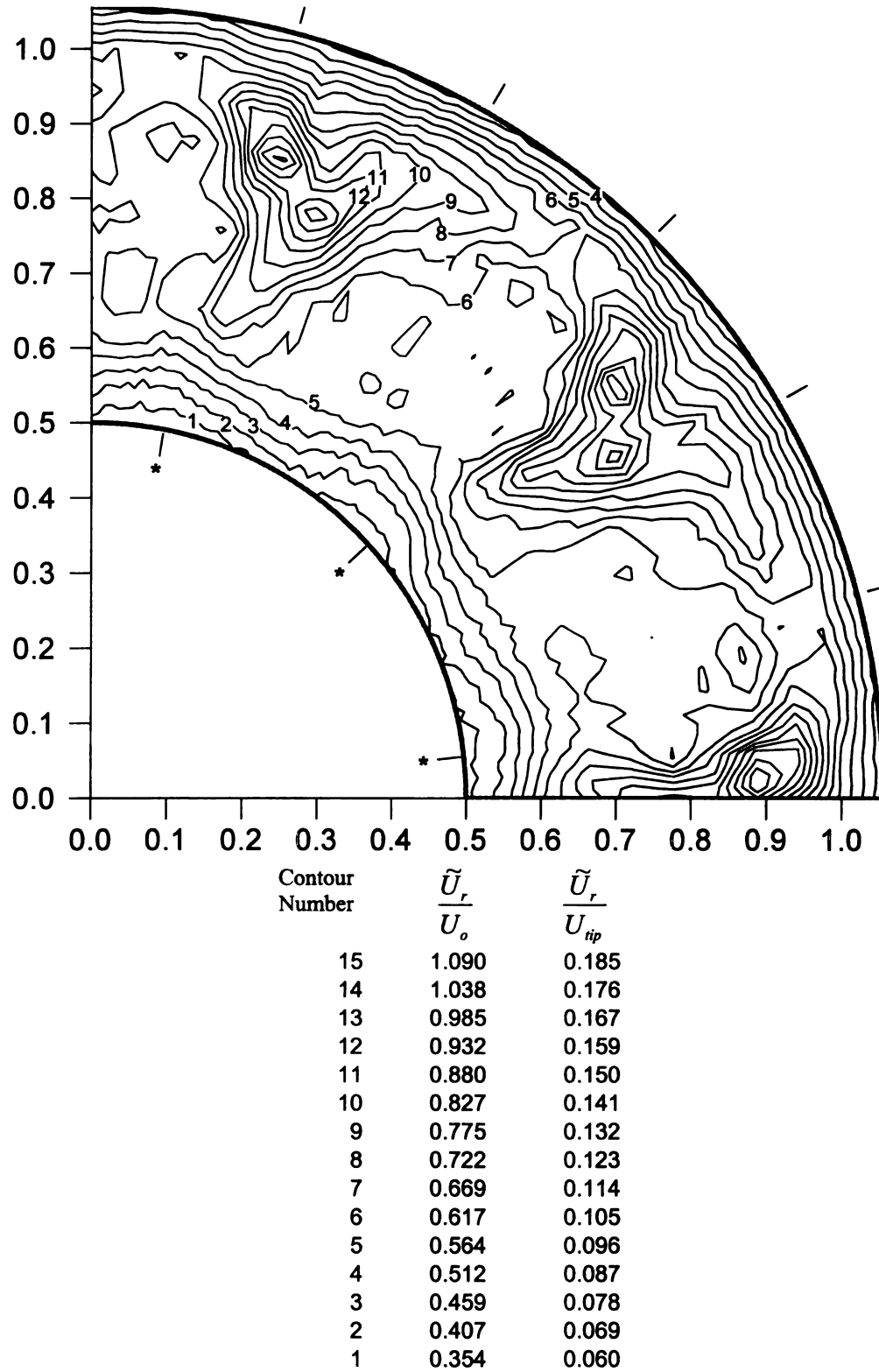
Figure 6.48 Phase averaged RMS of radial velocity for condition 'H'

Contour Number	$\dfrac{\widetilde{U}_r}{U_o}$	$\dfrac{\widetilde{U}_r}{U_{tip}}$
15	1.047	0.178
14	0.992	0.169
13	0.938	0.159
12	0.883	0.150
11	0.829	0.141
10	0.775	0.132
9	0.720	0.122
8	0.666	0.113
7	0.612	0.104
6	0.557	0.095
5	0.503	0.085
4	0.449	0.076
3	0.394	0.067
2	0.340	0.058
1	0.286	0.049
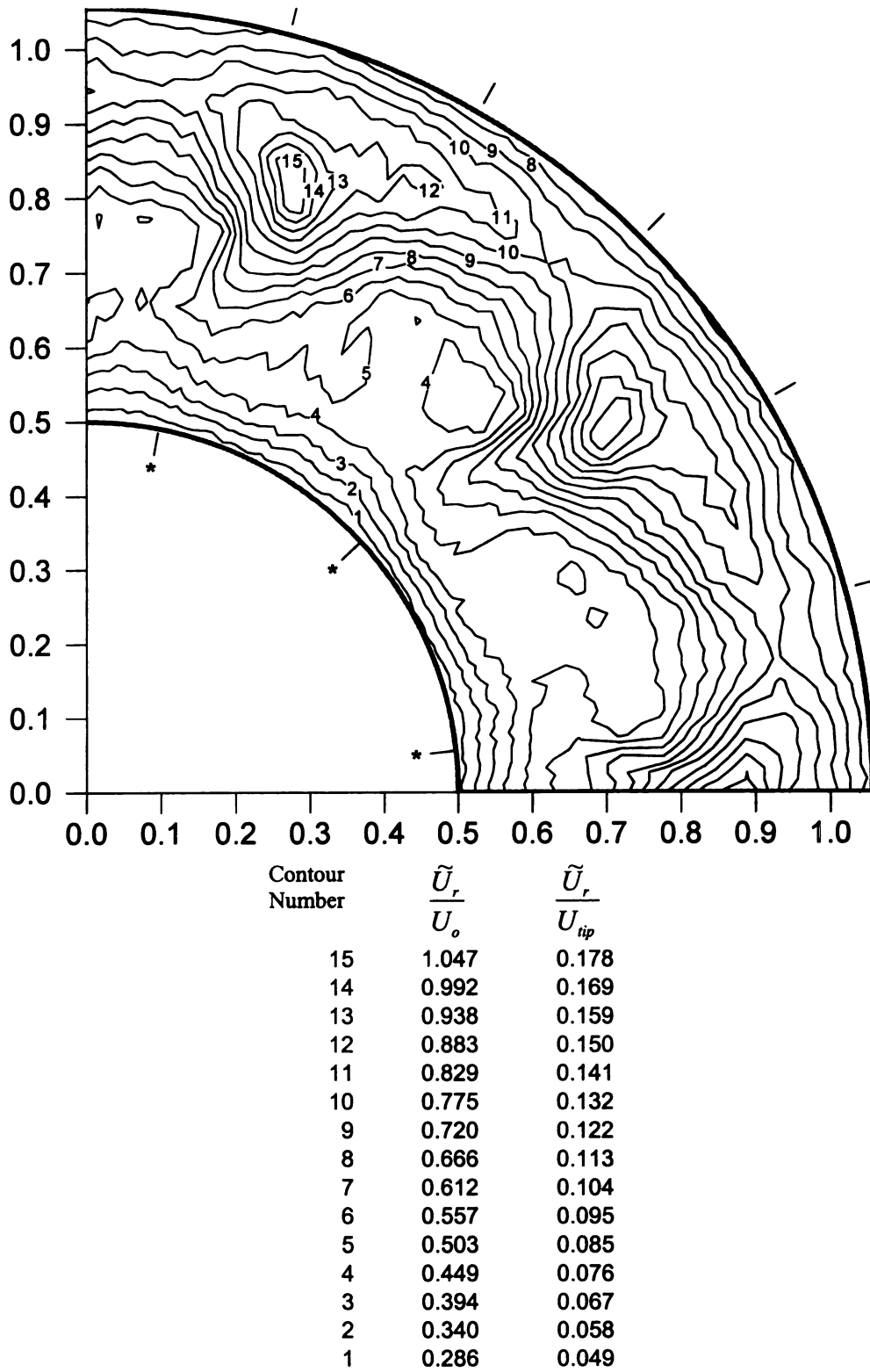
Figure 6.49 Phase averaged RMS of radial velocity for condition 'I'

Contour Number	$\dfrac{\widetilde{U}_r}{U_o}$	$\dfrac{\widetilde{U}_r}{U_{tip}}$
15	0.536	0.161
14	0.507	0.152
13	0.478	0.143
12	0.449	0.135
11	0.420	0.126
10	0.391	0.117
9	0.363	0.109
8	0.334	0.100
7	0.305	0.091
6	0.276	0.083
5	0.247	0.074
4	0.218	0.065
3	0.189	0.057
2	0.160	0.048
1	0.131	0.039
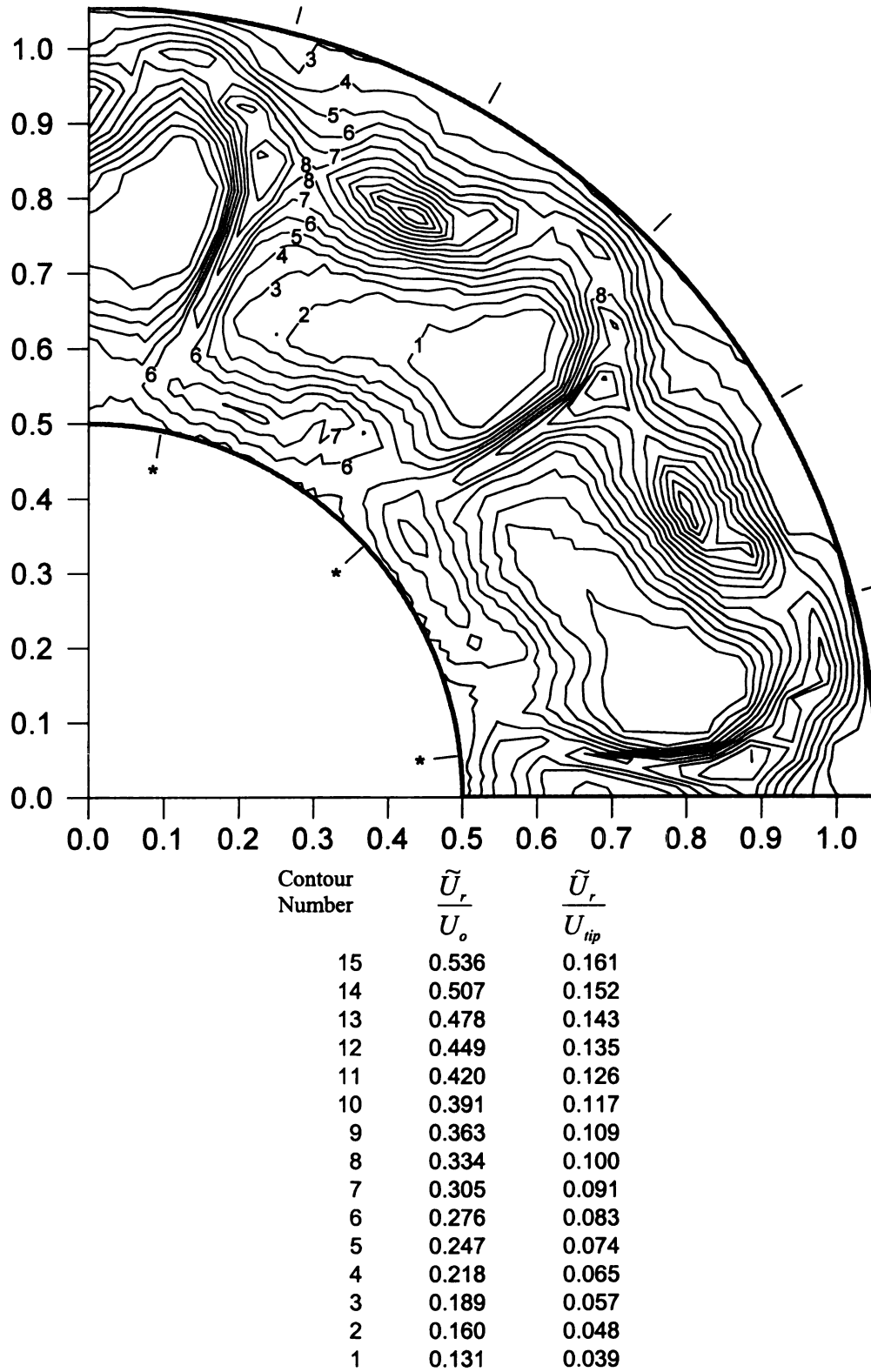
Figure 6.50 Phase averaged RMS of radial velocity for condition 'J'

Contour Number	$\dfrac{\tilde{U}_r}{U_o}$	$\dfrac{\tilde{U}_r}{U_{tip}}$
15	0.491	0.167
14	0.465	0.158
13	0.438	0.149
12	0.412	0.140
11	0.385	0.131
10	0.359	0.122
9	0.332	0.113
8	0.306	0.104
7	0.279	0.095
6	0.253	0.086
5	0.226	0.077
4	0.200	0.068
3	0.173	0.059
2	0.147	0.050
1	0.120	0.041
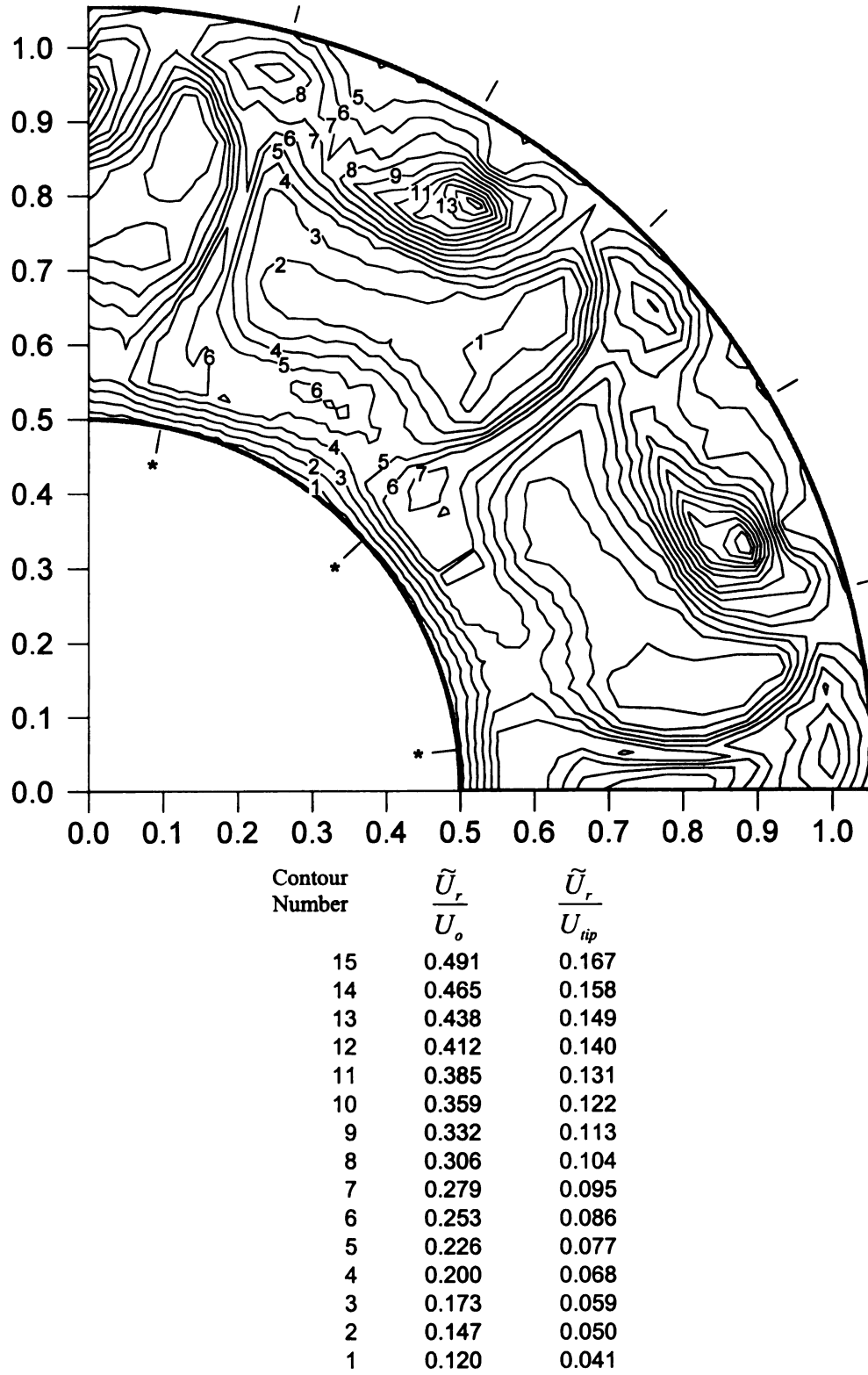
Figure 6.51 Phase averaged RMS of radial velocity for condition 'K'
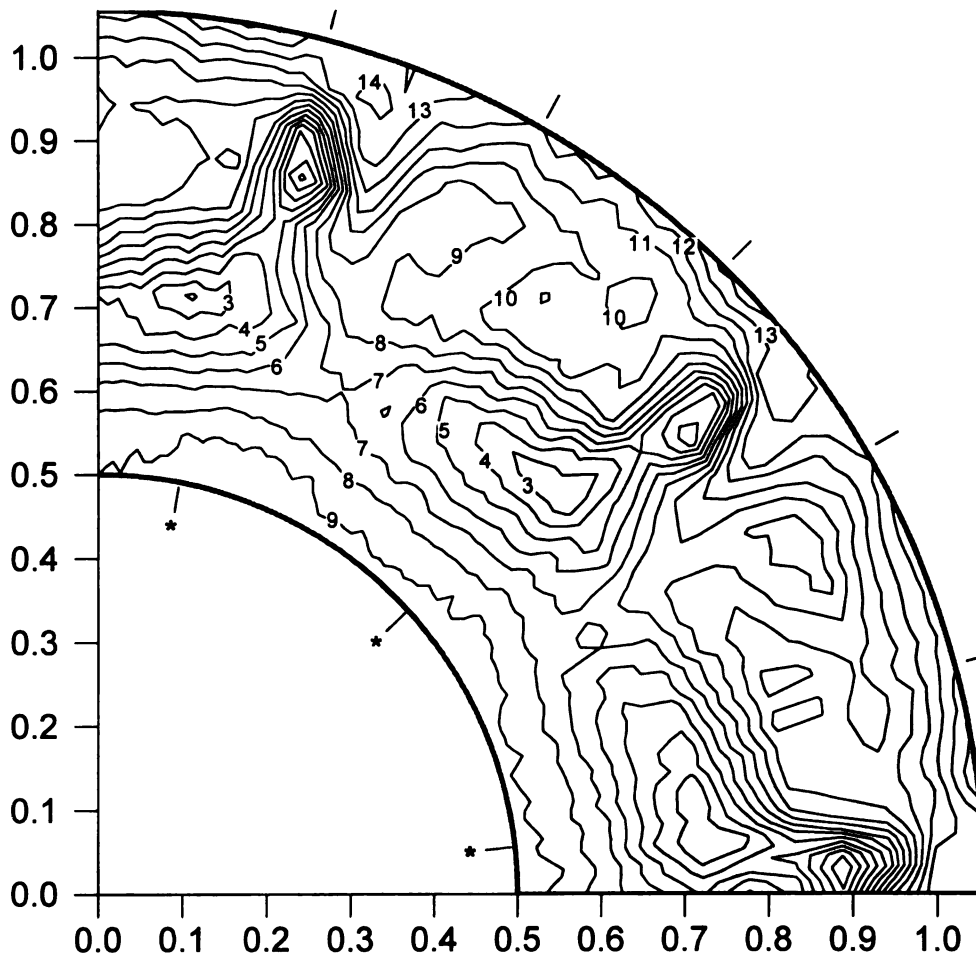
Contour Number	$\dfrac{\overline{\omega}_x}{2\Omega_{fan}}$
15	1.89
14	1.51
13	1.14
12	0.760
11	0.377
10	0.000
9	-0.377
8	-0.760
7	-1.14
6	-1.51
5	-1.89
4	-2.27
3	-2.65
2	-3.03
1	-3.41

Figure 6.52 Phase averaged axial vorticity for condition 'G'

Contour Number	$\dfrac{\overline{\omega}_x}{2\Omega_{fan}}$
15	2.36
14	1.73
13	1.10
12	0.471
11	-0.157
10	-0.785
9	-1.41
8	-2.04
7	-2.67
6	-3.30
5	-3.93
4	-4.56
3	-5.19
2	-5.82
1	-6.45
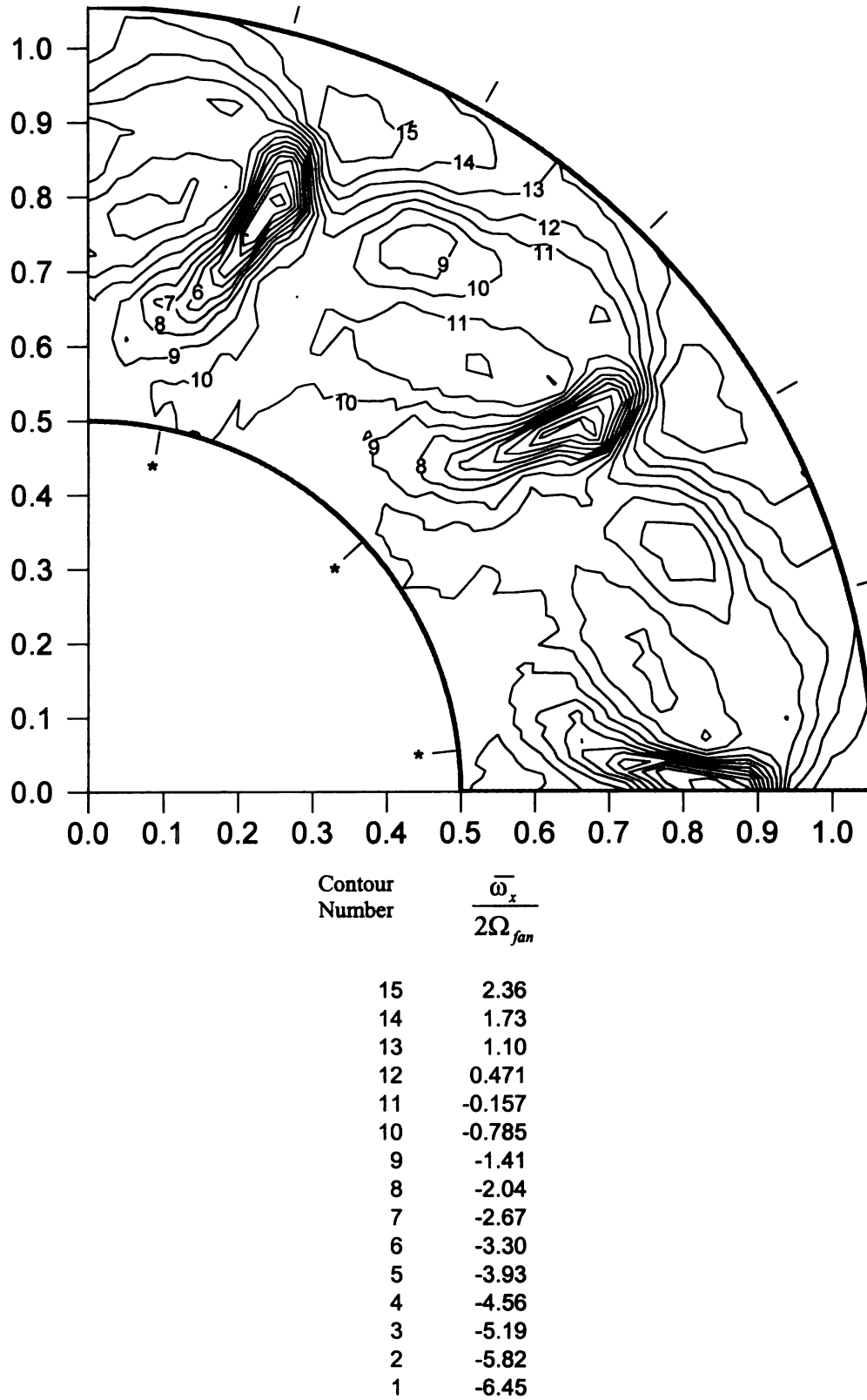
Figure 6.53 Phase averaged axial vorticity for condition 'H'

Contour Number	$\dfrac{\overline{\omega}_x}{2\Omega_{fan}}$
15	0.835
14	0.465
13	0.100
12	-0.270
11	-0.634
10	-0.999
9	-1.37
8	-1.73
7	-2.10
6	-2.47
5	-2.83
4	-3.20
3	-3.57
2	-3.94
1	-4.30
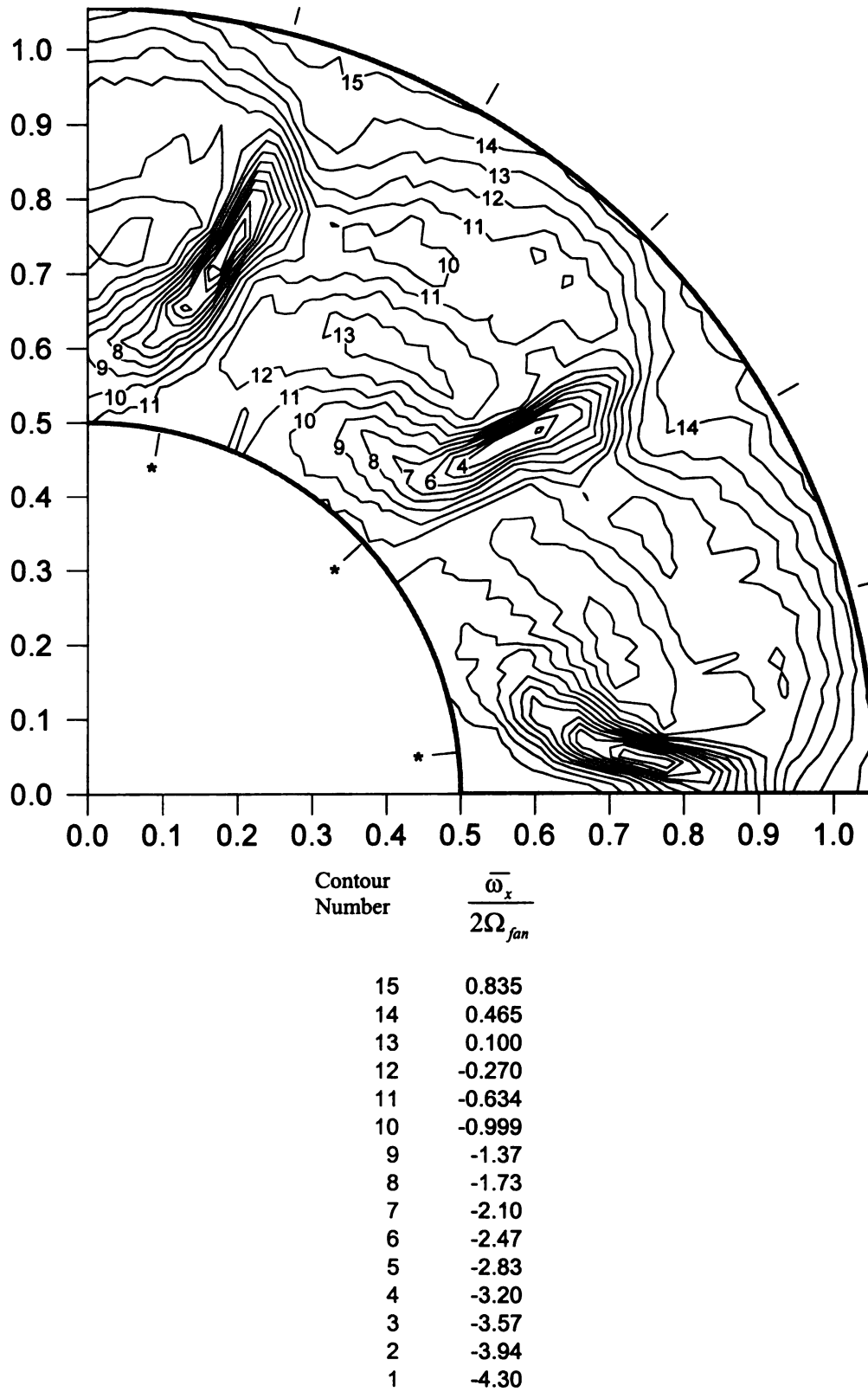
Figure 6.54 Phase averaged axial vorticity for condition 'I'

Contour Number	$\dfrac{\overline{\omega}_x}{2\Omega_{fan}}$
15	2.02
14	1.60
13	1.18
12	0.754
11	0.333
10	-0.088
9	-0.509
8	-0.930
7	-1.36
6	-1.78
5	-2.20
4	-2.62
3	-3.04
2	-3.28
1	-3.89
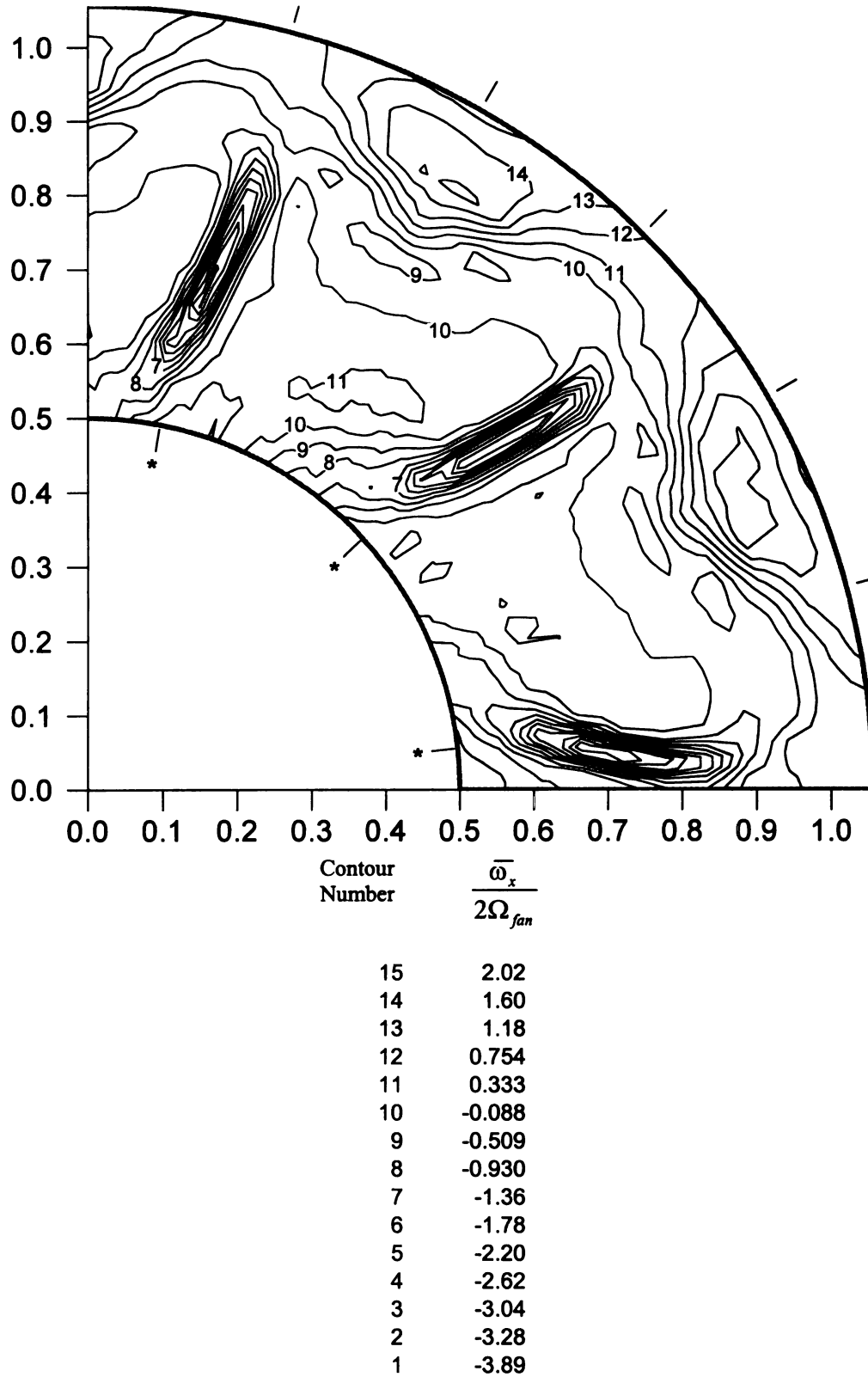
Figure 6.55 Phase averaged axial vorticity for condition 'J'
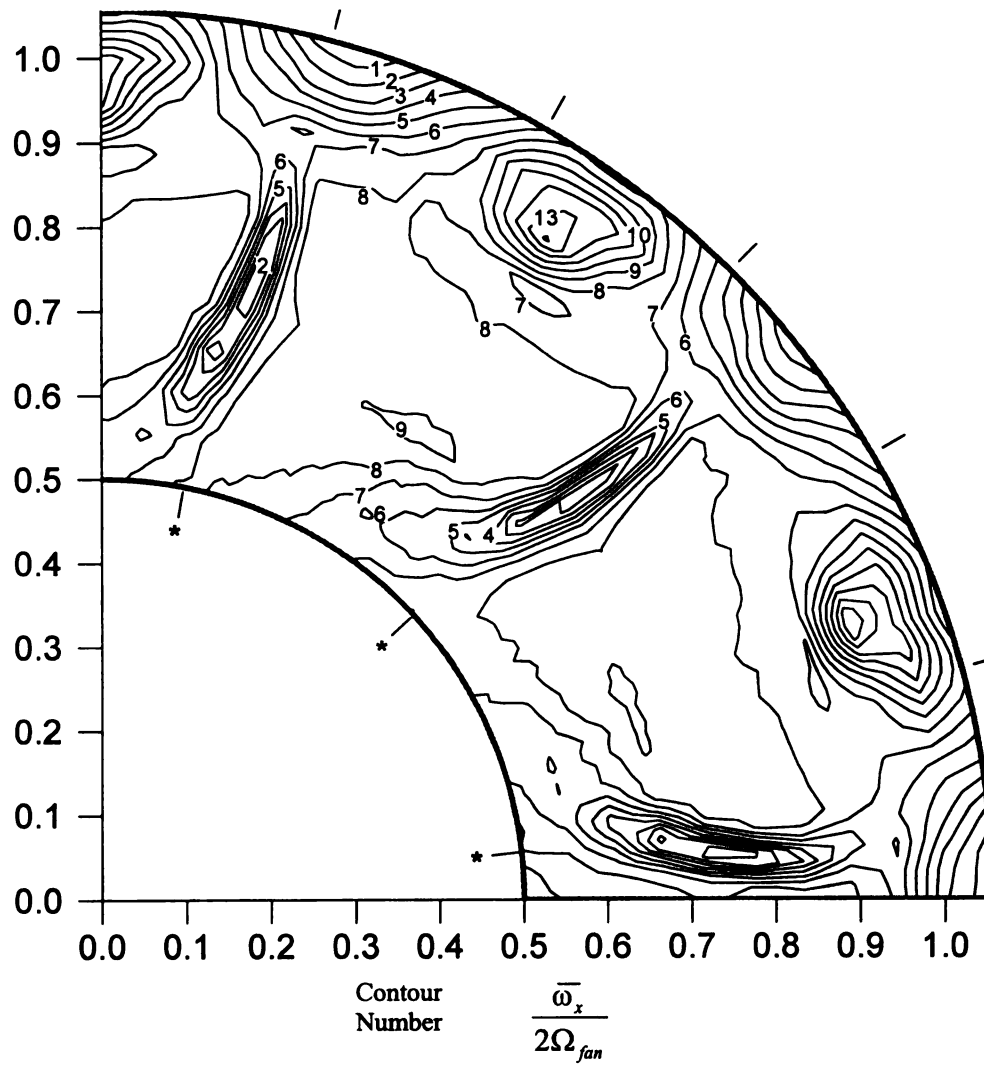
Contour Number	$\dfrac{\overline{\omega}_x}{2\Omega_{fan}}$
15	2.59
14	2.21
13	1.82
12	1.43
11	1.05
10	0.666
9	0.283
8	-0.100
7	-0.483
6	-0.867
5	-1.25
4	-1.64
3	-2.02
2	-2.41
1	-2.79

Figure 6.56 Phase averaged axial vorticity for condition 'K'

7. CONCLUSIONS AND VIABILITY PREDICTIONS

The ACFRD facility was constructed in 1994 for the study of automotive cooling fans. The experimental equipment and measurement techniques described in Chapter 4 have been developed to aid in the understanding of the fluid mechanical attributes of fan flows. In addition to this thesis, the data acquired using the ACFRD facility have aided the Ford Motor Company in the validation of computational models of underhood cooling systems.

The aerodynamic shroud was conceived in September 1994 by Professor John Foss of Michigan State University. To the best of the author's knowledge, the use of an annular jet to aid in the efficiency of fan flows is new and original. A prototype shroud was assembled, and performance data were acquired. The ability of equation (5-2) and (5-3) to represent the functional dependence of the data indicate that for a given geometry both the system performance and efficiency depend only on the flow rate through the fan, and the power input into the shroud.

The system efficiency will clearly depend on the design of the shroud delivery system. Specifically, losses in the prime mover and ducting system which provides the aerodynamic shroud with pressurized air will result in lower system efficiency. The losses in the shroud ducting will be proportional to the square of the air velocity. The aerodynamic shroud should be designed with a relatively small gap height such that a relatively low flow rate (i.e., low V^2) and high pressure can be used to obtain an equivalent shroud power (χ). A prime mover should then be selected which operates efficiently in a high pressure rise - low volume flow rate environment.

The performance and efficiency data were presented in Chapter 5. The results show enhanced performance and higher flow rates, and degraded performance at lower flow rates. The ability of the aerodynamic shroud to enhance the efficiency of an automobile cooling system greatly depends on the system resistance (i.e., the operating point is the intersection of the performance curve with a parabola which defines the system resistance). This resistance is typically created by the presence of the grill, air conditioning condenser, radiator, and downstream blockage elements such as the engine. The data show that a large system resistance would cause the aerodynamic shroud to lessen the efficiency, whereas a smaller system resistance would allow the aerodynamic shroud to increase the system efficiency.

A 1994 Ford Explorer was investigated to obtain an understanding of the flow field in an actual vehicle. The vehicle was loaned to Michigan State University for a brief period. As a result very little quantitative were was acquired. However, tuft visualizations were used to gain a general understanding of the flow field in the underhood compartment. The author estimates that the cooling fan operates in the range $0.10<\phi<0.17$ at the idle condition. This estimate is based on qualitative comparison of the flow field observed in the underhood compartment using a tuft with results shown in Chapter 6. It is difficult to determine if the aerodynamic shroud will increase or decrease the performance based on this information and the data presented in Chapter 5. It is encouraging to note however, that the idle condition represents the "worst case" operating condition. A "ram air" effect caused by the relative motion of the air with respect to a moving vehicle will increase the ϕ value of the operating condition. Additionally, many vehicles exist which are expected to have much less resistance to the cooling air flow.

For example, the larger engine compartments found in the heavy truck industry might be more suitable for the aerodynamic shroud.

For the experiments presented in this thesis a single design was selected for the prototype aerodynamic shroud. Future work in this area should concentrate on geometrical optimization of the fan and shroud. The data reported on the velocity field indicate that the strong positive radial flow at the tip of the fan at low flow rates is causing interacting with the axial Coanda jet and decreasing the system efficiency. It is believed that a proper system design which considers both the fan and shroud geometry may significantly increase the efficacy of the aerodynamic shroud.

In conclusion, the data acquired show the aerodynamic shroud to be a concept which clearly has potential for automotive, as well as other applications. The data presented should be used to understand the flow field created by the fan/shroud combination. Continued work should be directed toward the optimization of the system in conjunction with the application environment.

REFERENCES

Adamczyk, J., Celestina, M., Greitzer, E., "The Role of Tip Clearance in High-Speed Fan Stall," Journal of Turbomachinery, Vol. 115, January 1993.

Ameri, M., and Dybbs, A., "Theoretical Modeling of Coanda Ejectors," ASME FED-Vol. 163, Fluid Machinery, 1993

Anderson, D., Tannehill, J., Pletcher, R., Computational Fluid Mechanics and Heat Transfer, Hemisphere Publishing Corp., New York, 1984.

Baranski, B., "Designing the Engine Cooling Fan," SAE #740691, 1997

Bohl, D., "An Experimental Study of the Near Field Region of a Free Jet With Passive Mixing Tabs," M.S. Thesis, Dept. of Mechanical Engineering, Michigan State University, 1996.

Dring, R., Joslyn, H., Hardin, L., "An Investigation of Axial Compressor Rotor Aerodynamics," Journal of Engineering for Power, Vol. 104, January 1982.

El-Taher, R., "Experimental Investigation of Curvature Effects on Ventilated Wall Jets," AIAA Journal, Vol 21, No 11 November 1983.

Foss, J., Wallace, J., Wark, C., "Vorticity Measurements," Instrumentation for Fluid Dynamics, Joseph Schetz and Allen Fuhs ed., Wiley and Sons, Inc., pp.1066-1067, 1995.

Hirsch, C., and Kool, P., "Measurement of the Three-Dimensional Flow Field Behind an Axial Compressor Stage," Journal of Engineering for Power, April 1977, p168

Inoue, M., Kumoumaru, M., Fukuhara, M., "Behavior of Tip Leakage Flow Behind an Axial Compressor Rotor," Journal of Engineering for Power, Vol. 108, January 1986.

Inoue, M., Kuroumaru, M., "Three Dimensional Structure and Decay of Vorticies Behind an Axial Flow Rotating Blade Row," Journal of Engineering for Power, Vol. 106, July 1984.

Kuroumaru, M., Inque M., Higaki, T.,"Measurement of Three Dimensional Flow Field behind an Impeller by Means of Periodic Multo-sampling with a Slanted Hot Wire," Bulletin of the JSME, Vol. 25, No. 209, November 1982.

Lakshminarauana, B., "Techniques for Aerodynamic and Turbulence Measurements in Turbomachinery Rotors," Journal of Engineering for Power, Vol. 103, April 1981.

Lakshminarayana, B., "Methods of Predicting the Tip Clearance Effects in Axial Flow Turbomachinery," Journal of Basic Engineering, September 1970.

Lakshminarayana, B., Fluid Mechanics and Heat Transfer in Turbomachinery, John Wiley and Sons, 1996.

Shakouchi, T., Onohara, Y., and Kato, S., "Analysis of a Two-Dimensional, Turbulent Wall Jet Along a Circular Cylinder," JSME Inernational Journal Volume32 No 3, p332, 1989.

Storer, J., Cumpsty, N., "An Approximate Analysis and Prediction Method for Tip Clearance Loss in Axial Compressors," Journal of Turbomachinery, Vol. 116, October 1994.

Van Houten, R., Hickey, R., Kobayashi, S., "Fan Wake Measurements By Five-Hole Yaw Tube and Laser Anemometer," Airflow Research and Manufacturing Corporation, Document 160, September 1993.

Wilson, D., and Goldsteinm, R., "Turbulent Wall Jets With Cylindrical Streamwise Surface Curvature," Journal of Fluids Engineering, September 1976.

Appendix A Coanda Jet Velocity Measurements

A single hot wire was used to acquire velocity measurements in the axisymmetric Coanda jet with the cooling fan removed. This was executed prior to the measurements presented in Chapters 5 and 6. The purpose of the experiment was to provide the author with a general understanding of the boundary conditions imposed on the fan by the aerodynamic shroud. It should be noted that the measured velocity field would likely be greatly altered by the presence of the rotating fan.

Time series voltages from a single anemometer output were acquired for 10 seconds at 5,000 hz. These data were converted to velocities by the modified Collis and Williams equation as discussed in Chpater 4. These data were acquired at a single streamwise location of x/g=98, where x is the curvlinear distance from the jet exit, and g is the width of the jet exit. A value of g=1.0mm was used for the data presented. The resultant value of x=98mm corresponds to the inlet plane of the fan blades. Four values for $P_{plenum}-P_{atm}$ (82, 351, 543, and 817 Pa) were used to characterize the jet. The velocities derived from this presure reading were used to scale the velocity values.

The profiles for the mean and RMS of velocity are shown in Figure A.1. All four test conditions indicate that the Coanda jet is attached at this streamwise location. The thickness of the wall jet ($y=y(u=0.5u_{max})$) for all tested conditions is less than the fan tip clearance of 25mm. It is interesting to note that the profile corresponding to the lowest plenum pressure is significantly different in shape compared to the three higher values. It is believed that this is a result of turbulent transition of the boundary layers the jet contraction at larger shroud pressure.
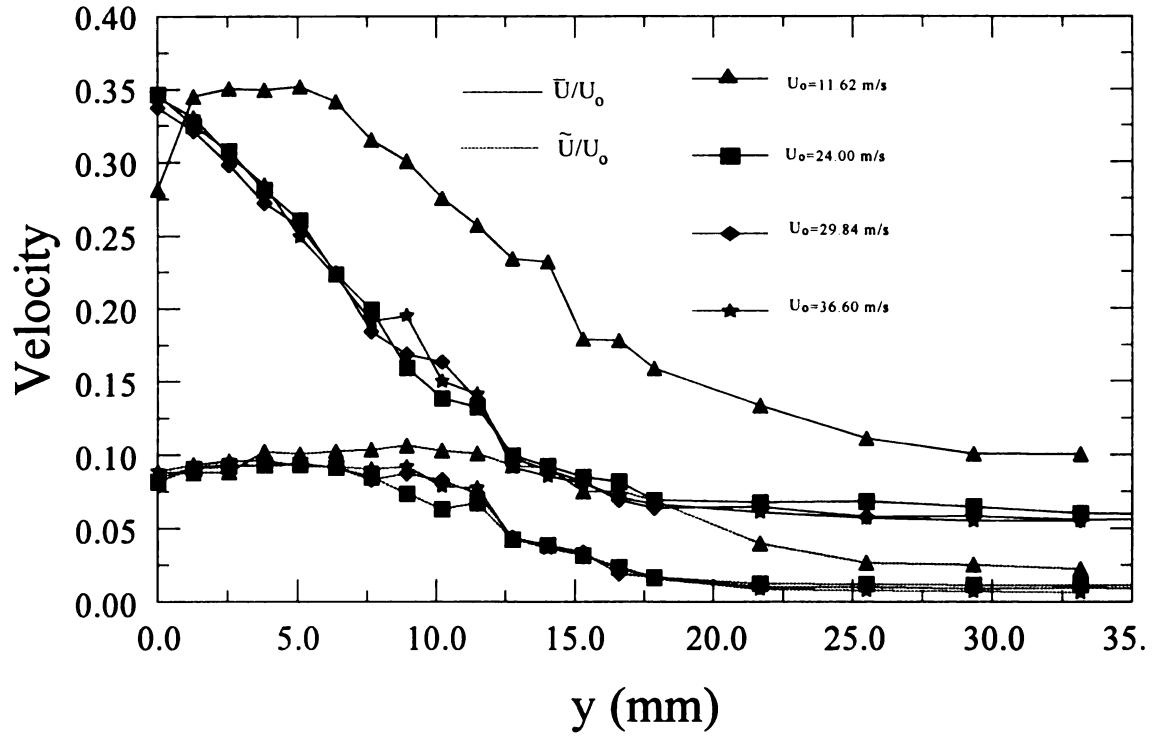
Figure A1 Mean and RMS velocity profiles for x=98mm (x/g=98)

Appendix B   Phase Averaged Kinetic Energy

The kinetic energy of the flow was calculated from the mean velocity values presented in Chapter 6. This quantity was felt to be of interest to those who might consider modeling or simulating this type of flow field numericaly. The time averaged kinetic energy was calculated from

$$\overline{KE}(x,r,\theta) = \left(\overline{U}_x^2 + \overline{U}_r^2 + \overline{U}_\theta^2\right)\!\big/2 . \tag{B-1}$$

Figures B.1 and B.2 represent the data calculated from B-1 scaled by U_{tip} and U_o respectively. The phase averaged kinetic energy was calculated from

$$< \overline{KE} > (x,r,\theta,\alpha) = \left(< \overline{U}_x >^2 + < \overline{U}_r >^2 + < \overline{U}_\theta >^2\right)\!\big/2 \tag{B-2}$$

where the brackets <> represent a phase averaged quantity. These data are shown in Figures B3 through B7 for conditions 'G' through 'K', as described in Chapter 6.
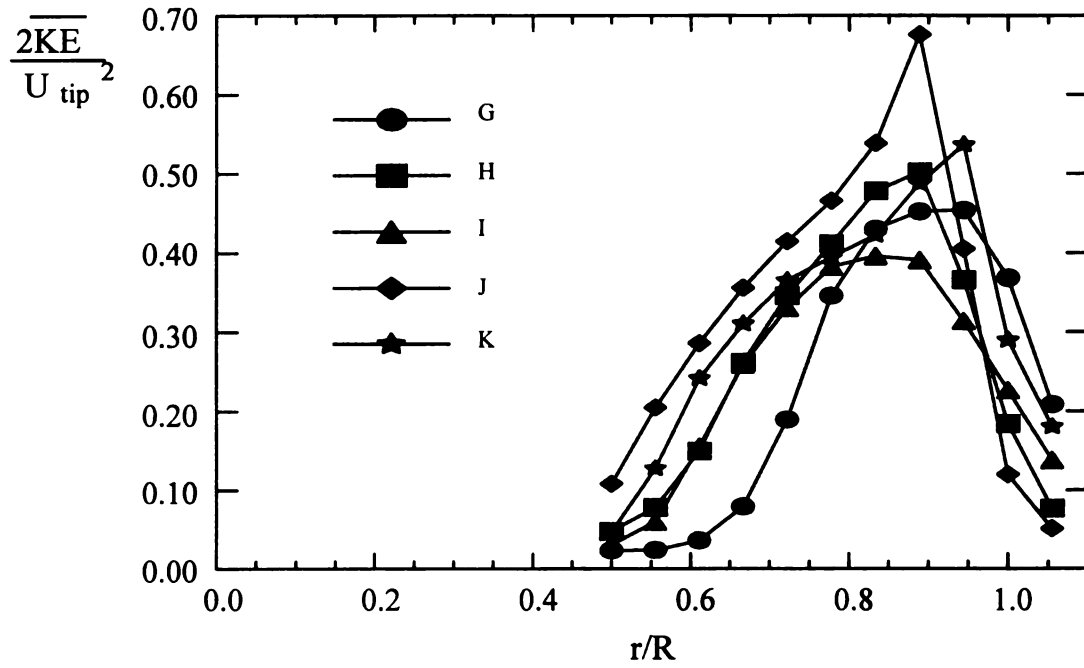
Figure B.1 Time averaged kinetic energy normalized by U_{tip}
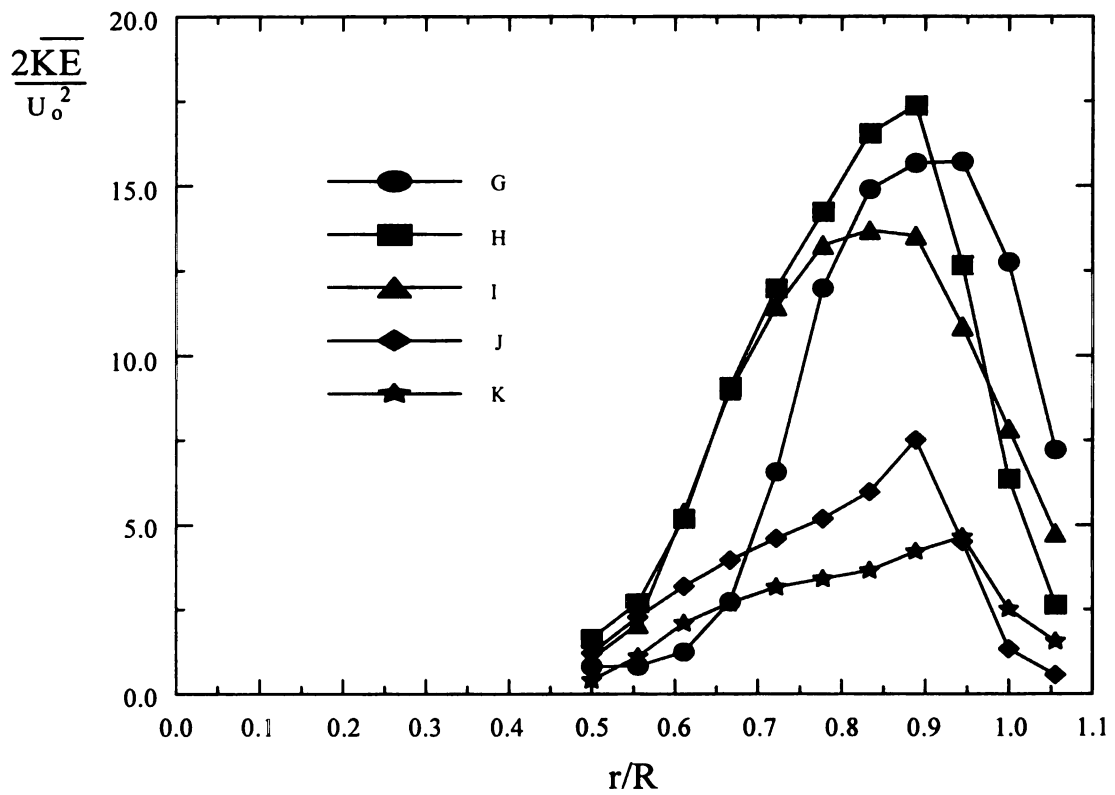
Figure B.2 Time averaged kinetic energy normalized by U_o
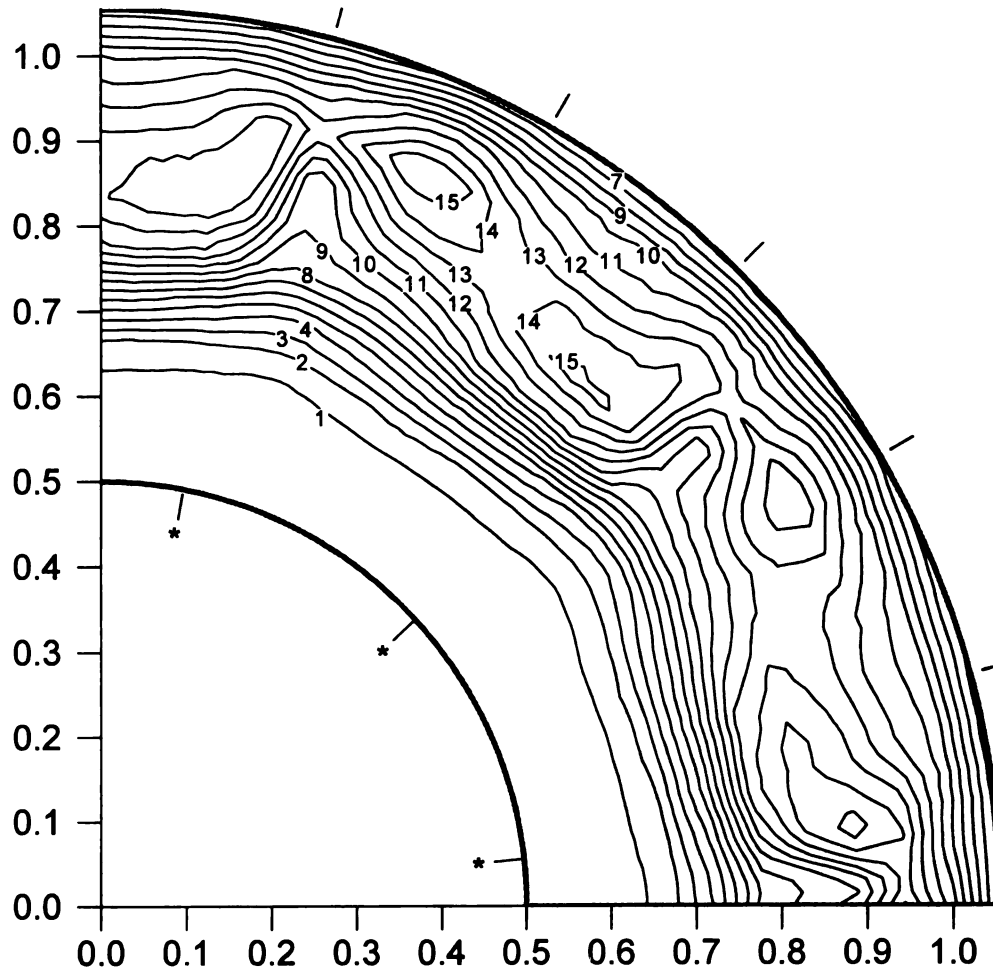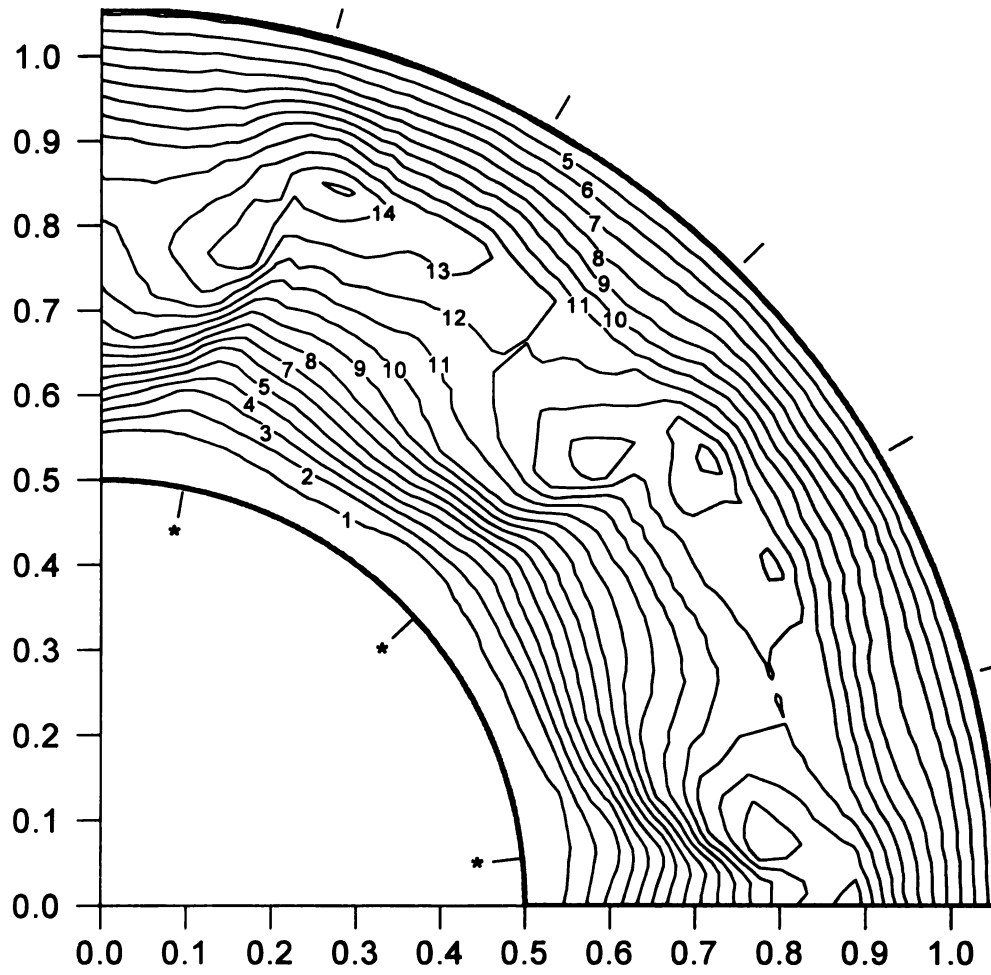
Contour Number	$\dfrac{2KE}{U_o^2}$	$\dfrac{2KE}{U_{tip}^2}$
15	18.2	0.52
14	17.0	0.49
13	15.8	0.46
12	14.7	0.42
11	13.5	0.39
10	12.3	0.36
9	11.2	0.32
8	10.0	0.29
7	8.8	0.26
6	7.7	0.22
5	6.5	0.19
4	5.3	0.15
3	4.2	0.12
2	3.0	0.09
1	1.8	0.05

Figure B.3 Phase averaged kinetic energy for condition 'G'
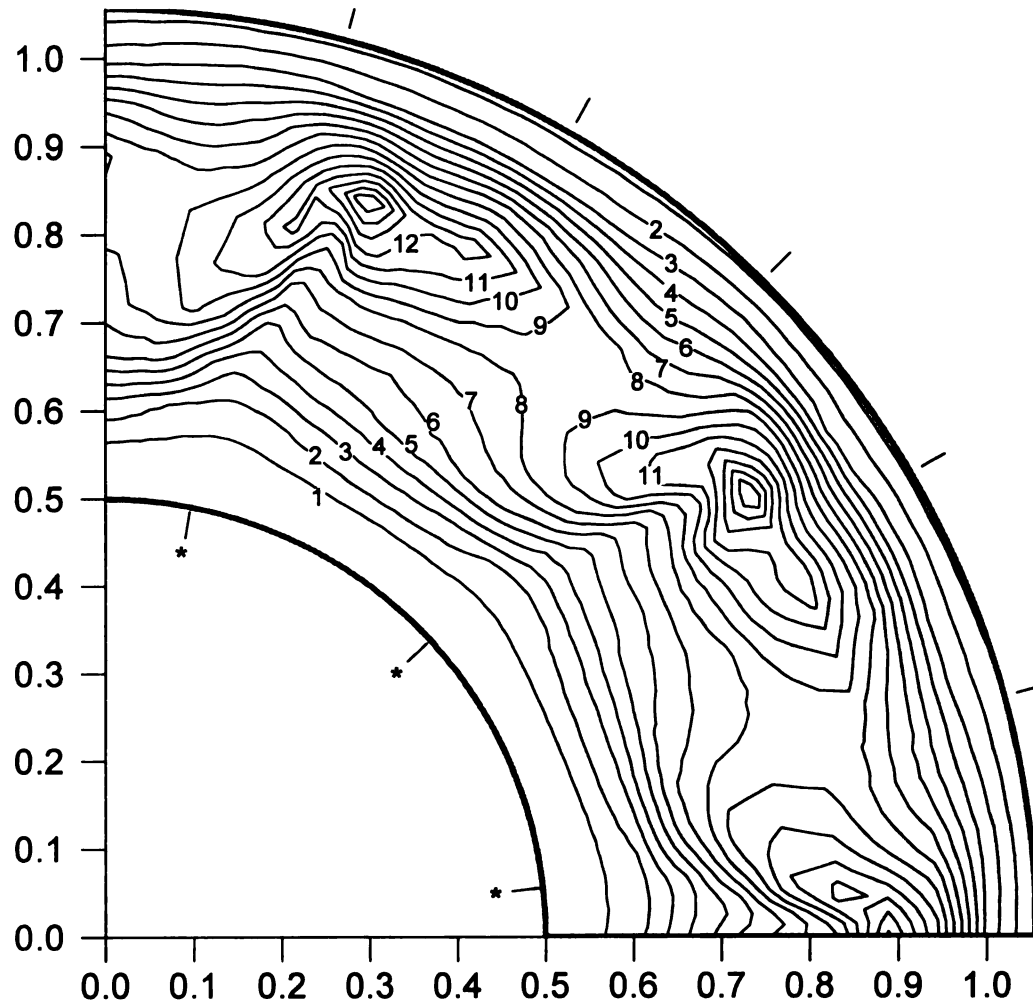
Contour Number	$\dfrac{2KE}{U_o^2}$	$\dfrac{2KE}{U_{tip}^2}$
15	25.2	0.73
14	23.6	0.68
13	22.0	0.64
12	20.4	0.59
11	18.9	0.54
10	17.3	0.50
9	15.7	0.45
8	14.1	0.41
7	12.6	0.36
6	11.0	0.32
5	9.4	0.27
4	7.8	0.23
3	6.3	0.18
2	4.7	0.14
1	3.1	0.09

Figure B.4 Phase averaged kinetic energy for condition 'H'

Contour Number	$\dfrac{2KE}{U_o^2}$	$\dfrac{2KE}{U_{tip}^2}$
15	15.8	0.46
14	14.8	0.43
13	13.8	0.40
12	12.9	0.37
11	11.9	0.34
10	10.9	0.31
9	9.9	0.29
8	8.9	0.26
7	7.9	0.23
6	6.9	0.20
5	5.9	0.17
4	4.9	0.14
3	3.9	0.11
2	3.0	0.09
1	2.0	0.06

Figure B.5 Phase averaged kinetic energy for condition 'I'
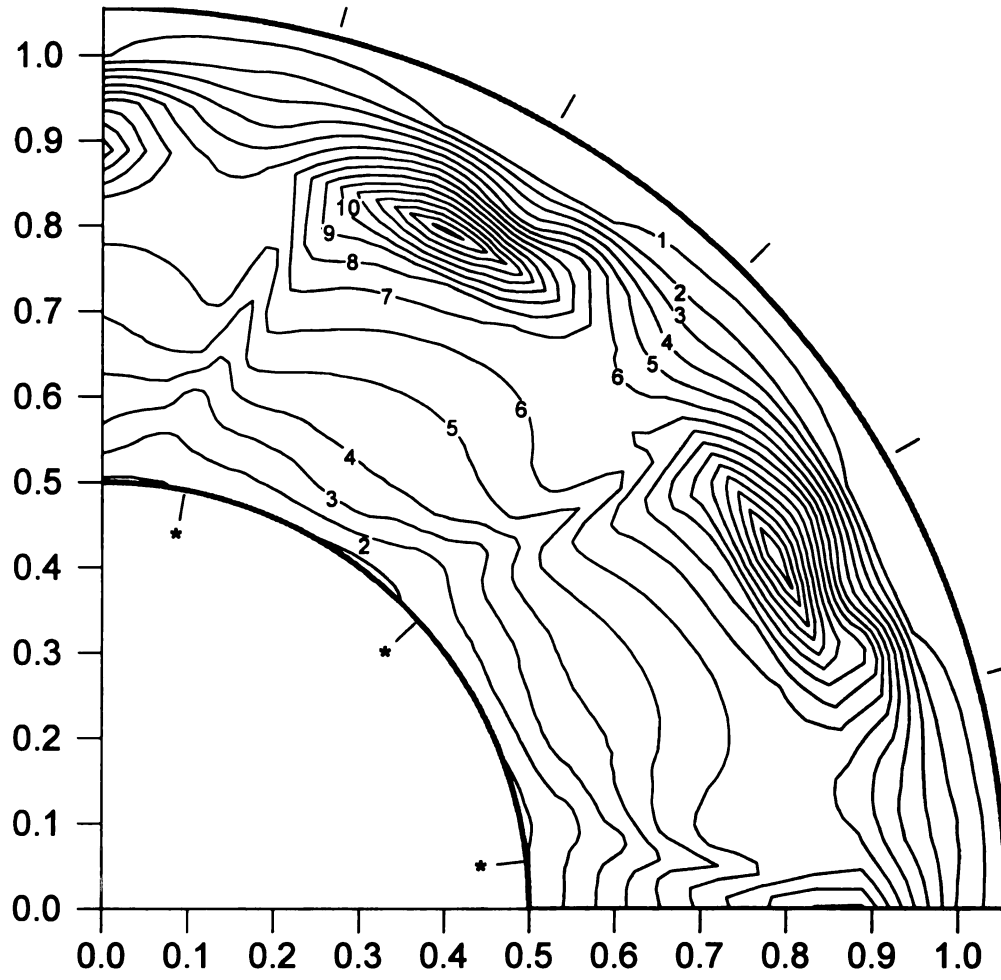
Contour Number	$\dfrac{2KE}{U_o^2}$	$\dfrac{2KE}{U_{tip}^2}$
15	11.7	1.05
14	11.0	0.99
13	10.2	0.92
12	9.5	0.85
11	8.7	0.78
10	8.0	0.72
9	7.2	0.65
8	6.4	0.58
7	5.7	0.51
6	4.9	0.44
5	4.2	0.38
4	3.4	0.31
3	2.7	0.24
2	1.9	0.17
1	1.2	0.11

Figure B.6 Phase averaged kinetic energy for condition 'J'
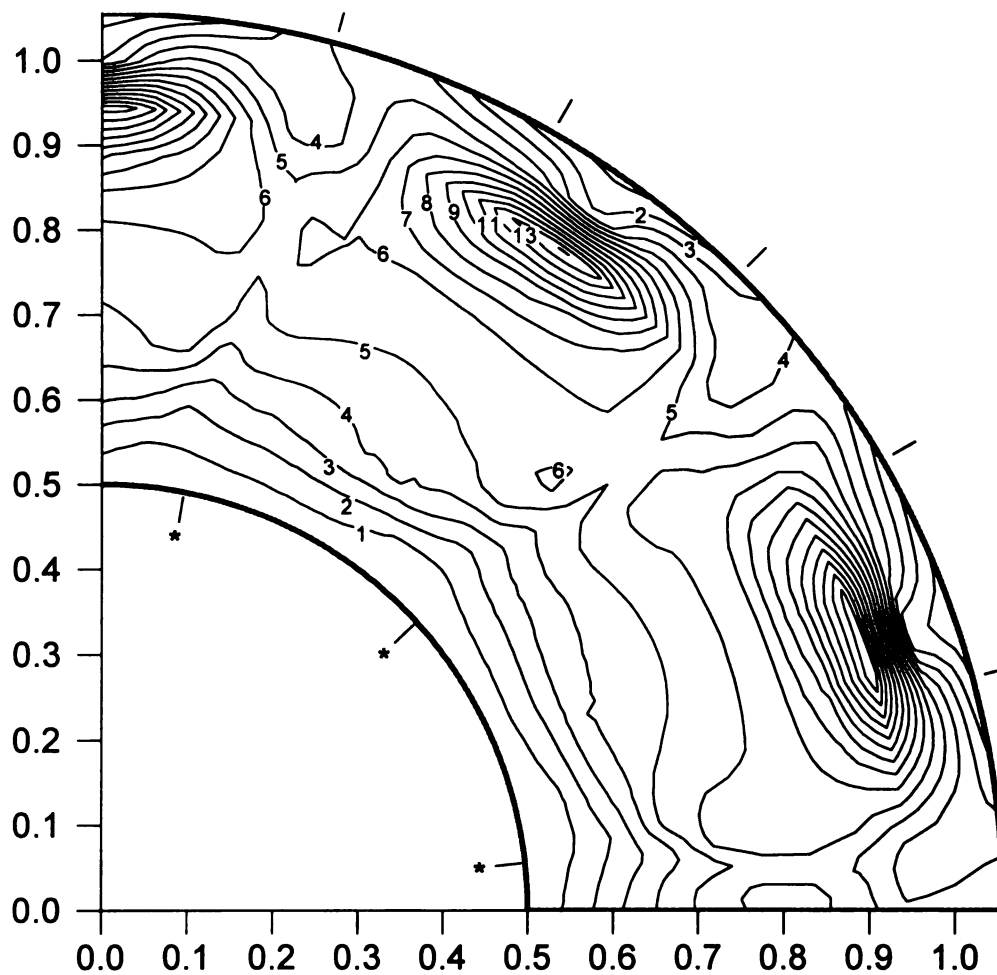
| Contour Number	$\dfrac{2KE}{U_o^2}$	$\dfrac{2KE}{U_{tip}^2}$
15	8.6	0.99
14	8.0	0.92
13	7.5	0.86
12	6.9	0.80
11	6.4	0.74
10	5.8	0.67
9	5.3	0.61
8	4.7	0.55
7	4.2	0.48
6	3.6	0.42
5	3.1	0.36
4	2.5	0.29
3	2.0	0.23
2	1.5	0.17
1	0.9	0.10

Figure B.7 Phase averaged kinetic energy for condition 'K'

Appendix C Exit Flow Angle Calculations

The phase averaged flow angle of the air leaving the fan (β_2) was calculated from the equation:

$$\beta_2 = \tan^{-1}\left(\frac{<\overline{U}_\theta>}{<\overline{U}_x>}\right)$$

Simple analysis of fans is often performed using velocity triangles and the relative inflow and exit flow angles. Performance and efficiency data can be estimated based on radial integration this information. These data for the test conditions 'G' through 'K' (see Chapter 6) are given in Figures C.1 through C.5 respectively.
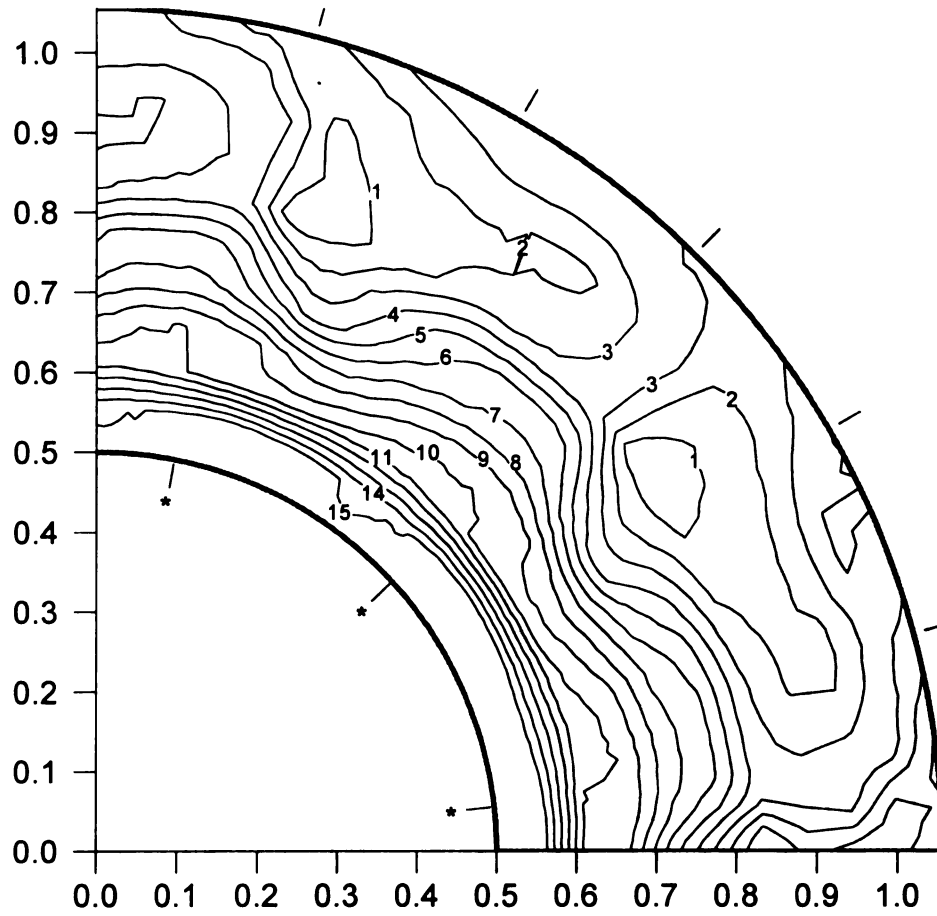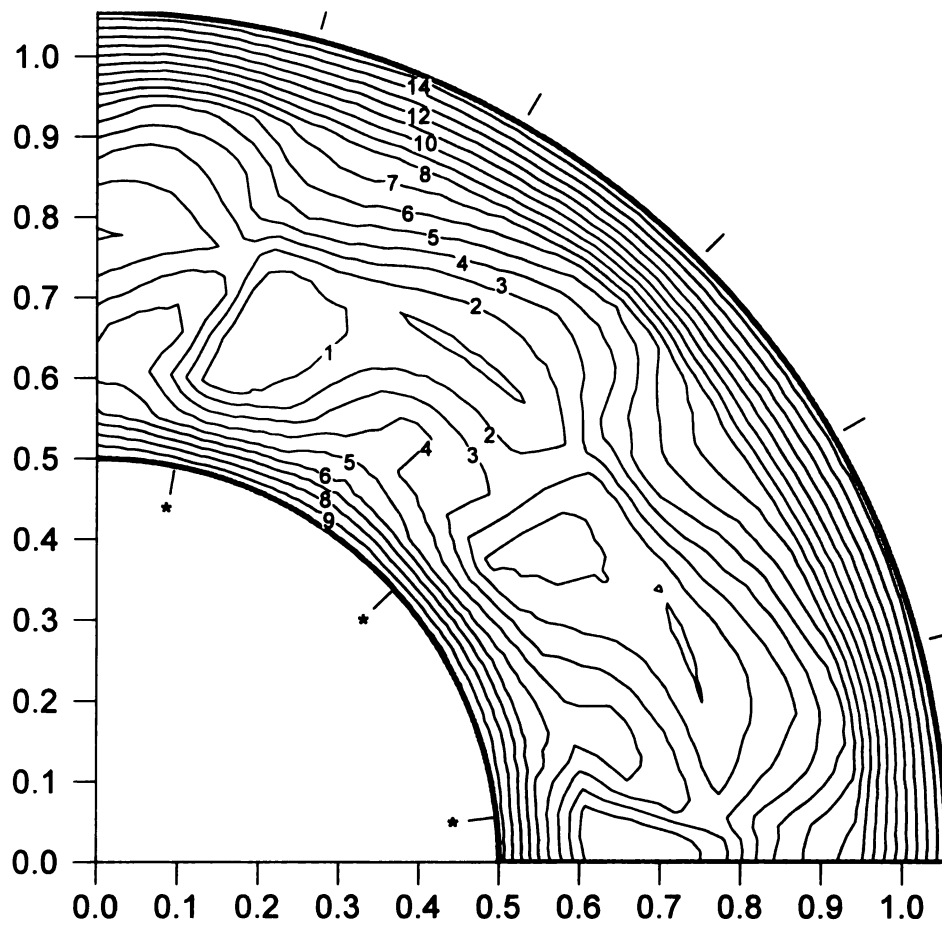
Contour Number	β_2
15	98.9
14	94.9
13	90.9
12	86.9
11	82.9
10	78.9
9	74.9
8	70.9
7	66.9
6	62.9
5	59.0
4	55.0
3	51.0
2	47.0
1	43.0

Figure C1 Phase averaged exit flow angle for condition 'G'
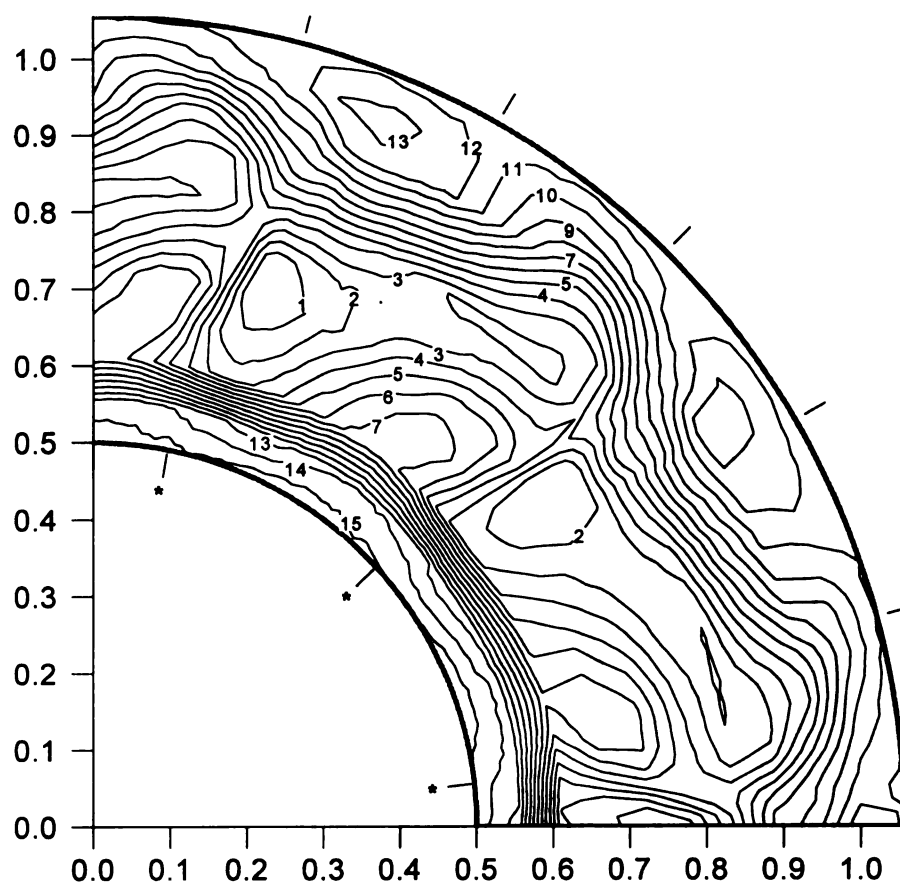
Contour Number	β_2
15	72.4
14	69.8
13	67.2
12	64.5
11	61.9
10	59.3
9	56.7
8	54.1
7	51.4
6	48.8
5	46.2
4	43.6
3	40.9
2	38.3
1	35.7

Figure C2 Phase averaged exit flow angle for condition 'H'

Contour Number	β_2
15	84.2
14	80.5
13	76.8
12	73.1
11	69.5
10	65.8
9	62.1
8	58.4
7	54.7
6	51.0
5	47.3
4	43.6
3	39.9
2	36.2
1	32.6

Figure C3 Phase averaged exit flow angle for condition 'I'

Contour Number	β_2
15	71.2
14	67.1
13	63.0
12	59.0
11	54.9
10	50.9
9	46.8
8	42.7
7	38.7
6	34.6
5	30.6
4	26.5
3	22.4
2	18.4
1	14.3
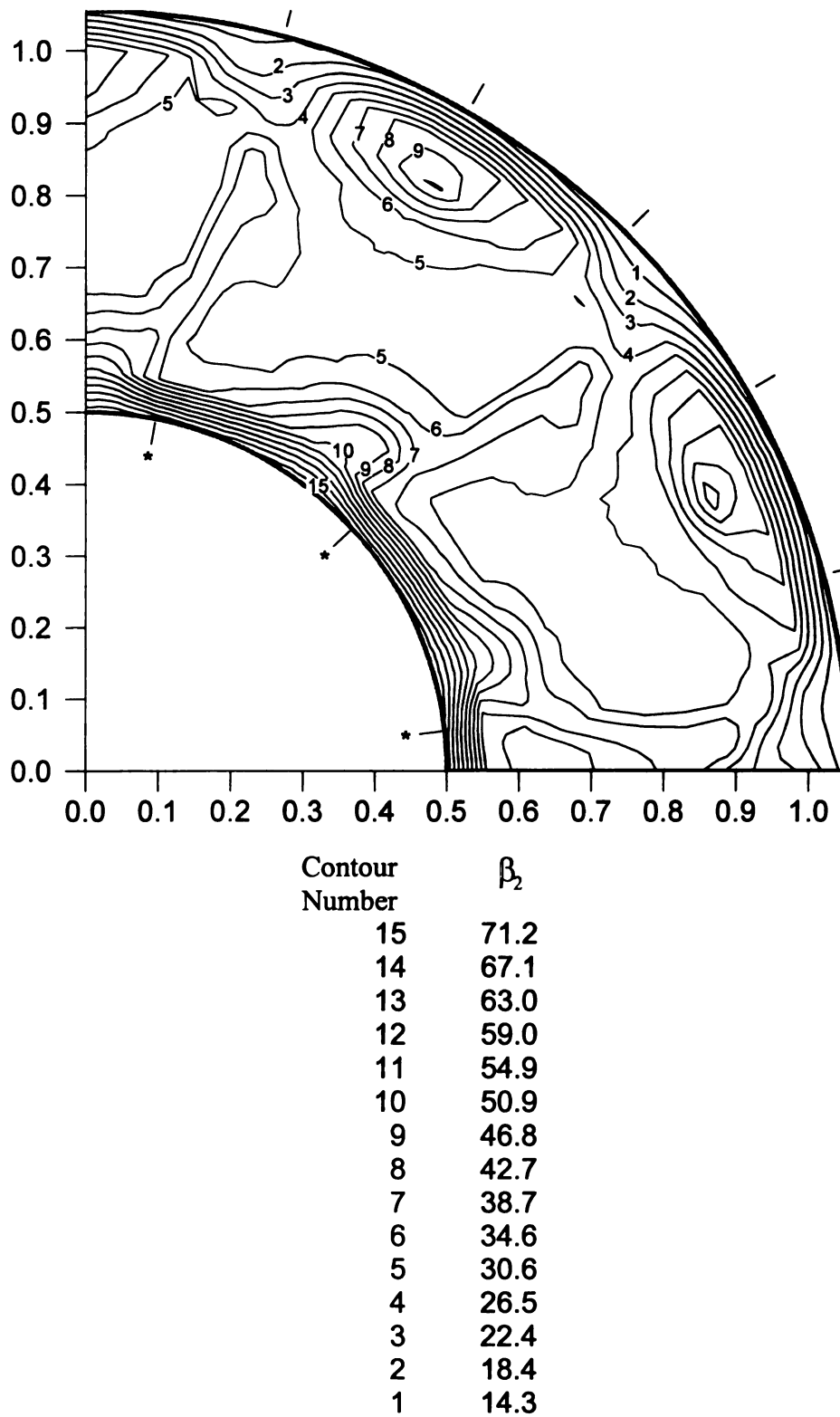
Figure C4 Phase averaged exit flow angle for condition 'J'
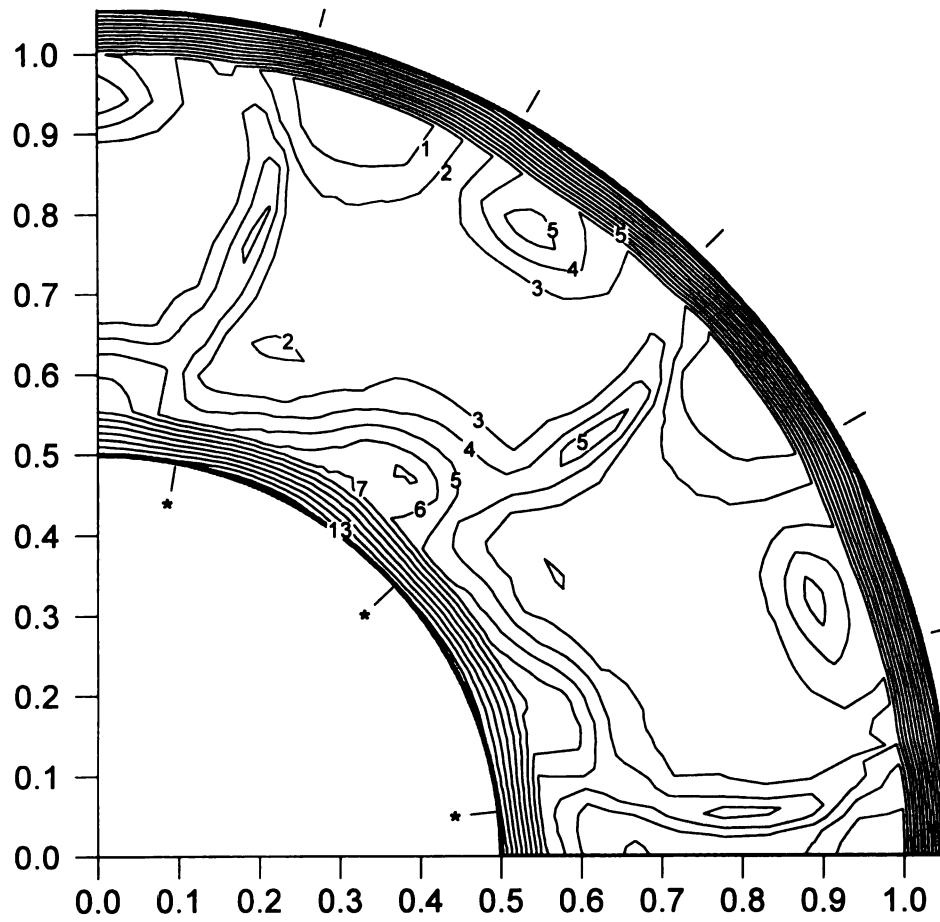
Contour Number	β_2
15	84.4
14	79.9
13	75.4
12	70.9
11	66.4
10	61.8
9	57.3
8	52.8
7	48.3
6	43.8
5	39.3
4	34.8
3	30.3
2	25.8
1	21.2

Figure C5 Phase averaged exit flow angle for condition 'J'